



TECHNISCHE  
UNIVERSITÄT  
DRESDEN

---

# The Dynamically Assisted Schwinger Process: Primary and Secondary Effects

Dissertation  
zur Erlangung des akademischen Grades  
Doctor rerum naturalium

vorgelegt von

Andreas Otto

geboren am 19. November 1987 in Lichtenstein

Institut für Theoretische Physik  
Fachrichtung Physik  
Fakultät Mathematik und Naturwissenschaften  
der Technischen Universität Dresden  
2017

1. Gutachter: Prof. Dr. Burkhard Kämpfer
2. Gutachter: Prof. Dr. Dominik Stöckinger
3. Gutachter: Prof. Dr. David Blaschke

Eingereicht am 4. August 2017

## Abstract

The dynamical Schwinger effect refers to the creation of electron-positron pairs by a time dependent, spatially homogeneous electric field. It probes the fundamentals of quantum electrodynamics and is sought to be verified with upcoming high-intensity laser installations. In the dynamically assisted Schwinger effect, the pair yield is increased by orders of magnitude through the combination of fields of different field strength and frequency scales. In this thesis we, investigate both processes in the framework of a quantum kinetic equation. We are especially interested in what amplification factors can be achieved by the assisting field and whether intermediately large mode occupation numbers have a physical significance and could serve as a verification of the Schwinger effect. For the latter goal, we couple our system to a quantized radiation field that serves as a secondary (photon) probe and study its spectrum, as the afterglow of the dynamical Schwinger effect.

## Kurzdarstellung

Als dynamischen Schwingereffekt bezeichnet man die Erzeugung von Elektron-Positron-Paaren durch ein zeitabhängiges, räumlich homogenes elektrisches Feld. Er dient zur Untersuchung der Grundlagen der Quantenelektrodynamik und es wird versucht, ihn an zukünftigen Hochintensitäts-Laseranlagen zu verifizieren. Bei dem dynamisch assistierten Schwingereffekt wird die Paarausbeute durch eine Kombination von Feldern mit unterschiedlichen Feldstärken- und Frequenzskalen um mehrere Größenordnungen erhöht. In dieser Dissertation untersuchen wir beide Prozesse im Rahmen einer quantenkinetischen Gleichung. Wir interessieren uns besonders dafür, welche Verstärkungsfaktoren durch das assistierende Feld erreicht werden können und ob intermediär große Modenbesetzungszahlen physikalische Signifikanz haben und als Verifizierung des Schwingereffekts dienen können. Für zweiteres Ziel koppeln wir unser System an ein quantisiertes Strahlungsfeld, das als sekundäres (Photonen-) Signal dient, und untersuchen dessen Spektrum, das Nachglühen des dynamischen Schwingereffekts.





# Contents

<b>1</b>	<b>Introduction</b>	<b>1</b>
1.1	Pair creation and Schwinger effect . . . . .	2
1.2	Outline of this thesis . . . . .	5
<b>2</b>	<b>Dynamical Schwinger effect</b>	<b>9</b>
2.1	Nomenclature and definitions . . . . .	9
2.2	Derivation of the Quantum Kinetic Equation . . . . .	10
2.2.1	The Bogoliubov transform . . . . .	10
2.2.2	Particle number and quantum kinetic equation . . . . .	12
2.2.3	Low-density approximation . . . . .	13
2.3	Electrical fields . . . . .	14
2.3.1	Schwinger field . . . . .	15
2.3.2	Sauter pulse . . . . .	15
2.3.3	Periodic pulse . . . . .	17
2.4	Numerics . . . . .	19
2.4.1	Dimensionless quantum kinetic equation . . . . .	19
2.4.2	Implementation details . . . . .	20
2.4.3	Exploiting periodicity . . . . .	21
2.5	Phase space structure and time evolution for the periodic pulse . . . . .	22
2.5.1	Fourier analysis within the low-density approximation . . . . .	22
2.5.2	Behavior of $f$ close to a shell . . . . .	26
2.5.3	Total pair number . . . . .	30
2.6	Calculating the amplitudes $I_n$ . . . . .	31
2.6.1	Singularity and integration contour . . . . .	31
2.6.2	Expanding the integrand and closing the contour . . . . .	32
2.7	Physics from the amplitudes . . . . .	34
2.8	Summary . . . . .	39
<b>3</b>	<b>Dynamically assisted Schwinger effect</b>	<b>41</b>
3.1	Superposition of two Sauter pulses . . . . .	41
3.1.1	Field model . . . . .	41
3.1.2	Numerical results . . . . .	43
3.2	Superposition of two periodic pulses . . . . .	45
3.2.1	Numerical results . . . . .	45
3.2.2	Location and movement of the zeros . . . . .	48
3.2.3	Envelope for the two field case . . . . .	50
3.3	Summary . . . . .	52
<b>4</b>	<b>Photon signature</b>	<b>53</b>
4.1	Backreaction . . . . .	53
4.1.1	Normal order and mean-field current . . . . .	53

4.1.2	Equation of motions . . . . .	54
4.2	A formula for the photon spectrum . . . . .	57
4.2.1	Evaluation of $C_{rsi}$ . . . . .	59
4.2.2	Small- and large-frequency behavior of $C_{rsi}$ . . . . .	60
4.3	Application of the photon spectrum formula . . . . .	62
4.3.1	Numerics . . . . .	62
4.3.2	Numerical results . . . . .	62
4.4	Summary . . . . .	66
<b>5</b>	<b>Conclusion and outlook</b>	<b>69</b>
<b>A</b>	<b>A toy model for particle creation</b>	<b>71</b>
<b>B</b>	<b>Some mathematical remarks about the quantum kinetic equation</b>	<b>75</b>
B.1	Properties of the base spinors . . . . .	75
B.2	Lifting the quantum kinetic equation to the Lie algebra . . . . .	76
B.3	Long term evolution of $f$ for a periodic field . . . . .	78
<b>C</b>	<b>Generalized Bogoliubov transform</b>	<b>81</b>
C.1	Linear transformation of creation and annihilation operators . . . . .	81
C.2	Second quantization . . . . .	85
	<b>List of Figures</b>	<b>93</b>
	<b>List of Tables</b>	<b>96</b>
	<b>Bibliography</b>	<b>97</b>

# 1 Introduction

Quantum electrodynamics (QED) is the quantum theory of light interacting with matter and describes, for example, the scattering of a photon off an electron, the Coulomb interaction or the annihilation of an electron and a positron, producing two photons. Together with the electro-weak interaction and quantum chromodynamics (QCD), it is one of the three pillars of the standard model of particle physics. It is the first and arguably most successful quantum field theory (QFT) and its creators, R. Feynman, J. Schwinger and S. Tomonaga, were awarded the Nobel price for their discovery. In this theory the strength of the coupling between light and matter is encoded in the quantity  $e$ , the elementary charge. A standard technique for calculations in QED is to expand physical observables in powers of  $e$  using Feynman diagrams. For example, the magnetic moment  $g$  of the electron calculated within QED is  $g = 2 + \frac{e^2}{4\pi^2} + \mathcal{O}(e^4)$ . It is an early result of the theory [1] and greatly helped to establish its validity and reputation. Julian Schwinger, who calculated the first-order correction, had the result engraved on his tombstone. Over the years  $g$ , was calculated to ever higher orders in  $e$ , currently up to  $e^{10}$  [2, 3], showing impressive agreement with the experiment.

There are, however, calculations for which such an expansion is not possible, for fundamental (the result may be non-analytical in the expansion parameter  $e$ ) or practical reasons (the Feynman diagrams get too complicated to evaluate). This happens when the electromagnetic fields involved get strong, on the order of the “critical” electric field strength  $E_c = m^2/e = 1.3 \times 10^{18}$  V/m (or  $B_c = 4.4 \times 10^9$  T for the magnetic field strength) with  $m$  the electron mass. The subfield that deals with such phenomena is called strong-field QED and is less well tested than the perturbative sector. Its most prominent example is the Schwinger effect [4] which, despite its name, was first investigated by Sauter [5] and Euler and Heisenberg [6]. It is the name given to the spontaneous creation of electron-positron pairs from vacuum by a static electric field. As it is the background for most of this thesis, we will describe it in more detail below.

Other areas of strong-field QED include light-by-light scattering. Although photons cannot directly interact with each other (QED being an abelian gauge theory, there are no interaction vertices between the gauge field), they can interact via a virtual fermion loop, creating an effective photon-photon vertex. This can for example manifest in the matterless double-slit: two strong lasers are focused parallel to each other and a beam of high-frequency photons is shone perpendicularly on this focal region. By theory’s prediction, an interference pattern as in the classical double-slit experiment should emerge [7, 8]. A similar effect is vacuum birefringence, where a strong electric field polarizes the vacuum, making it birefringent [9, 10].

Strong electro-magnetic fields can for example be found in the vicinity of super-heavy nuclei. The binding energy of the lowest electron state exceeds the electron-positron band gap at a critical nuclear charge of  $Z_{\text{cr}} = 172.5$  [11, 12]. That means that state dives into

the positron continuum, resulting in pair creation. Since such heavy stable nuclei have not yet been discovered, it was sought to observe this effect in heavy ion collisions [13, 14]. This was thwarted by the lifetime of the resulting composite nuclei being short low to allow for pair creation to set in.<sup>1</sup> Other sources can be found in outer space in the form of pulsars and magnetars which are rapidly rotating neutron stars. Their magnetic field can reach strengths of  $10^8$  to  $10^{11}$  T [15, 16]. This is well in the regime of strong-field QED. Even the electric fields these magnetic fields induce can reach the critical field strength and the energy density of the “vacuum” in the presence of such a magnetic field is greater than the mass density of lead. Unfortunately it is hard to set up laboratory equipment close to neutron stars. However, through the light emitted from these stars, the birefringence induced by this strong magnetic field may be detected [17, 18].

At present, the most promising avenue for observing strong field effects is via high-intensity (optical) lasers. They have so far eluded experimental verification for two reasons: the experimentally achievable field strength  $E$  is still small compared to  $E_c$  and many effects scale exponentially with  $E$ , e.g.  $\propto e^{-\pi \frac{E_c}{E}}$ . For lasers, the critical field strength corresponds to a critical intensity  $I_c$  which in natural units is just  $I_c = E_c^2$  and has a numerical value of  $I_c = 4.4 \times 10^{29}$  W/cm<sup>2</sup>. Current petawatt lasers reach intensities of  $10^{21}$  to  $10^{24}$  W/cm<sup>2</sup> which corresponds to field strengths of  $E \approx 10^{-5} \dots 10^{-3} E_c$ . This translates to e.g. the Schwinger effect being suppressed by a factor of about  $e^{10^4} \dots e^{10^6}$ . In recent years, a multitude of research facilities focusing on strong (optical) lasers have been proposed, planned and funded, with some already in operation. Examples are the Vulcan 10 PW project [19], Apollon [20], PHELIX [21, 22] HiPER [23, 24], POLARIS [25, 26], HIBEF [27], PETAL [28], ELI [29–31] and XCELS [32, 33]. For an overview of the technology used to achieve these field strengths see [34]. There are different trade-offs between intensity, total energy delivered and pulse length, among others, with some more suitable for strong-field QED and some for other fields of physics. The race to higher intensities generates a mutual amplification of interest between theorists and experimentalist: Higher available field strengths let us probe the quantum vacuum, and interesting prediction of new physics drives the development of stronger lasers. For general proposals for utilizing these facilities for strong-field QED research, see [35–40].

### 1.1 Pair creation and Schwinger effect

This thesis focuses on pair creation by electric fields. We will assume our  $E$  field to be spatially homogeneous, but time dependent. The model for this is two colliding lasers. They will form a standing wave with the electric field in the anti-nodes being homogeneous at the scale of the wavelength of the lasers. If this is large compared to the Compton wavelength of the electron, our simplification is justified. The Compton wavelength is the intrinsic length scale of pair creation. Indeed, we can interpret the critical field strength the following way: An electron in a field of this strength gains its own rest mass as energy when accelerated over one Compton wavelength.

The Schwinger effect is only one physical setting in which particles can be created. There is also the famous Hawking radiation, where the horizon of a black hole splits a virtual

---

<sup>1</sup>Similarly, the passage time of peripheral ultrarelativistic heavy ion collisions is argued to be too short to cause analog strong-field effects.

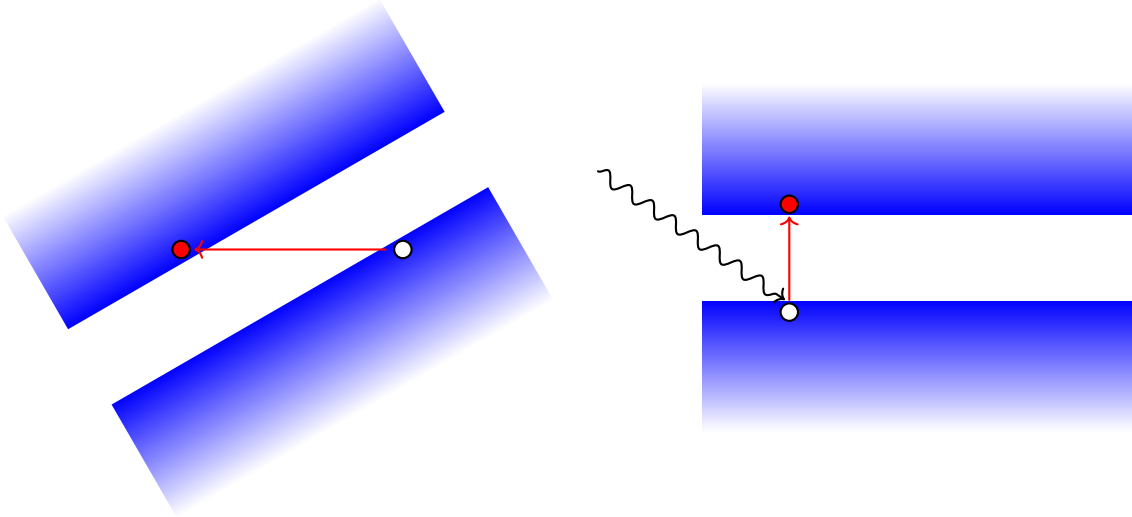


**Figure 1.1:** Schematic illustration of the Schwinger (left) and Breit-Wheeler effect (right) in the Dirac sea picture. The positron continuum is the lower blue band, the electron continuum the upper one. The red circle represents a particle, the white circle a hole and the wiggly line a photon.

particle-anti-particle loop and one of them escapes and can be measured as thermal radiation by a far away observer [41, 42]. The driving force here is gravitation in the context of general relativity (GR). Indeed GR provides a wide variety of scenarios for particle creation, e.g. on a large scale by an expanding universe [43–45] or inflationary reheating [46], or on a small scale through Unruh radiation [47]. The latter also has parallels with QED [48]. In fact, QFT on curved space-time has many interesting parallels with background field QED. Yet another example is from quantum chromodynamics with hadron production from chromoelectric flux tubes [49]. Also in QCD, there is the chiral phase transition, which can be modeled by a time dependent particle mass, leading to pair production too [50, 51]. These different scenarios are conceptually similar, with the underlying theoretical description being the Bogoliubov transform which diagonalizes a time dependent Hamiltonian. Its time dependence in the above examples comes from quite different physical phenomena: a background field, or curved space-time or time dependent mass. We will investigate the Bogoliubov transform in detail in the course of this work, but as an introduction to the general cases, we invite the reader to read appendix A. It presents a toy model for pair creation which, although simplified, captures many of the essential concepts.

We will investigate electron-positron (pair) production within QED. There are conceptually two processes by which this can happen, the already mentioned Schwinger effect and the Breit-Wheeler process. The former can be interpreted in the Dirac sea picture as a (constant) electric field tilting the electron and positron continua. A particle from the filled lower continuum will tunnel into the higher one, leaving a hole behind (the positron) and becoming an electron. This is shown schematically in the left panel of Fig. 1.1. It has as of yet, as we mentioned, not been observed due to insufficient available field strengths. The Breit-Wheeler process is conceptually simpler: Two photons collide and produce a pair,  $\gamma\gamma \rightarrow e^+e^-$ . Interpreting it similarly to the Schwinger effect, we can be imagined a particle being lifted by a photon from the lower into the upper continuum see the right panel of

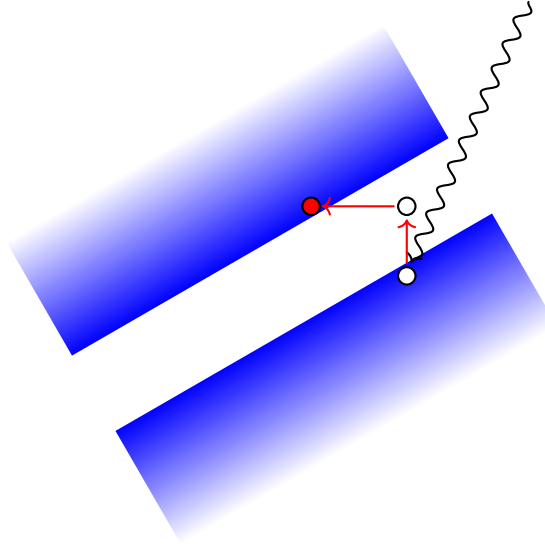


**Figure 1.2:** Schematic illustration of the dynamically assisted Schwinger effect, with entities as in Fig. 1.1.

Fig. 1.1.<sup>2</sup> This process *has* been observed in the E144 experiment [52]. The Schwinger effect's dependence on the field strength is  $\propto E^2 e^{-\pi \frac{E_c}{E}}$ , while the Breit-Wheeler's is  $\propto E^2$ . As might be guessed from the intuitive picture, the latter effect can be easily calculated in the perturbative regime, when just two photons take part in creating a pair, which happens when the combined energy of the photons in their rest frame is greater than  $2m$ . When the energy is lower, more photons and thus are higher field strength are needed and the perturbative calculations get progressively more complicated, to the point of being intractable. That is when strong-field methods need to be applied.<sup>3</sup>

The dynamical Schwinger effect is the middle ground between these two examples. The electrical field is still assumed as a spatially homogeneous background field, but can vary with time. We will later see that this contains the correct scaling behaviors w.r.t.  $E$  of both processes as a limiting case. It is thus some matter of interpretation where to draw the line between both processes, but it is a fallacy to assume two things are the same whenever one can gradually transition from one to the other. A slowly varying but strong field acts more like the Schwinger effect, and a fast but weak field like the Breit-Wheeler process. Combining two fields with such different scales results in the so called dynamically assisted Schwinger effect [53, 54] which increases the number of produced pairs by orders of magnitude. The idea behind it is depicted in Fig. 1.2: the slow and strong field tilts the bands as before and the photons from the fast and weak field lift a particle from the positron continuum. They do not lift it completely into the upper band, but it is enough to shorten the tunneling length. Since tunneling probability depends exponentially on tunneling length, even a rather small lift will have a large effect. Such a setup might be achieved experimentally by colliding a strong optical laser with an X-ray free electron

---

<sup>2</sup>The reaction needs two photons for the conservation of momentum, but we did not draw them in the picture.

<sup>3</sup>It should be noted, however, that the law of conservation of effort holds. To apply strong-field methods, one assumes the photons come from a coherent background field which is another approximation (in contrast to perturbation theory), but one more suitable for this case.

laser [55] which, as the name suggests, operates at much higher frequencies than the former, but also lower field strengths.

Since the Schwinger effect, as mentioned, has as of yet not been observed due to insufficient pair yields (or equivalently insufficiently strong fields), we will also look at possible secondary probes. In particular, even when no real particles are produced, there will be some virtual particles influenced by the applied electric field.<sup>4</sup> In our chosen approach, this manifests in a large number of quasi-particles at intermediate times. They can potentially radiate real photons through various processes, e.g. pair annihilation or bremsstrahlung. These real photons may serve as a verification of the Schwinger effect, even when the residual pair yield is too low to measure. Of further interest in this context is the fundamental question whether the intermediate quasi-particles have any physical meaning, since in the standard QFT interpretation, only the out-states and thus the residual pair number can be connected to observables. This photon radiation from the background field is conceptually similar to photon-photon scattering and vacuum birefringence, but we do not use an external probe photon and emphasize the relation to the intermediate quasi-particles as a possible verification of the dynamical Schwinger effect.

## 1.2 Outline of this thesis

In chapter 2 we will investigate the dynamical Schwinger effect. There is already a lot of research on this subject (see [56] for a recent review, also relevant for chapter 3). Our main tool is the so called quantum kinetic equation [57, 58]. There are also different approaches, such as WKB methods [59, 60], worldline instantons [61–63] or the Wigner formalism [64–66]. Phenomenologically, we restrict ourselves to spatially homogeneous, linearly polarized, time dependent fields. Spatially inhomogeneous fields were studied in [67–71], other polarizations in [72, 73] and superpositions of plane waves in [74, 75]. Within our model and approach, there are a variety of time dependencies for the electric field under investigation. We will cite more specific literature when we discuss them in chapter 2.

Chapter 3 discusses the dynamically assisted Schwinger effect. We will superpose two fields of different scales, as was first proposed in [53, 54]. We do this for different time dependencies and, building on the results of chapter 2, we give an explanation for the orders of magnitude increase in the particle yield.

Chapter 4 deals with the secondary photon probes. We couple our system to a quantized radiation field similar to [50]. This results in the vacuum emitting photons in the presence of an electric background field and we discuss how they might serve as a verification of the dynamical Schwinger effect and how they pertain to the interpretation of QFT. Also, the echo of the dynamically assisted Schwinger effect in the photon spectrum is discussed.

Chapter 5 provides a conclusion and outlook in addition to the short summaries at the end of each chapter.

---

<sup>4</sup>One popular intuitive picture is the external field aligning virtual electron-positron loops, thus polarizing the vacuum.

In appendix A we exhibit the already mentioned toy model of particle creation. Appendix B deals with some mathematical properties of our chosen framework, the quantum kinetic equation. Appendix C explains the theory of general Bogoliubov transforms, valid for all quadratic Hamiltonians and background fields (not just spatially homogeneous ones).

Published papers containing results that are presented in this thesis are (in chronological order)

- I A. Otto, D. Seipt, D. Blaschke, B. Kämpfer, and S. A. Smolyansky, “Lifting shell structures in the dynamically assisted Schwinger effect in periodic fields”, *Phys. Lett. B* **740**, 335 (2015)
- II A. Otto, D. Seipt, D. B. Blaschke, S. A. Smolyansky, and B. Kämpfer, “Dynamical Schwinger process in a bifrequent electric field of finite duration: Survey on amplification”, *Phys. Rev. D* **91**, 105018 (2015)
- III A. Otto, T. Nusch, D. Seipt, B. Kämpfer, D. B. Blaschke, A. D. Panferov, S. A. Smolyansky, and A. I. Titov, “Pair production by Schwinger and Breit-Wheeler processes in bi-frequent fields”, *J. Plasma Phys.* **82**, 655820301 (2016)
- IV T. Nusch, A. Otto, D. Seipt, B. Kämpfer, A. I. Titov, D. B. Blaschke, A. D. Panferov, and S. A. Smolyansky, “Laser assisted Breit-Wheeler and Schwinger processes”, Proceedings of the International Symposium on New Horizons in Fundamental Physics, Makutsi, South Africa, 23.–28. November 2015, FIAS Interdisc. Sci. Ser. (2017), pp. 253–262
- V A. D. Panferov, S. A. Smolyansky, A. Otto, B. Kämpfer, D. B. Blaschke, and Ł. Juchnowski, “Assisted dynamical Schwinger effect: pair production in a pulsed bifrequent field”, *Eur. Phys. J. D* **70**, 56 (2016)
- VI S. A. Smolyansky, A. D. Panferov, D. B. Blaschke, Ł. Juchnowski, B. Kämpfer, and A. Otto, “Vacuum particle-antiparticle creation in strong fields as a field induced phase transition”, *Russ. Phys. J.* **59**, 1731 (2017)
- VII A. Otto and B. Kämpfer, “Afterglow of the dynamical Schwinger process: Soft photons amass”, *Phys. Rev. D* **95**, 125007 (2017)

Paper I contains mainly numerical results from chapters 2 and 3 and paper II the analytical derivations. Papers III and IV contain details of the time evolution for the periodic pulse from chapter 2 and compares the Schwinger effect with the Breit-Wheeler process. Papers V and VI discuss the dynamical and dynamically assisted Schwinger effect for the Sauter pulse and how the transition of the intermediate high quasi-particle number to the residual pair number can be interpreted as a phase transition. Paper VII contains the results of chapter 4, the secondary photon probes of the Schwinger effect.

Parallel to elaborating the material in this thesis, two Bachelor’s and one Master’s thesis have been supervised, with another Bachelor’s thesis on the backreaction (see chapter 4) being in progress:



1. H. Oppitz, “Dynamisch assistierter Schwinger-Effekt in unterschiedlichen Feldkonfigurationen”, Bachelor’s Thesis (Technische Universität Dresden, 2013)
2. S. Hähnel, “Paarerzeugung in elektrischen Feldern: Numerische Untersuchungen zum Schwinger-Effekt”, Bachelor’s thesis (Technische Universität Dresden, 2015)
3. H. Oppitz, “Dynamisch assistierter Schwinger-Effekt für Multi-Skalen-Feldkonfigurationen”, Master’s Thesis (Technische Universität Dresden, 2017)



## 2 Dynamical Schwinger effect

In this chapter we will investigate the dynamical Schwinger effect, in which only one field is active. We will first derive the quantum kinetic equation, the workhorse of this thesis as it underlies most of our calculations, and discuss approximations as well as some aspects of its numerical implementation. This derivation is done by diagonalizing the Hamiltonian via a Bogoliubov transform. Then we introduce the different types of time dependent fields that are commonly studied and present brief results for the Schwinger and Sauter fields, before turning to the periodic pulse, which is our main focus and will take the rest of the chapter. We study the resulting spectrum first with analytical methods which we later compare to the numerics.

### 2.1 Nomenclature and definitions

We use units in which  $\hbar = c = 1$ . Three-vectors are indicated by boldface (e.g.  $\mathbf{x}$ ) and their components by latin indices (e.g.  $x_i$ ). Four-vectors are in normal math font (e.g.  $x$ ) and their components indexed by greek letters (e.g.  $x^\mu$ ). The metric tensor is “mostly negative”, i.e.  $g = \text{diag}(1, -1, -1, -1)$ , so that the scalar product of two four-vectors  $x = (t, \mathbf{x})$  and  $y = (s, \mathbf{y})$  is  $xy = x^\mu y_\mu = ts - \mathbf{x} \cdot \mathbf{y}$ . The Dirac matrices are in the Weyl representation given by

$$\gamma^0 = \begin{pmatrix} 0 & 1 \\ 1 & 0 \end{pmatrix}, \quad \boldsymbol{\gamma} = \begin{pmatrix} 0 & \boldsymbol{\sigma} \\ -\boldsymbol{\sigma} & 0 \end{pmatrix}, \quad (2.1)$$

and the Pauli matrices are

$$\sigma_1 = \begin{pmatrix} 0 & 1 \\ 1 & 0 \end{pmatrix}, \quad \sigma_2 = \begin{pmatrix} 0 & -i \\ i & 0 \end{pmatrix}, \quad \sigma_3 = \begin{pmatrix} 1 & 0 \\ 0 & -1 \end{pmatrix}. \quad (2.2)$$

We employ Dirac’s slash notation, that is for any four-vector  $A$  we define  $\not{A} = \gamma^\mu A_\mu$ . Partial derivatives have the following equivalent notations

$$\frac{\partial}{\partial y} f(x^\mu) = \partial_y f(x^\mu) = \partial_2 f(x^\mu) \quad (2.3)$$

and the total time derivative can be expressed as

$$\frac{d}{dt} g(t) = \dot{g}(t). \quad (2.4)$$

The momentum component parallel to the unidirectional electrical field is called  $p_\parallel$  and that perpendicular to it  $p_\perp$ . Since  $\mathbf{E}$  will always point along the  $z$  direction,  $p_\parallel = p_z$ .

## 2.2 Derivation of the Quantum Kinetic Equation

The aim of this section is to diagonalize the QED Hamiltonian in the presence of a background field  $A$ ,

$$H(t) = \int d^3x \bar{\Psi}(t, \mathbf{x}) [-i\gamma \nabla + e\mathbf{A} + m] \Psi(t, \mathbf{x}), \quad (2.5)$$

via a Bogoliubov transformation. We will derive an equation for the coefficients of this transformation, which in turn implies an equation for the number of created pairs.

### 2.2.1 The Bogoliubov transform

The Heisenberg equation of motion for the operator  $\Psi$  following from (2.5) is the Dirac equation

$$(i\partial\!\!\!/ - e\mathbf{A}(t, \mathbf{x}) - m)\Psi(t, \mathbf{x}) = 0. \quad (2.6)$$

Choosing the Coulomb gauge we set  $A^0 = E^0 = 0$  so only the vector components remain. Recall that we assume our electric field (and thus the vector potential  $\mathbf{A}$ ) spatially homogeneous, linearly polarized and time dependent.

$$\mathbf{E}(t, \mathbf{x}) = \mathbf{E}(t) = E(t)\mathbf{e}_z, \quad \mathbf{A}(t, \mathbf{x}) = \mathbf{A}(t) = A(t)\mathbf{e}_z, \quad \dot{\mathbf{E}}(t) = -\dot{\mathbf{A}}(t). \quad (2.7)$$

This simple form of the field suggests the ansatz

$$\Psi(t, \mathbf{x}) = \int \frac{d^3p}{(2\pi)^3} \psi(t, \mathbf{p}) e^{i\mathbf{p}\mathbf{x}}. \quad (2.8)$$

Plugging (2.8) in (2.6) yields a reduced Dirac equation for  $\psi$ , which in Schrödinger form reads

$$i\partial_t \psi(t, \mathbf{p}) = h(\mathbf{P}(t)) \psi(t, \mathbf{p}), \quad (2.9)$$

with the quasi-momentum  $\mathbf{P}(t) = \mathbf{p} - e\mathbf{A}(t)$  and the first-quantized Dirac Hamiltonian

$$h(\mathbf{p}) = \gamma^0(\mathbf{p}\boldsymbol{\gamma} + m) = \begin{pmatrix} -\mathbf{p}\boldsymbol{\gamma} & m \\ m & \mathbf{p}\boldsymbol{\gamma} \end{pmatrix}. \quad (2.10)$$

The square of the matrix  $h$  is a scalar,  $h(\mathbf{p})^2 = \Omega(\mathbf{p})^2$ , with  $\Omega(\mathbf{p}) = \sqrt{m^2 + \mathbf{p}^2}$  the energy of a particle with mass  $m$  and momentum  $\mathbf{p}$ . Consequently,  $h(\mathbf{p})$  has  $\{-\Omega(\mathbf{p}), -\Omega(\mathbf{p}), \Omega(\mathbf{p}), \Omega(\mathbf{p})\}$  as its set of eigenvalues (counting multiplicity). We define by a slight abuse of notation  $h(t, \mathbf{p}) = h(\mathbf{P}(t))$  and  $\Omega(t, \mathbf{p}) = \Omega(\mathbf{P}(t))$  and use them interchangeably.

The Hamiltonian  $h(t, \mathbf{p})$  thus distinguishes two sets of bases of the spinor space:  $u_r(t, \mathbf{p})$ ,  $v_r(t, -\mathbf{p})$  and  $U_r(t, \mathbf{p})$ ,  $V_r(t, -\mathbf{p})$  with  $r = 1, 2$ . The first are solutions to (2.9):

$$\begin{aligned} i\partial_t u_r(t, \mathbf{p}) &= h(t, \mathbf{p}) u_r(t, \mathbf{p}), \\ i\partial_t v_r(t, -\mathbf{p}) &= h(t, \mathbf{p}) v_r(t, -\mathbf{p}), \end{aligned} \quad (2.11)$$

while the second are eigenvectors to  $h(t, \mathbf{p})$ :

$$\begin{aligned} h(t, \mathbf{p})U_r(t, \mathbf{p}) &= \Omega(t, \mathbf{p})U_r(t, \mathbf{p}), \\ h(t, \mathbf{p})V_r(t, -\mathbf{p}) &= -\Omega(t, \mathbf{p})V_r(t, -\mathbf{p}). \end{aligned} \quad (2.12)$$

From now on we require our field  $E$  to be switched on at  $t_{\text{on}}$  and off at  $t_{\text{off}}$ , i.e.  $E(t \leq t_{\text{on}}) = E(t \geq t_{\text{off}}) = 0$ . This implies  $A(t \leq t_{\text{on}}) = A_{-\infty}^1$  and  $A(t \geq t_{\text{off}}) = A_{\infty}$ . Our solutions to (2.11) and (2.12) can then be fixed by requiring they coincide with the free solutions at  $t = t_{\text{on}}$ :

$$\begin{aligned} u_r(t = t_{\text{on}}, \mathbf{p}) &= U_r(t = t_{\text{on}}, \mathbf{p}) = u_r(\mathbf{p}), \\ v_r(t = t_{\text{on}}, -\mathbf{p}) &= V_r(t = t_{\text{on}}, -\mathbf{p}) = v_r(-\mathbf{p}). \end{aligned} \quad (2.13)$$

We choose the time independent base spinors to be

$$u_r(\mathbf{p}) = \frac{\Omega(\mathbf{p}) + h(\mathbf{p})}{\sqrt{2\Omega(\mathbf{p})(\Omega(\mathbf{p}) - p_z)}} R_r, \quad v_r(-\mathbf{p}) = \frac{-\Omega(\mathbf{p}) + h(\mathbf{p})}{\sqrt{2\Omega(\mathbf{p})(\Omega(\mathbf{p}) + p_z)}} R_r, \quad (2.14)$$

where  $R_r$  are two eigenvectors to  $\gamma^0\gamma^3$  with eigenvalue  $-1$ , which suits our setting since  $\mathbf{E}$  points along the  $z$  axis.

It is straightforward to show the following properties of these base spinors (see appendix B.1): They are orthogonal

$$\begin{aligned} u_r^\dagger(\mathbf{p})u_s(\mathbf{p}) &= v_r^\dagger(-\mathbf{p})v_s(-\mathbf{p}) = \delta_{rs}, \\ u_r^\dagger(\mathbf{p})v_s(-\mathbf{p}) &= 0, \end{aligned} \quad (2.15)$$

they are eigenvectors of  $h(\mathbf{p})$

$$\begin{aligned} h(\mathbf{p})u_r(\mathbf{p}) &= \Omega(\mathbf{p})u_r(\mathbf{p}), \\ h(\mathbf{p})v_r(-\mathbf{p}) &= -\Omega(\mathbf{p})v_r(-\mathbf{p}). \end{aligned} \quad (2.16)$$

and they obey the following ordinary differential equations (ODEs)

$$\begin{aligned} \frac{d}{dt}u_r(\mathbf{P}(t)) &= \frac{1}{2}Q(t, \mathbf{p})v_r(-\mathbf{P}(t)), \\ \frac{d}{dt}v_r(-\mathbf{P}(t)) &= -\frac{1}{2}Q(t, \mathbf{p})u_r(\mathbf{P}(t)), \end{aligned} \quad (2.17)$$

with

$$Q(t, \mathbf{p}) = \frac{eE(t)\epsilon_\perp}{\Omega(\mathbf{P}(t))^2}, \quad \epsilon_\perp = \sqrt{m^2 + p_\perp^2}. \quad (2.18)$$

The quantity  $\epsilon_\perp$  is also called the transverse energy. From (2.16) it is immediately obvious that setting

$$U_r(t, \mathbf{p}) = u_r(\mathbf{P}(t)), \quad V_r(t, -\mathbf{p}) = v_r(-\mathbf{P}(t)) \quad (2.19)$$

satisfies (2.12) and (2.13). These spinors  $U_r$  and  $V_r$  are also orthonormal at all times, thanks to (2.15).

<sup>1</sup>We can always set this value to 0 by a gauge transformation, or equivalently by shifting  $\mathbf{p}$ .

For  $u_r(t, \mathbf{p})$  and  $v_r(t, -\mathbf{p})$  we make the ansatz

$$\begin{aligned} u_r(t, \mathbf{p}) &= \alpha(t, \mathbf{p})U_r(t, \mathbf{p}) + \beta(t, \mathbf{p})V_r(t, -\mathbf{p}), \\ v_r(t, -\mathbf{p}) &= -\beta^*(t, \mathbf{p})U_r(t, \mathbf{p}) + \alpha^*(t, \mathbf{p})V_r(t, -\mathbf{p}). \end{aligned} \quad (2.20)$$

We now insert (2.20) into (2.11) and employ (2.19),(2.17) and (2.12)) to arrive at coupled ODEs for  $\alpha$  and  $\beta$ :

$$\begin{aligned} \dot{\alpha}(t, \mathbf{p}) &= -i\Omega(t, \mathbf{p})\alpha(t, \mathbf{p}) + \frac{1}{2}Q(t, \mathbf{p})\beta(t, \mathbf{p}), \\ \dot{\beta}(t, \mathbf{p}) &= -\frac{1}{2}Q(t, \mathbf{p})\alpha(t, \mathbf{p}) + i\Omega(t, \mathbf{p})\beta(t, \mathbf{p}). \end{aligned} \quad (2.21)$$

The initial conditions (2.13) translate to  $\alpha(t = t_{\text{on}}, \mathbf{p}) = 1$ ,  $\beta(t = t_{\text{on}}, \mathbf{p}) = 0$ . Note that (2.21) implies  $\frac{d}{dt}(|\alpha|^2 + |\beta|^2) = 0$  and, due to the initial condition,  $|\alpha|^2 + |\beta|^2 = 1$ . This makes (2.20) a unitary transformation. With this we have completely specified both bases and we can decompose a general solution  $\psi$  of (2.9) in both of them:

$$\begin{aligned} \psi(t, \mathbf{p}) &= \sum_r \left[ c_r(\mathbf{p})u_r(t, \mathbf{p}) + d_r^\dagger(-\mathbf{p})v_r(t, -\mathbf{p}) \right] \\ &= \sum_r \left[ C_r(t, \mathbf{p})U_r(t, \mathbf{p}) + D_r^\dagger(t, -\mathbf{p})V_r(t, -\mathbf{p}) \right]. \end{aligned} \quad (2.22)$$

The operator  $c_r(\mathbf{p})$  destroys a particle of momentum  $\mathbf{p}$  and spin  $r$ , and  $d_r^\dagger(\mathbf{p})$  creates an anti-particle. They fulfill the usual anti-commutation relations and span our Fock space. Since  $c_r$ ,  $d_r^\dagger$ ,  $u_r$ ,  $v_r$ ,  $U_r$  and  $V_r$  are fixed, we can now define  $C_r$  and  $D_r^\dagger$  in such a way that the second equality in (2.22) holds:

$$\begin{aligned} C_r(t, \mathbf{p}) &= \alpha(t, \mathbf{p})c_r(\mathbf{p}) - \beta^*(t, \mathbf{p})d_r^\dagger(-\mathbf{p}), \\ D_r^\dagger(t, -\mathbf{p}) &= \beta(t, \mathbf{p})c_r(\mathbf{p}) + \alpha^*(t, \mathbf{p})d_r^\dagger(-\mathbf{p}). \end{aligned} \quad (2.23)$$

This is the Bogoliubov transform from  $c_r$ ,  $d_r$  to  $C_r$ ,  $D_r$ .

### 2.2.2 Particle number and quantum kinetic equation

To see the significance of (2.23) let us look at the QED Hamiltonian. We can express (2.5) in terms of  $\psi$  and  $h$  as

$$H(t) = \int \frac{d^3p}{(2\pi)^3} \psi^\dagger(t, \mathbf{p})h(\mathbf{P}(t))\psi(t, \mathbf{p}). \quad (2.24)$$

Inserting (2.22) and taking into account (2.12) and the orthonormality of  $U_r$  and  $V_r$  yields

$$H(t) = \int \frac{d^3p}{(2\pi)^3} \sum_r \Omega(\mathbf{P}(t)) \left[ C_r^\dagger(t, \mathbf{p})C_r(t, \mathbf{p}) - D_r(t, \mathbf{p})D_r^\dagger(t, \mathbf{p}) \right]. \quad (2.25)$$

Thus  $H$  is diagonalized in terms of the operators  $C_r$  and  $D_r$ .

The Bogoliubov transform (2.23) also has the crucial property of leaving the canonical anti-commutation relations intact, that is

$$\begin{aligned} \{c_r(\mathbf{p}), c_s^\dagger(\mathbf{q})\} &= \{C_r(t, \mathbf{p}), C_s^\dagger(t, \mathbf{q})\} = (2\pi)^3 \delta_{rs} \delta(\mathbf{p} - \mathbf{q}), \\ \{d_r(\mathbf{p}), d_s^\dagger(\mathbf{q})\} &= \{D_r(t, \mathbf{p}), D_s^\dagger(t, \mathbf{q})\} = (2\pi)^3 \delta_{rs} \delta(\mathbf{p} - \mathbf{q}) \end{aligned} \quad (2.26)$$

with all other anti-commutators zero. Thus, both sets of operators are creation/annihilation operators of particles with spin  $\frac{1}{2}$  and mass  $m$ . They also define two different vacua,  $|0\rangle$  and  $|\Omega\rangle$ , by  $c_r |0\rangle = d_r |0\rangle = 0$  and  $C_r |\Omega\rangle = D_r |\Omega\rangle = 0$ . Since  $H$  is diagonal in  $C_r$  and  $D_r$ ,  $|\Omega\rangle$  is the (time dependent) ground state of the system.

The number operators  $c_r^\dagger c_r$  and  $C_r^\dagger C_r$  vanish when sandwiched between their respective vacua, but taking their expectation values using the other vacuum yields

$$\langle 0 | C_r^\dagger(t, \mathbf{p}) C_r(t, \mathbf{p}) | 0 \rangle = \langle \Omega(t) | c_r^\dagger(\mathbf{p}) c_r(\mathbf{p}) | \Omega(t) \rangle = |\beta(t, \mathbf{p})|^2 (2\pi)^3 \delta(0). \quad (2.27)$$

This quantity is the number of quasi-particles at time  $t$  produced by the electric field. A rigorous interpretation as an electron number is only possible when  $E$  is switched off, that is for  $t \geq t_{\text{off}}$ . The divergent factor  $(2\pi)^3 \delta(0) = \int d^3x e^{i0x} = \int d^3x$  is just the spatial volume of the homogeneous system, and we drop it by normalizing the particle number by this volume. We thus define the (dimensionless) (quasi-)particle number density  $f$  (including a factor 2 for the spin sum) as

$$f(t, \mathbf{p}) = 2|\beta(t, \mathbf{p})|^2. \quad (2.28)$$

Note that some authors do not include the spin sum in  $f$ , which introduces various factors of two in subsequent formulas. With the help of the auxiliary quantities  $u = -2 \operatorname{Re}(\alpha^* \beta)$  and  $v = 2 \operatorname{Im}(\alpha^* \beta)$  and the ODEs (2.21) we find a set of coupled ODEs for  $f$ :

$$\begin{aligned} \dot{f}(t, \mathbf{p}) &= Q(t, \mathbf{p}) u(t, \mathbf{p}), \\ \dot{u}(t, \mathbf{p}) &= Q(t, \mathbf{p}) (1 - f(t, \mathbf{p})) - 2\Omega(t, \mathbf{p}) v(t, \mathbf{p}), \\ \dot{v}(t, \mathbf{p}) &= 2\Omega(t, \mathbf{p}) u(t, \mathbf{p}), \end{aligned} \quad (2.29)$$

with the initial conditions  $f(t_{\text{on}}) = u(t_{\text{on}}) = v(t_{\text{on}}) = 0$ . This is the quantum kinetic equation (QKE) for the particle number density  $f$ . It was first derived in [57], see also [58].

### 2.2.3 Low-density approximation

The ODE (2.29) is a system of coupled equations which must be solved numerically. To gain analytical insight, approximations are in order. First, let us rewrite (2.29) as an integro-differential equation

$$\dot{f}(t, \mathbf{p}) = Q(t, \mathbf{p}) \int_{t_{\text{on}}}^t dt' Q(t', \mathbf{p}) [1 - f(t', \mathbf{p})] \cos \left( 2 \int_{t'}^t dt'' \Omega(t'', \mathbf{p}) \right). \quad (2.30)$$

The term  $(1 - f)$  in (2.30) is the Pauli blocking factor and arises from the fermion statistics. (In scalar QED it would be  $(1 + f)$ .) It also suggests a suitable approximation: In most cases our density will be small,  $f \ll 1$ , so that we can approximate  $1 - f \approx 1$ . Then the right side of Eq. (2.30) becomes independent of  $f$  and can be integrated to yield

$$f(t, \mathbf{p}) = \frac{1}{2} \left| \int_{t_{\text{on}}}^t dt' Q(t', \mathbf{p}) e^{2i\Theta(t', \mathbf{p})} \right|^2, \quad (2.31)$$

where we introduced the dynamical phase

$$\Theta(t, \mathbf{p}) = \int_{t_{\text{on}}}^t dt' \Omega(\mathbf{P}(t')) = \int_{t_{\text{on}}}^t dt' \sqrt{m^2 + p_{\perp}^2 + (p_z - eA(t'))^2}. \quad (2.32)$$

Equation (2.31) is called the low-density approximation (LDA) and can be checked for self-consistency. If the resulting  $f$  is  $\mathcal{O}(1)$ , then the LDA can no longer be valid, and thus the result is unphysical. In this case, one must resort to solving the full equation (2.30) which is equivalent to (2.29).

We can also derive the LDA for the Bogoliubov coefficients themselves in a more systematic way. Recall the definition of  $Q$  given in Eq. (2.18):  $Q(t, \mathbf{p}) = eE(t)\epsilon_{\perp}/\Omega(t, \mathbf{p})^2$ , that is  $Q \propto E$ . We can solve (2.21) in a series expansion by inserting a parameter  $\epsilon$  in front of  $Q$  and in the end setting  $\epsilon = 1$ .<sup>2</sup> We get the modified equation

$$\frac{d}{dt} \begin{pmatrix} \alpha \\ \beta \end{pmatrix} = \left[ \begin{pmatrix} -i\Omega & 0 \\ 0 & i\Omega \end{pmatrix} + \epsilon \begin{pmatrix} 0 & \frac{Q}{2} \\ -\frac{Q}{2} & 0 \end{pmatrix} \right] \begin{pmatrix} \alpha \\ \beta \end{pmatrix}. \quad (2.33)$$

Now we make a series ansatz for both coefficients:  $\alpha = \sum_n \epsilon^n \alpha_n$  and  $\beta = \sum_n \epsilon^n \beta_n$ . Inserting into (2.33) and comparing by powers of  $\epsilon$  yields a set of recursive ODEs:

$$\begin{aligned} \dot{\alpha}_{n+1} &= -i\Omega\alpha_{n+1} + \frac{Q}{2}\beta_n, & \dot{\alpha}_0 &= -i\Omega\alpha_0, \\ \dot{\beta}_{n+1} &= -\frac{Q}{2}\alpha_n + i\Omega\beta_{n+1}, & \dot{\beta}_0 &= i\Omega\beta_0, \end{aligned} \quad (2.34)$$

which, upon utilizing the initial conditions  $\alpha(t = t_{\text{on}}) = 1$  and  $\beta(t = t_{\text{on}}) = 0$ , integrate to

$$\begin{aligned} \alpha_{n+1}(t) &= e^{-i\Theta(t)} \int_{t_{\text{on}}}^t dt' \beta_n(t') \frac{Q(t')}{2} e^{i\Theta(t')}, & \alpha_0(t) &= e^{-i\Theta(t)}, \\ \beta_{n+1}(t) &= -e^{i\Theta(t)} \int_{t_{\text{on}}}^t dt' \alpha_n(t') \frac{Q(t')}{2} e^{-i\Theta(t')}, & \beta_0(t) &= 0. \end{aligned} \quad (2.35)$$

The first non-vanishing term for  $\beta$  is

$$\beta_1(t, \mathbf{p}) = -\frac{1}{2} e^{i\Theta(t, \mathbf{p})} \int_{t_{\text{on}}}^t dt' Q(t', \mathbf{p}) e^{-2i\Theta(t', \mathbf{p})} \quad (2.36)$$

which inserted into  $f = 2|\beta|^2$  yields (2.31).

### 2.3 Electrical fields

In our subsequent discussions of pair production, we will use three types of time dependent electric fields, which we describe in this section along with simple analytical properties.

---

<sup>2</sup>This is equivalent to an expansion in the electric field  $E$ , but more notationally convenient.



### 2.3.1 Schwinger field

In this case the electric field is constant:

$$A(t) = -E_0 t, \quad E(t) = E_0. \quad (2.37)$$

This is the field used in the first studies of vacuum decay and pair production [4, 5]. It does not conform to our convention of being switched on at  $t = t_{\text{on}}$  and off at  $t = t_{\text{off}}$ , but that can be overcome by a limiting procedure of first calculating  $f$  and then sending  $t_{\text{on}} \rightarrow -\infty$  and  $t_{\text{off}} \rightarrow \infty$ . Analytical solutions can thus be derived in terms of the parabolic cylinder functions  $D_a(z)$  (see [86]):

$$\begin{aligned} f(t, \mathbf{p}) &= \frac{1}{4} \left( 1 + \frac{u}{\sqrt{2\eta + u^2}} \right) e^{-\frac{\pi\eta}{4}} |A - B|^2, \\ A &= \left( \sqrt{2\eta + u^2} - u \right) D_{-1+\frac{i\eta}{2}} \left( -ue^{-\frac{i\pi}{4}} \right), \quad B = 2e^{\frac{i\pi}{4}} D_{+\frac{i\eta}{2}} \left( -ue^{-\frac{i\pi}{4}} \right), \\ u &= \sqrt{\frac{2}{eE_0}} (p_z + eE_0 t), \quad \eta = \frac{\epsilon_{\perp}^2}{eE_0}. \end{aligned} \quad (2.38)$$

Schwinger's seminal result is recovered by computing the total pair creation rate

$$\dot{N} = \int d^3 p f(t, \mathbf{p}) = \frac{(eE_0)^2}{4\pi^3} e^{-\frac{\pi m^2}{eE_0}}. \quad (2.39)$$

### 2.3.2 Sauter pulse

This pulse type depends on a timescale  $\tau$  in addition to the scale  $E_0$ :

$$A(t) = -E_0 \tau \tanh \frac{t}{\tau}, \quad E(t) = \frac{E_0}{\cosh^2 \frac{t}{\tau}}. \quad (2.40)$$

A plot of the time dependencies is shown in Fig. 2.1. It obeys our switch-on/off convention only asymptotically, but that can be handled in the same way as for the Schwinger field. Analytical solutions for  $f$  can again be obtained (see [86]), similar in form to (2.38), but instead of the parabolic cylinder functions one utilizes the hypergeometric function  ${}_2F_1$ :

$$\begin{aligned} f(t, \mathbf{p}) &= \frac{1 + \frac{P_z}{\Omega(t, \mathbf{p})}}{2\Omega(-\infty, \mathbf{p}) [\Omega(-\infty, \mathbf{p}) - p_z + eE_0 \tau]} |A + iB|^2, \\ A &= \frac{2}{\tau} u(1-u) \frac{ab}{c} {}_2F_1(1+a, 1+b, 1+c; u), \\ B &= [\Omega(t, \mathbf{p}) - (1-u)\Omega(-\infty, \mathbf{p}) - u\Omega(\infty, \mathbf{p})] {}_2F_1(a, b, c; u), \\ u &= \frac{1}{2} (1 + \tanh \frac{t}{\tau}), \quad a = -ieE_0 \tau^2 - \frac{i\tau\Omega(-\infty, \mathbf{p})}{2} + \frac{i\tau\Omega(\infty, \mathbf{p})}{2}, \\ b &= 1 + ieE_0 \tau^2 - \frac{i\tau\Omega(-\infty, \mathbf{p})}{2} + \frac{i\tau\Omega(\infty, \mathbf{p})}{2}, \quad c = 1 - i\tau\Omega(-\infty, \mathbf{p}). \end{aligned} \quad (2.41)$$

Two examples of the time evolution resulting from (2.38) and (2.41) are shown in Fig. 2.2 for different field strengths. As the length of the Sauter pulse  $\tau$  is increased, its solution

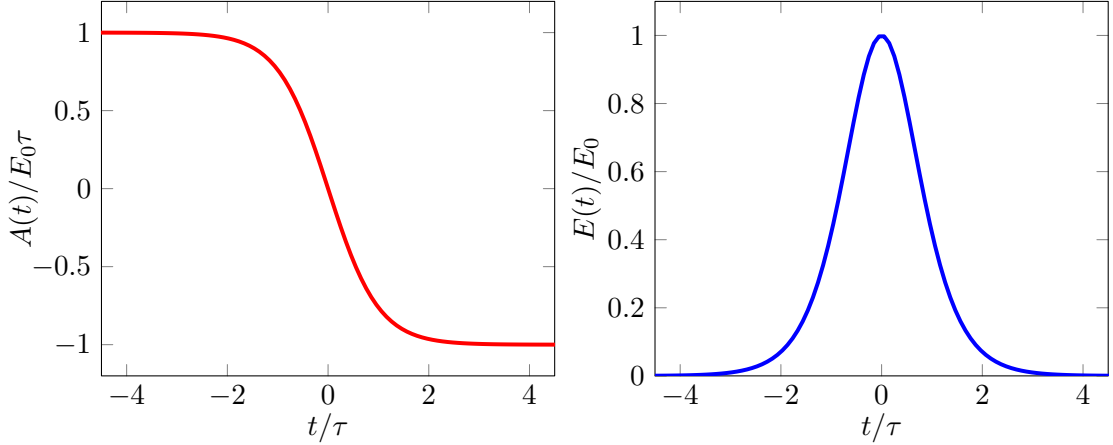


**Figure 2.1:** Plots of the time evolution of the vector potential (left) and electric field (right) for the Sauter pulse (2.40).

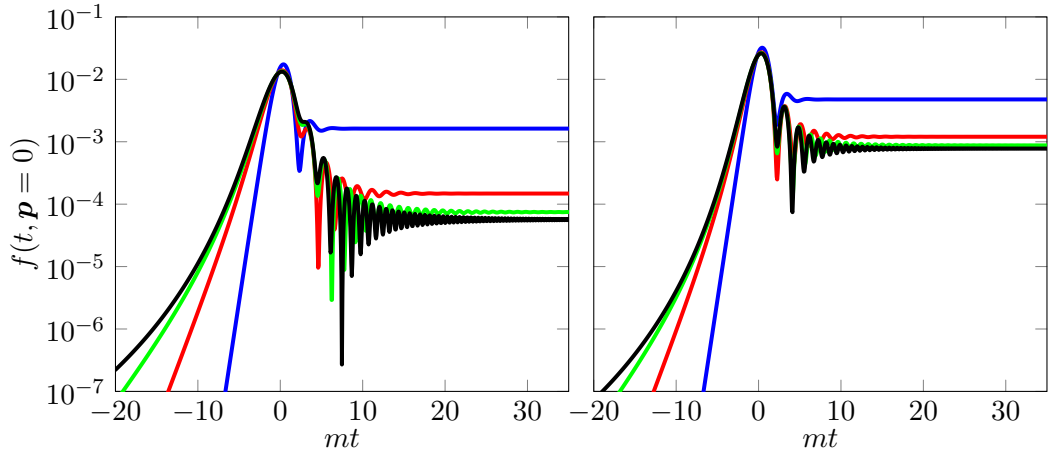


**Figure 2.2:** Time evolution of the pair density  $f$  for Schwinger (black) and Sauter pulse (blue:  $\tau = 2/m$ ; red:  $\tau = 5/m$ ; green:  $\tau = 10/m$ ) at  $\mathbf{p} = 0$ . The field strength is  $E_0 = 0.3E_c$  in the left and  $E_0 = 0.4E_c$  in the right panel. The fields for the Schwinger field are given by (2.37) and its solution by (2.38). For the Sauter pulse, the corresponding equations are (2.40) and (2.41).

approaches the Schwinger case. This is of course expected, since the limit  $\tau \rightarrow \infty$  of (2.40) is just (2.37).

We also note that  $f$  reaches an intermediate maximum far greater than its residual value  $f(t \rightarrow \infty)$ .<sup>3</sup> This is a generic feature also present in other pulse types. It begs the question whether the number of intermediate quasi-particles has any physical significance. By the standard rules of QFT, only asymptotic states are physical, thus only  $f(t \rightarrow \pm\infty)$  can be interpreted as a pair density. What then does it represent in between asymptotic times? And given that the residual number for realistically achievable pulse parameters has as of yet been too small to measure, could this be an avenue for detecting the dynamical Schwinger effect experimentally? We will keep these questions in mind.

<sup>3</sup>For example, in the left panel of Fig. 2.2 the maximum value for the Schwinger pulse is about  $10^3$  times greater than its asymptotic value.

An important dimensionless quantity can be formed from the physical quantities  $e$ ,  $m$  and the parameters  $E_0$ ,  $\tau$ : the Keldysh parameter  $\gamma$ . It is defined by

$$\gamma = \frac{m}{eE_0\tau} = \frac{E_c}{E_0} \frac{1}{m\tau}. \quad (2.42)$$

One can think of it as relating the energy scales inherent in  $E_0$  and  $\tau$ . It is used to distinguish two cases. For  $\gamma \ll 1$  we say the field is in the adiabatic or tunneling regime. There it is expected to behave mostly like the Schwinger field, i.e. it acts mostly through its field strength and not the energy inherent due to its time dependence. For  $\gamma \gg 1$ , on the other hand, we say the field is in the multiphoton or perturbative regime. As the name suggests, it should behave mostly as an ensemble of many quanta with frequencies due to the time scale. Perturbation theory in the external field might be applicable for some calculations here, but unlikely to succeed in the adiabatic regime. These are, however, mainly illustrations meant to stimulate one's intuition and should be taken with a grain of salt. In particular, one should not exclusively depend on the Keldysh parameter for classifying fields, but rather look at the total parameter space spanned by the two dimensionless quantities  $E_0/E_c$  and  $m\tau$ .

### 2.3.3 Periodic pulse

Both the Schwinger and Sauter pulses have the advantage that the QKE can be solved analytically with known functions when they are used as background fields. The usefulness of these solutions can be questioned, however, since they look fairly intractable and it is difficult to extract analytical predictions from them.

A major problem exists in their physical relevance. Since  $A(t_{\text{on}}) > A(t_{\text{off}})$  the fields contain a DC component which must have an electric charge as a source. So they cannot correctly model a solution of Maxwell's equations in vacuum, e.g. a laser, even under our relaxed assumption of a spatially homogeneous field.

A more realistic approach is to consider a periodic  $A$  field with frequency  $\nu$  modulated by an envelope  $K$ :

$$A(t) = K(t) \frac{E_0}{\nu} \cos \nu t, \quad E(t) = K(t) E_0 \sin \nu t - \dot{K}(t) \frac{E_0}{\nu} \cos \nu t. \quad (2.43)$$

The frequency is in one to one relation to the time scale  $\tau$  that we used for the Sauter pulse:  $\nu = 1/\tau$ . Then the Keldysh parameter is  $\gamma = \frac{E_c \nu}{E_0 m}$ .<sup>4</sup> The period of the oscillations is  $T = 2\pi/\nu$ . It is possible to add a carrier envelope phase  $\varphi_0$  to the field (2.43) by substituting  $\nu t \rightarrow \nu t + \varphi_0$ . However, since we expect it to be of minor importance for fields with a large number of oscillations under the envelope, and since we would like to keep our parameter space small, we do not add it.

For the envelope  $K$  one might choose for example a window function [87] or a Gaussian [88]. But we want our envelope to have three properties, some of which those two examples do not exhibit:

<sup>4</sup>We thought a frequency looks more natural for an oscillating field, and a timescale for a Gaussian-like field, since the latter is just a measure for its width.

1. Smoothness, preferably  $K \in C^\infty$ .
2. Make  $E$  fulfill the switch-on/off conditions and do not let  $A$  acquire a DC component, e.g. by setting  $K(t_{\text{on}}) = K(t_{\text{off}}) = 0$ .
3. Be constant over a preferably large time interval.

Modulating the  $A$  field by the envelope instead of the  $E$  field has two advantages: It is easy to eliminate the DC component and we do not have to integrate  $A$  over time (most likely numerically) to get  $E$ . Had we multiplied  $E$  by  $K$ , careful picking of the parameters would have been necessary to ensure  $A(t_{\text{off}}) = A(t_{\text{on}})$ . We therefore construct an envelope function satisfying our criteria using the two helper functions

$$r(x) = \begin{cases} 0, & x \leq 0 \\ e^{-\frac{1}{x}}, & x > 0 \end{cases}, \quad s(x) = \frac{r(x)}{r(x) + r(1-x)}. \quad (2.44)$$

Indeed,  $r \in C^\infty$  but it is not analytical, since  $r^{(n)}(x) = 0$ , so every term of its Taylor series around  $x = 0$  is zero. This carries over to  $s$ , which is defined in terms of  $r$  (and its denominator can never be zero). We also note that  $s(x \leq 0) = 0$  and  $s(x \geq 1) = 1$ . Defining our envelope by

$$K(t) = s\left(\frac{t}{t_{\text{ramp}}}\right) s\left(\frac{t_{\text{flat}} - 2t_{\text{ramp}} - t}{t_{\text{ramp}}}\right) \quad (2.45)$$

fulfills these three properties:

1.  $K \in C^\infty$  since  $s$  is.
2.  $K(t \leq 0) = K(t \geq t_{\text{flat}} + 2t_{\text{ramp}}) = 0$ , so  $t_{\text{on}} = 0$  and  $t_{\text{off}} = t_{\text{flat}} + 2t_{\text{ramp}}$ .
3.  $K(t) = 1$  for  $t_{\text{ramp}} \leq t \leq t_{\text{flat}} + t_{\text{ramp}}$ .

The  $A$  field is thus switched on smoothly in  $[0, t_{\text{ramp}})$ , the duration of which is controlled by the ramping time  $t_{\text{ramp}}$ . It then oscillates with constant amplitude in  $[t_{\text{ramp}}, t_{\text{flat}} + t_{\text{ramp}}]$  for the duration of the flat-top interval  $t_{\text{flat}}$ , and is again switched off smoothly in  $(t_{\text{flat}} + t_{\text{ramp}}, t_{\text{flat}} + 2t_{\text{ramp}}]$  with the same duration as the switch-on process,  $t_{\text{ramp}}$ .<sup>5</sup> Both parameters,  $t_{\text{ramp}}$  and  $t_{\text{flat}}$ , can be chosen independently of each other and to arbitrary positive values. For example, setting  $t_{\text{ramp}} = 0$  the resulting envelope is just a window function,  $K(t) = \theta(t)\theta(t_{\text{flat}} - t)$ . On the other hand, setting  $t_{\text{flat}} = 0$  there will be no interval of constant amplitude; the field is switched on, and immediately off again.

We will mainly restrict ourselves to the case where  $t_{\text{ramp}} \ll t_{\text{flat}}$ , so the resulting fields are as close as physically reasonable to pure oscillating fields. It is, however, also necessary to not make  $t_{\text{ramp}}$  too small, because since  $\dot{K}(t) = \mathcal{O}(1/t_{\text{ramp}})$  in the switching-on/off region this would create large spikes in the  $E$  field. This is also why using a window function is very much unphysical. It creates a delta-function spike in the electric field. We will later see that  $f$  oscillates rapidly with the periodic field as input. Suddenly switching off simply “freezes” the density  $f$  in place, and that will be highly sensitive to when the switching-off

---

<sup>5</sup>One might have chosen two different timescales for switching on and off, but that seemed an unnecessary enlargement of the parameter space with no expected additional insights.

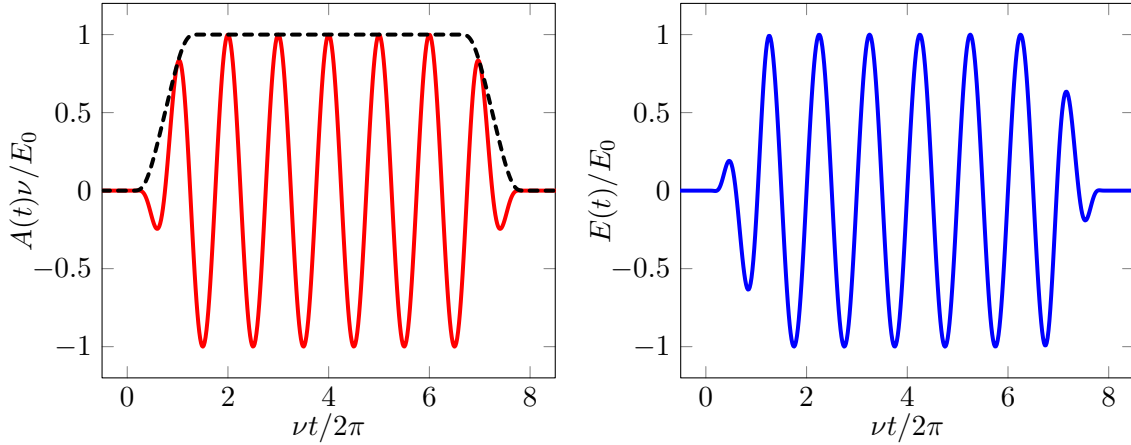


**Figure 2.3:** Plot of the time evolution of the vector potential (left) and electric field (right) for the periodic pulse (2.43). The envelope  $K$  is shown as a dashed black curve in the left panel. Its parameters are  $t_{\text{ramp}} = 1.5T$  and  $t_{\text{flat}} = 5T$ .

occurred. The densities thus obtained have little value. One can get what one wants by suitably setting the switch-off time. In contrast, slowly switching off makes the oscillations slowly vanish and  $f$  converge to a value, that varies slowly with  $t_{\text{ramp}}$ . Thus we require  $t_{\text{ramp}}$  to be at least a few oscillations of the modulated function, e.g.  $t_{\text{ramp}} \gtrsim 3T$ . The values we will most often use are  $t_{\text{ramp}} = 5T$  and  $t_{\text{flat}} = 50T$ .

Plots of the  $A$  field and the resulting  $E$  field are shown in Fig. 2.3. The envelope  $K$  is superimposed over  $A$  as a dashed black curve. Both parameters for the envelope are relatively small in the plots compared to what we will usually use. This ensures there are not too many oscillations of the fields under the envelope, which would be impossible to plot right.

## 2.4 Numerics

Before we turn to analytical approaches, let us describe some details of our numerical implementation for the periodic pulse, since this will be used throughout to check the analytical results.

### 2.4.1 Dimensionless quantum kinetic equation

The first step of implementing a numerical algorithm is often to define dimensionless quantities that correspond to the real ones, because computers can only be programmed with dimensionless floats.<sup>6</sup> We denote the dimensionless variant of a variable or function

<sup>6</sup>There are in fact libraries for using dimensional quantities in code directly, e.g. [89], but they are not widely used and often introduce some overhead.

by putting a hat over them, e.g.  $t \rightarrow \hat{t}$ . Their definitions read

$$\begin{aligned} \hat{t} &= \nu t, \quad \hat{\mathbf{p}} = \frac{\mathbf{p}}{m}, \quad \hat{A}(\hat{t}) = \frac{eA(t)}{m}, \quad \hat{E}(\hat{t}) = \frac{eE(t)}{m^2} = \frac{E(t)}{E_c}, \\ \hat{\Omega}(\hat{t}, \hat{\mathbf{p}}) &= \frac{\Omega(t, \mathbf{p})}{m} = \sqrt{1 + \hat{p}_\perp^2 + (\hat{p}_\parallel - \hat{A}(\hat{t}))^2}, \quad \hat{Q}(\hat{t}, \hat{\mathbf{p}}) = \frac{Q(t, \mathbf{p})}{m} = \frac{\hat{E}(\hat{t})\epsilon_\perp}{\hat{\Omega}(\hat{t}, \hat{\mathbf{p}})}. \end{aligned} \quad (2.46)$$

Note that  $\alpha$ ,  $\beta$ ,  $f$ ,  $u$  and  $v$  are already dimensionless. Our dimensionless version of Eq. (2.21) for the Bogoliubov coefficients is then

$$\frac{d}{d\hat{t}} \begin{pmatrix} \alpha \\ \beta \end{pmatrix} = \frac{m}{\nu} \begin{pmatrix} -i\hat{\Omega} & \hat{Q}/2 \\ -\hat{Q}/2 & i\hat{\Omega} \end{pmatrix} \begin{pmatrix} \alpha \\ \beta \end{pmatrix} \quad (2.47)$$

and the QKE (2.29) reads

$$\frac{d}{d\hat{t}} \begin{pmatrix} f \\ u \\ v \end{pmatrix} = \frac{m}{\nu} \begin{pmatrix} 0 & \hat{Q} & 0 \\ -\hat{Q} & 0 & -2\hat{\Omega} \\ 0 & 2\hat{\Omega} & 0 \end{pmatrix} \begin{pmatrix} f \\ u \\ v \end{pmatrix} + \frac{m}{\nu} \begin{pmatrix} 0 \\ \hat{Q} \\ 0 \end{pmatrix}. \quad (2.48)$$

There are four dimensionless constants that enter the equations:

1. The dimensionless field strength  $E_0/E_c$ .
2. The dimensionless frequency  $\nu/m$ .
3. The dimensionless ramping and flat-top times,  $\nu t_{\text{ramp}}$  and  $\nu t_{\text{flat}}$ .

We can write our fields exclusively in terms of them:

$$\begin{aligned} \hat{A}(\hat{t}) &= K(\hat{t}) \frac{m E_0}{\nu E_c} \cos \hat{t}, \quad \hat{E}(\hat{t}) = K(\hat{t}) \frac{E_0}{E_c} \sin \hat{t} - K'(\hat{t}) \frac{E_0}{E_c} \cos \hat{t}, \\ K(\hat{t}) &= s \left( \frac{\hat{t}}{\nu t_{\text{ramp}}} \right) \cdot s \left( \frac{\nu t_{\text{flat}} - 2\nu t_{\text{ramp}} - \hat{t}}{\nu t_{\text{ramp}}} \right). \end{aligned} \quad (2.49)$$

### 2.4.2 Implementation details

We have translated our equations into a form suitable for computers. All those hats are however not easy on the eye, so we will always refer to the dimensional unhatted quantities and equations with the understanding that they need to be translated with the above prescriptions where needed.

Both Eqs. (2.21) and (2.29) are ordinary, linear differential equations of first order. There is, crucially, no coupling between different momenta  $\mathbf{p}$ . The problem thus becomes what is sometimes called “embarrassingly parallel”, i.e. we can compute solutions to the equations independently for different momenta and parameters and distribute the computations to as many processors as our resources allow.

Numerical methods for solving ODEs are plentiful, see for example [90] for an introduction and overview. Implementing them correctly and efficiently is a difficult task in its own

right, which we will not attempt in the course of this work. Instead we use the C++ library `odeint` [91] which provides a wide variety of algorithms. In particular, one can choose between different solvers, such as Runge-Kutta schemes of various order, the Bulirsch-Stoer algorithm or Rosenbrock methods. After some explorations, we settled on its `runge_kutta_fehlberg78` template class as a stepper and its `integrate_adaptive` procedure for integration of the equations.

The implementation works well for large field strengths and frequencies, e.g.  $E_0 = \mathcal{O}(0.1E_c)$  and  $\nu = \mathcal{O}(0.5m)$ . Trying to make these parameters smaller to approach more realistic values exposes two problems. Lowering  $E_0$  rapidly reduces the residual pair density  $f$  to the point where it is much smaller than the machine precision. Lowering  $\nu$  on the other hand makes  $m/\nu \gg 1$ . This significantly increases the time it takes for the algorithm to solve the equation. In fact, we found “experimentally” that the computational complexity is  $\mathcal{O}((m/\nu)^2)$ . In practice, one cannot go much lower than  $E_0 = 10^{-2}E_c$  and  $\nu = 10^{-3}m$  with presently available resources.

### 2.4.3 Exploiting periodicity

The naive algorithm for integrating over the entire time  $t_{\text{ramp}} + t_{\text{flat}} + t_{\text{ramp}}$  is linear in those times, i.e.  $\propto \mathcal{O}(t_{\text{ramp}}) + \mathcal{O}(t_{\text{flat}})$ . We can make use of the periodicity of our fields in the flat-top region and employ Floquet’s theorem to lower this to  $\mathcal{O}(t_{\text{ramp}}) + \mathcal{O}(\log t_{\text{flat}})$ . This makes integrating over the flat-top region take much less time than one needs for the switching-on/off.

We will explain this method for the Bogoliubov coefficients and their equation (2.21), but it works equally well for Eq. (2.29). We first rewrite (2.21) into a matrix differential equation:

$$\dot{U}(t, t_0) = M(t)U(t, t_0), \quad U(t_0, t_0) = \mathbb{1}, \quad (2.50)$$

$$U = \begin{pmatrix} \alpha & -\beta^* \\ \beta & \alpha^* \end{pmatrix}, \quad M = \begin{pmatrix} -i\Omega & Q/2 \\ -Q/2 & i\Omega \end{pmatrix}. \quad (2.51)$$

Note that  $M$  is skew-Hermitian, i.e. a solution  $U$  must be unitary and a one-parameter group, that is  $U(t_2, t_0) = U(t_2, t_1)U(t_1, t_0)$ . The entire time evolution can then be separated into  $U(t_{\text{flat}} + 2t_{\text{ramp}}, 0) = U(t_{\text{flat}} + 2t_{\text{ramp}}, t_{\text{flat}} + t_{\text{ramp}})U(t_{\text{flat}} + t_{\text{ramp}}, t_{\text{ramp}})U(t_{\text{ramp}}, 0)$ . In the flat-top interval, the matrix  $M$  is periodic with period  $T = 2\pi/\nu$ :  $M(t + T) = M(t)$  for  $t_{\text{ramp}} \leq t < t + T \leq t_{\text{flat}} + t_{\text{ramp}}$ . By Floquet’s theorem (see e.g. [92]), the middle part of  $U$  can be written as a product of a periodic matrix and an exponential:

$$U(t, t_{\text{ramp}}) = P(t - t_{\text{ramp}})e^{R(t - t_{\text{ramp}})}, \quad \text{for } t_{\text{ramp}} \leq t \leq t_{\text{flat}} + t_{\text{ramp}}, \quad (2.52)$$

$$P(t + T) = P(t), \quad R = \text{const.}$$

In particular, we have  $P(T) = \mathbb{1}$ , so that, if  $t_{\text{flat}} = nT$  for an integer  $n$ ,  $U(t_{\text{flat}} + t_{\text{ramp}}, t_{\text{ramp}}) = e^{nRT} = e^{RT^n} = U(t_{\text{ramp}} + T, t_{\text{ramp}})^n$ . Taking a matrix to the power of  $n$  can be done in  $\mathcal{O}(\log n)$  steps. Calculating  $U(t_{\text{ramp}} + T, t_{\text{ramp}})$  is constant time w.r.t.  $t_{\text{ramp}}$  and  $t_{\text{flat}}$ . The algorithm for computing the total time evolution is then clear:

1. Compute  $U_1 = U(t_{\text{ramp}}, 0)$  in  $\mathcal{O}(t_{\text{ramp}})$  time.

2. Compute  $U_2 = U(t_{\text{ramp}} + T, t_{\text{ramp}})$  in constant time.
3. Compute  $U_3 = U(t_{\text{flat}} + 2t_{\text{ramp}}, t_{\text{flat}} + t_{\text{ramp}})$  in  $\mathcal{O}(t_{\text{ramp}})$  time.<sup>7</sup>
4. Compute  $U_2^n$  in  $\mathcal{O}(\log n) = \mathcal{O}(\log t_{\text{flat}})$  time.
5. Compute the result  $U(t_{\text{flat}} + 2t_{\text{ramp}}, 0) = U_3 U_2^n U_1$  in constant time.

Adding up the time complexities for each step yields the claimed result. We just assumed  $t_{\text{flat}} = nT$  with integer  $n$  for exposition's sake. The algorithm can be generalized, with the same time complexity to arbitrary  $t_{\text{flat}}$ .

## 2.5 Phase space structure and time evolution for the periodic pulse

With the preliminaries out of the way, let us look at analytical properties that can be derived for  $f$  with the periodic pulse as background. From the outset, we will make two simplifications: We will use the low-density approximation (2.31) to derive our results and we will neglect effects of the switching-on/off process introduced by the envelope  $K$  in (2.43). This allows for a Fourier analysis similar to [93, 94], but we will get some more insights about the detailed spectrum and the time evolution. The validity of the results will be justified by comparing them with the numerical computations. Tackling the problem of treating the switching-on/off analytically was done in [85].

### 2.5.1 Fourier analysis within the low-density approximation

The pair density  $f$  in the low-density approximation (2.31) is just the squared modulus of some function, which we shall call  $I$ . Explicitly,

$$I(t, \mathbf{p}) = \int_{t_{\text{on}}}^t dt' Q(t', \mathbf{p}) e^{2i\Theta(t', \mathbf{p})} \quad (2.53)$$

and  $f = \frac{1}{2}|I|^2$ . Recall that we fixed  $t_{\text{on}} = 0$  for the periodic pulse. In the flat-top interval the  $A$  field is periodic with period  $T = 2\pi/\nu$  and even,  $A(-t) = A(t)$ . This carries over to  $\Omega(t, \mathbf{p}) = \Omega(\mathbf{p} - e\mathbf{A}(t))$  which can therefore be written as a Fourier series

$$\begin{aligned} \Omega(t, \mathbf{p}) &= \sum_{n=0}^{\infty} \Omega_n(\mathbf{p}) \cos(n\nu t), \\ \Omega_0(\mathbf{p}) &= \frac{1}{T} \int_0^T dt \Omega(t, \mathbf{p}), \quad \Omega_{n>0}(\mathbf{p}) = \frac{2}{T} \int_0^T dt \Omega(t, \mathbf{p}) \cos(n\nu t). \end{aligned} \quad (2.54)$$

---

<sup>7</sup>In fact, for  $t_{\text{flat}} = nT$  we must have  $U_3 = U_1^\dagger$ .



The dynamical phase  $\Theta$  in (2.53) is just the time integral of  $\Omega$ , so we have

$$\Theta(t, \mathbf{p}) = \int_0^t dt' \Omega(t', \mathbf{p}) = \Omega_0(\mathbf{p})t + \sum_{n=1}^{\infty} \frac{\Omega_n(\mathbf{p})}{n} \sin \nu t = \Omega_0(\mathbf{p})t + P(t, \mathbf{p}), \quad (2.55)$$

where  $P$  (no relation to the quantity  $P$  in section 2.4.3!) is again  $T$ -periodic in  $t$ . Inserting this in (2.53) yields

$$I(t, \mathbf{p}) = \int_0^t dt' Q(t', \mathbf{p}) e^{2iP(t', \mathbf{p})} e^{2i\Omega_0(\mathbf{p})t'}. \quad (2.56)$$

The function  $Qe^{2iP}$  is again  $T$ -periodic and we thus expand it again in a (now complex) Fourier series:

$$Q(t, \mathbf{p}) e^{2iP(t, \mathbf{p})} = \sum_{n=-\infty}^{\infty} I_n(\mathbf{p}) e^{-in\nu t}, \quad I_n(\mathbf{p}) = \frac{1}{T} \int_0^T dt Q(t, \mathbf{p}) e^{2iP(t, \mathbf{p})} e^{in\nu t}, \quad (2.57)$$

so that

$$I(t, \mathbf{p}) = \int_0^t dt' \sum_n I_n(\mathbf{p}) e^{-in\nu t'} e^{2i\Omega_0(\mathbf{p})t'} = \sum_n iI_n(\mathbf{p}) \frac{e^{i(n\nu - 2\Omega_0(\mathbf{p}))t} - 1}{n\nu - 2\Omega_0(\mathbf{p})}. \quad (2.58)$$

The denominator  $n\nu - 2\Omega_0(\mathbf{p})$  can become zero for suitable values  $n$  and  $\mathbf{p}$ , and in this case  $I$  and consequently  $f$  will be large (although, it turns out, not divergent). The equation

$$2\Omega_0(\mathbf{p}) = n\nu \quad (2.59)$$

defines structures in phase space that we call shells or ridges. It is fulfilled by certain momenta  $\mathbf{p}$  forming a submanifold of phase space for each integer  $n$ , which we call the shell or ridge number.

Before analyzing this further, let us verify it with numerics. Figure 2.4 shows a contour plot of the residual density  $f$ , after the field has been switched off, over phase space (the  $p_{\perp}$ - $p_{\parallel}$  plane). The parameters used are  $E_0 = 0.2E_c$  and  $\nu = 0.02m$ , leading to a Keldysh parameter of  $\gamma = 0.1$ , putting the field in the adiabatic regime. One can clearly see sharp shells/ridges arising in phase space where  $f$  gets large (note the logarithmic scale for the color map). Different shells correspond to different values of  $n$ . They are not equal distances apart, nor are they simple circles in phase space but elongated, ellipse like along the  $p_{\parallel}$  axis (note the scales are different on the axes). This can be better seen in Fig. 2.5 which depicts cuts through the phase space shown in the contour plot. The numbers  $n$  corresponding to the shells are plotted above the peaks. They are clearly spaced further apart in the right panel along the  $p_{\parallel}$  direction than in the left panel, the  $p_{\perp}$  direction. The density drops for larger  $|\mathbf{p}|$ , but more slowly in the  $p_{\parallel}$  direction than in the  $p_{\perp}$  direction.

To understand the shells' location and shape, one must investigate the Fourier zero mode  $\Omega_0$ . Without a background field we simply have usual dispersion relation  $\Omega_0(\mathbf{p})|_{A=0} = \Omega(\mathbf{p}) = \sqrt{m^2 + \mathbf{p}^2}$ . It starts off as a parabola for small values of  $|\mathbf{p}|$  and then tapers of to a straight line for  $|\mathbf{p}| \gg m$ . That is also the basic form for a general function  $\Omega_0(\mathbf{p})$ . It explains the distances between successive shells: The first shells are far apart, since the

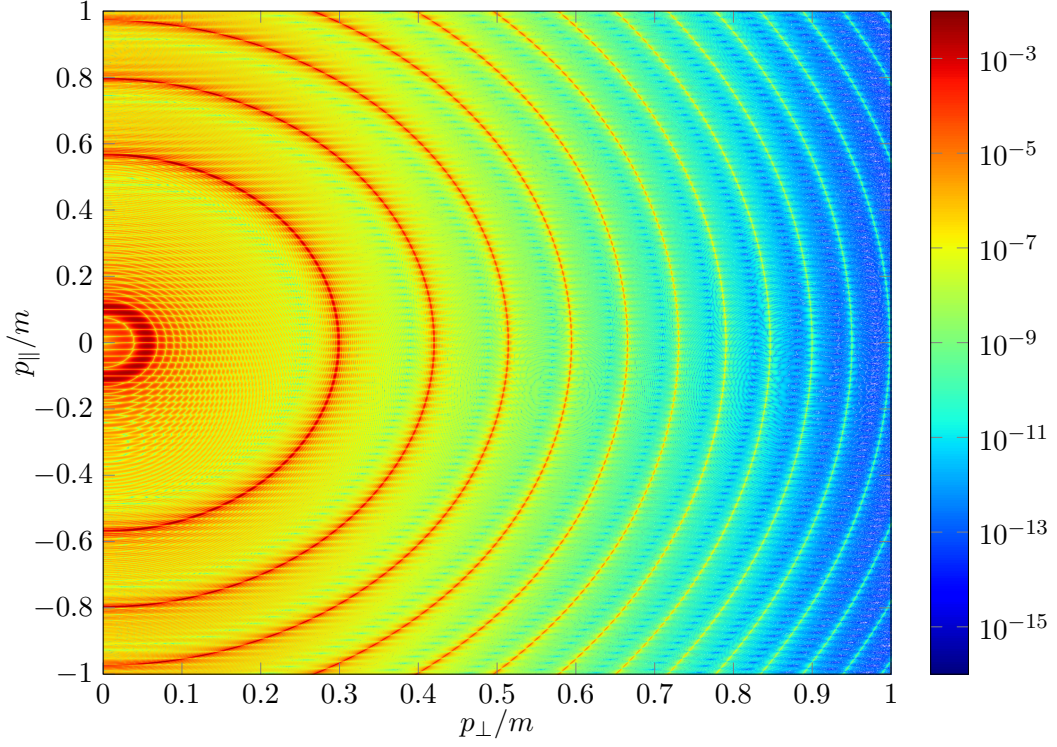


**Figure 2.4:** Contour plot of the pair density  $f$  over the phase space  $p_{\perp}$ - $p_{\parallel}$  with parameters  $E_0 = 0.2E_c$ ,  $\nu = 0.02m$ ,  $t_{\text{ramp}} = 5T$ ,  $t_{\text{flat}} = 50T$ . Loci of momenta, where  $2\Omega_0(\mathbf{p}) = n\nu$ , form sharp ridges where  $f$  becomes large.

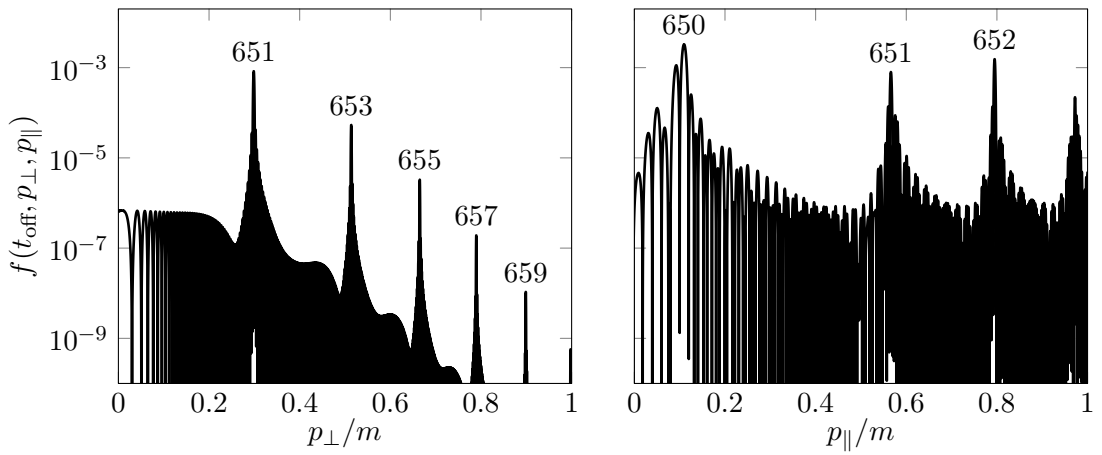


**Figure 2.5:** Cut through the phase space contour plot in Fig. 2.4 for  $p_{\parallel} = 0$  (left) and  $p_{\perp} = 0$  (right). The shell number  $n$  is displayed above the ridge peaks.

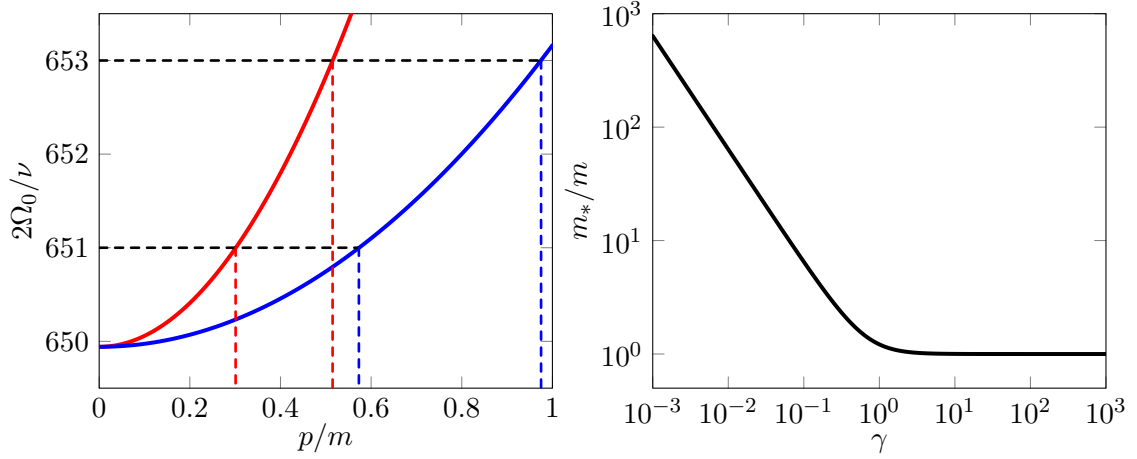


**Figure 2.6:** Left panel: Plot of the Fourier zero mode  $\Omega_0$  as a function of  $p_\perp$ ,  $p_\parallel = 0$  (red) or a function of  $p_\parallel$ ,  $p_\perp = 0$  (blue) with parameters  $E_0 = 0.2E_c$ ,  $\nu = 0.02m$ . Example solutions for  $2\Omega_0 = 651\nu$  and  $2\Omega_0 = 653\nu$  are indicated by the dashed lines. Right panel: Plot of the effective mass  $m_*$  given by Eq. (2.60) as a function of the Keldysh parameter  $\gamma$ .

parabola has little slope. Further out they are equidistant, since the slope of a straight line is constant. This is illustrated in the left panel of Fig. 2.6. Notice that  $\Omega_0$  grows more slowly in the  $p_\parallel$  direction than in the  $p_\perp$  direction. Therefore the shell radii are larger in the former direction than in the latter one, which explains the elongated shell shape in Fig. 2.4 and the peaks being spread further apart in the right panel of Fig. 2.5 than in the left panel.

We can interpret the ridge-determining equation (2.59) in the following way: The Dirac field absorbs  $n$  quanta of the background field with energy  $\nu$  to create a pair (the factor 2) of quasi-particles with momentum  $\mathbf{p}$  and energy  $\Omega_0(\mathbf{p})$ . So  $\Omega_0$  plays the role of an effective energy for the quasi-particles from which we can define an effective mass  $m_* = \Omega_0(\mathbf{p} = 0)$ . We will later derive Eq. (2.82) for  $\Omega_0$ , but already note its specialization (with  $F = {}_2F_1$  the hypergeometric function)

$$m_* = mF\left(-\frac{1}{2}, \frac{1}{2}; 1; -\gamma^{-2}\right) = \begin{cases} \frac{2}{\pi}m\gamma^{-1}, & \gamma \ll 1, \\ m, & \gamma \gg 1, \end{cases} \quad (2.60)$$

depending only on the Keldysh parameter  $\gamma$ . Both notably differ from their counterparts without a background field. For example, the effective mass corresponding to the parameters  $E_0 = 0.2E_c$ ,  $\nu = 0.02m$  (the same parameters as in Figs. 2.4–2.6) is  $m_* \approx 6.4m$ . The quasi-particles in a background field are thus much more massive than their free counterparts, requiring more quanta to produce. Not taking into account the increased effective mass, one would guess 100 quanta of this field are needed for one pair at the threshold (the pair then being at rest). But as we can see from the plot, it is actually 650 quanta. A plot of the effective mass over the Keldysh parameter is shown in the right panel of Fig. 2.6. The limits for  $\gamma \ll 1$  and  $\gamma \gg 1$  given in Eq. (2.60) can be easily identified. For a more detailed discussion of the effective mass in the context of pair creation see [95].

We mention one more fact: The peaks for the even numbered shells do not appear in the cut of the phase space along the  $p_\perp$  direction, see the left panel of Fig. 2.5, whereas they do

appear in the  $p_{\parallel}$  direction, see the right panel. This will be explained below in section 2.7 when we study the amplitudes  $I_n$ .

### 2.5.2 Behavior of $f$ close to a shell

Having identified the shell/ridge structures as the important features of the residual phase space distribution in periodic fields, we want to investigate the behavior of the quasi-particle density  $f$  when the momentum  $\mathbf{p}$  is close to a shell. Since the ridges form ellipse-like structures in the  $p_{\perp}$ - $p_{\parallel}$  plane, we introduce polar coordinates:  $p_{\perp} = p \cos \varphi$ ,  $p_{\parallel} = p \sin \varphi$  with  $-\pi/2 \leq \varphi \leq \pi/2$ . These “ellipses” are then parametrized by  $\varphi$ -dependent radii  $p_n(\varphi)$ , where  $n$  is again the shell number. Each term in the sum (2.58) contributes only in a small region around each corresponding shell. We therefore make the following approximations:

1. We drop the terms for which there is no solution to  $2\Omega_0 = n\nu$ , i.e. we only take the sum for  $n \geq n_0 = \left\lceil \frac{2\Omega_0(0)}{\nu} \right\rceil$ .<sup>8</sup>
2. We set  $I_n(\mathbf{p}) = I_n(p, \varphi) = I_n(p_n(\varphi), \varphi)$  that is we replace the value of  $I_n$  close to a shell by its value on the shell.
3. We make a Taylor expansion of  $\Omega_0(\mathbf{p}) = \Omega_0(p, \varphi)$  around  $p = p_n(\varphi)$  to first order:  $\Omega_0(p_n(\varphi) + \epsilon_p, \varphi) = \Omega_0(p_n(\varphi), \varphi) + \Omega'_0(p_n(\varphi), \varphi)\epsilon_p + \mathcal{O}(\epsilon_p^2)$ . The prime is the derivative w.r.t.  $p$ , i.e.  $\Omega'_0 = \frac{\partial}{\partial p}\Omega_0$ .

By definition of  $p_n(\varphi)$ , we have  $2\Omega_0(p_n(\varphi), \varphi) = n\nu$  and therefore  $n\nu - 2\Omega_0(p, \varphi) = -2\Omega'_0(p_n(\varphi), \varphi)\epsilon_p + \mathcal{O}(\epsilon_p^2)$ . Inserting all this into (2.58) (we do not write out the  $\varphi$  dependence of  $p_n$ ,  $I_n$  and  $\Omega'_0$ ) yields

$$I(t, \mathbf{p}) = -i \sum_{n \geq n_0} I_n(p_n) \frac{e^{-2i\Omega'_0(p_n)(p-p_n)t} - 1}{2\Omega'_0(p_n)(p-p_n)}. \quad (2.61)$$

To finally arrive at the pair density  $f$  we take the squared modulus of the above sum:

$$f(t, \mathbf{p}) = \frac{1}{2} |I(t, \mathbf{p})|^2 = \sum_{n \geq n_0} |I_n(p_n)|^2 \frac{\sin^2 [\Omega'_0(p_n)(p-p_n)t]}{[\Omega'_0(p_n)(p-p_n)]^2} + \text{mixed terms}. \quad (2.62)$$

The “mixed terms” all contain periodic factors and, by a heuristic argument, these are proportional to the amplitude  $E_0/\nu$  of  $A$ . This is where the switching-on/off comes into play again: If we switch off slowly enough, the amplitude is reduced in a quasi-static way. This also causes the “mixed terms” to go to zero, so that we have

$$f(t_{\text{off}}, \mathbf{p}) = \frac{1}{2} \sum_{n \geq n_0} |I_n(p_n)|^2 \frac{\sin^2 [\Omega'_0(p_n)(p-p_n)t_{\text{flat}}]}{[\Omega'_0(p_n)(p-p_n)]^2}. \quad (2.63)$$

Note that the time argument on the l.h.s. is  $t_{\text{off}} = t_{\text{flat}} + 2t_{\text{ramp}}$  while on the r.h.s. it is  $t_{\text{flat}}$ . We effectively only used the switching-on/off to make the oscillating mixed terms in (2.62) go to zero. To see how this happens we look at a full numerical solution of Eq. (2.29)

<sup>8</sup>The symbol  $\lceil x \rceil$  denotes the smallest integer greater or equal to  $x$ . For example,  $\lceil 3.4 \rceil = 4$ ,  $\lceil -5.6 \rceil = -5$ ,  $\lceil 6 \rceil = 6$ .

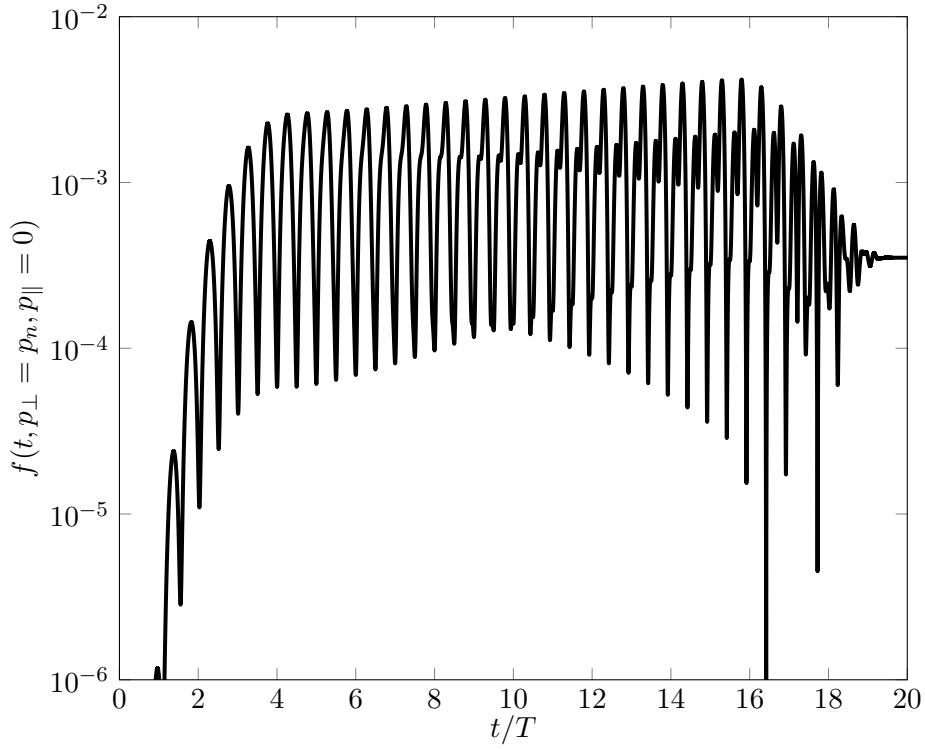


**Figure 2.7:** Plot of the time evolution of  $f$  for certain values of  $p_{\perp}$  and  $p_{\parallel}$  referring to a point on a ridge. Parameters are  $E_0 = 0.2E_c$ ,  $\nu = 0.5m$ ,  $t_{\text{ramp}} = 5T$ ,  $t_{\text{flat}} = 10T$ . We choose our momenta so that we are on a shell for the given parameters, i.e.  $p_{\perp} = 0.6920m$  and  $p_{\parallel} = 0$ . The switching-off sets in at  $t = 15T$  and makes the oscillations go to zero. The residual density remains constant for  $t > 20T$ .

in Fig. 2.7, where the complete time evolution of  $f$  for one point on a ridge is shown. One can see large oscillations at intermediate times, their maxima growing with time, but upon switching off they vanish to leave the residual density behind. This ties in with the remark we made about the necessity for a switching-off that is slow enough, at least over a few oscillations of the underlying field. Imagine we instead suddenly switched off in the middle of the oscillations. We might get any value between about  $5 \times 10^{-5}$  and  $5 \times 10^{-3}$ , depending on where exactly we switched off, which is clearly unphysical and due to the spike in the  $E$  field this sudden switching-off would produce. Careful readers may observe that we did not use our usual frequency  $\nu = 0.02m$  and flat-top time  $t_{\text{flat}} = 50T$  for this plot, but instead  $\nu = 0.5m$  and  $t_{\text{flat}} = 10T$ . Otherwise the oscillations would have been too large and rapid to be depicted in a meaningful way.

The switching-on/off process is investigated more thoroughly in [85]. It shows the above results more rigorously, gives error estimates and also looks at other possible functions to modulate the oscillations with (like a Gaussian or super-Gaussian).

The resulting phase space distribution  $f$  from Eq. (2.63) seems to oscillate over the entire phase space for variations of  $t_{\text{flat}}$ . But when we take a closer look at one summand we see that

$$\frac{\sin^2 [\Omega'_0(p_n)(p - p_n)t_{\text{flat}}]}{[\Omega'_0(p_n)(p - p_n)]^2} = t_{\text{flat}}^2 \frac{\sin^2 [\Omega'_0(p_n)(p - p_n)t_{\text{flat}}]}{[\Omega'_0(p_n)(p - p_n)t_{\text{flat}}]^2} \xrightarrow{p \rightarrow p_n} t_{\text{flat}}^2 \quad (2.64)$$

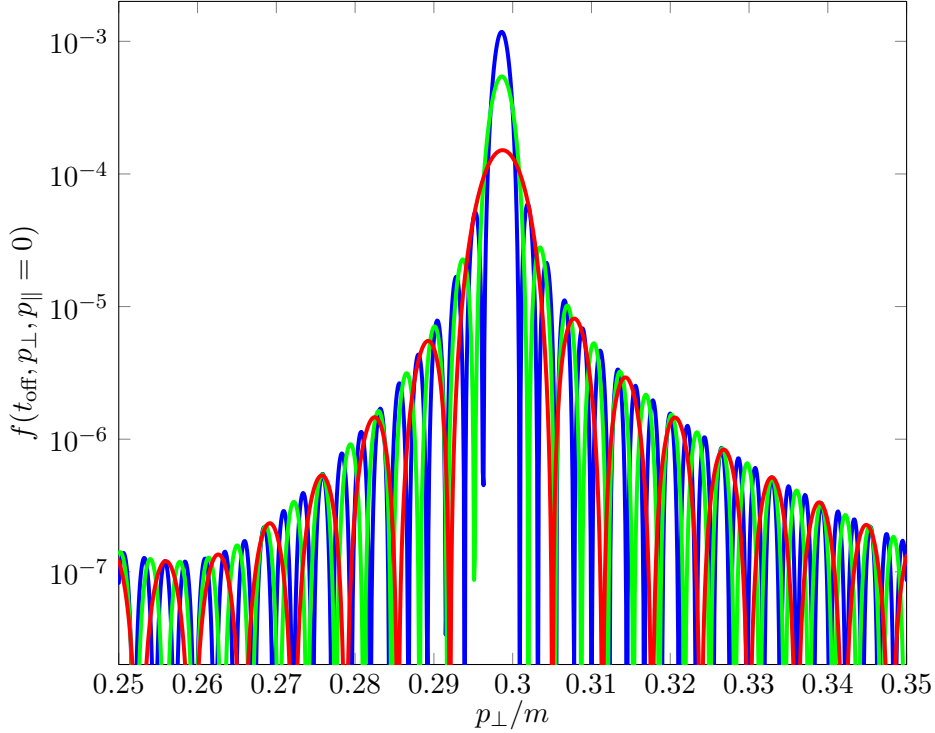


**Figure 2.8:** A zoom into the region of the  $n = 651$  peak in the left panel of Fig. 2.5. Red:  $t_{\text{flat}} = 20T$ ; green:  $t_{\text{flat}} = 40T$ ; blue:  $t_{\text{flat}} = 60T$ .

because  $\lim_{x \rightarrow 0} \sin x/x = 1$ . So the peak of a shell increases  $\propto t_{\text{flat}}^2$ , while its width decreases  $\propto 1/t_{\text{flat}}$ . One can see both claimed time dependencies in Fig. 2.8. Exactly on a shell for a fixed value of  $n$  we get (writing out the  $\varphi$  dependence)

$$f(t_{\text{off}}, p_n(\varphi), \varphi) = \frac{1}{2} |I_n(p_n(\varphi), \varphi)|^2 t_{\text{flat}}^2 + \text{const}, \quad (2.65)$$

where “const” here means “independent of  $t_{\text{flat}}$ ”.

Our two main results of this section can be summarized as follows.

1. Close to a shell the momentum dependence of the residual density is  $f(t_{\text{off}}, \mathbf{p}) \propto \sin^2[b(p - p_n)]/[b(p - p_n)]^2$ .
2. The peak of the shell grows  $\propto t_{\text{flat}}^2$ , while its width shrinks  $\propto 1/t_{\text{flat}}$ .

Since some unsystematic approximations were made in the derivation of Eq. (2.63) on top of already employing the LDA, we need to compare the result carefully to the numerical simulation. We cannot yet compare the exact formulas with the numerics, because we lack a way of calculating  $I_n(p_n)$  (this will be the subject of the next section), but their summarized form can be. The  $t_{\text{flat}}^2$  dependence should appear as a straight line in a log-log plot of  $f$  over  $t_{\text{flat}}$ , and that is exactly what we see in the left panel of Fig. 2.9 for  $t_{\text{flat}} \gtrsim 10T$ . The curve deviates from a straight line for smaller values of  $t_{\text{flat}}$ , but that is to be expected, since some of our approximations are not valid for this parameter region and the contributions from the switching-on/off process will dominate when  $t_{\text{ramp}} \gg t_{\text{flat}}$ . In that regime, a quasi-static approximation can be made which effectively enlarges the  $t_{\text{flat}}$ -region and which can also be applied to Gaussian-type pulses [85].



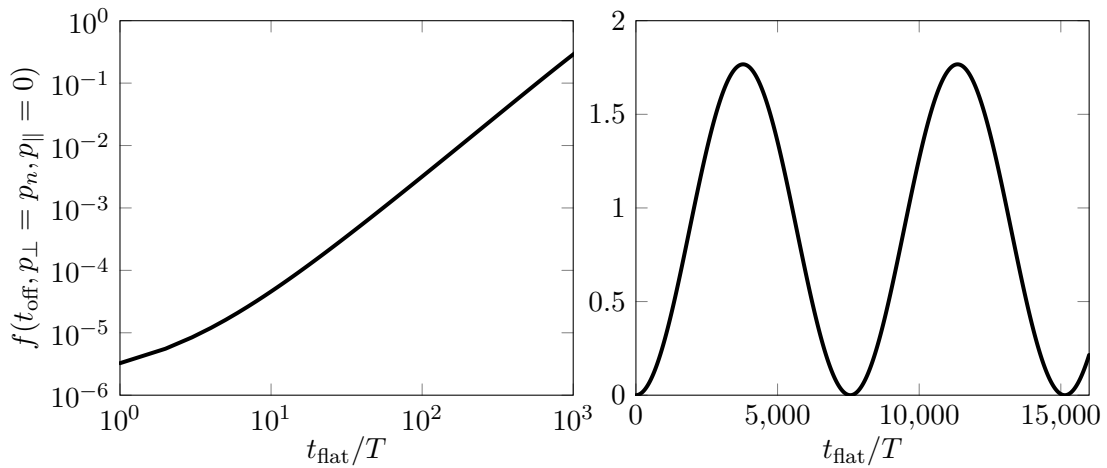


**Figure 2.9:** Plot of the  $t_{\text{flat}}$  dependence of  $f(t_{\text{off}})$ . Parameters are  $E_0 = 0.2E_c$ ,  $\nu = 0.02m$ ,  $t_{\text{ramp}} = 5T$ . We choose our momenta so that we are on the  $n = 651$  shell in the left panel of Fig. 2.5, i.e.  $p_{\perp} = 0.2985933m$  and  $p_{\parallel} = 0$ . Left:  $1 < t_{\text{flat}}/T < 10^3$ , log-log scales; right:  $0 < t_{\text{flat}}/T < 16000$ , linear scales.

For completeness' sake we also show the long term time evolution of  $f$  in the right panel of Fig. 2.9. The apparent functional form of the density is  $f = a \sin^2(bt_{\text{flat}})$  for some parameters  $a$  and  $b$ . Informally it is clear the unlimited growth implied in the  $t_{\text{flat}}^2$  dependence will be curbed by the Pauli-blocking factor  $1 - f$  in the QKE (2.29) (whose effect is better understood in its integro-differential form (2.30) and which arises from the fermion statistics). It is less obvious, why the density should not saturate at some level, but instead decline again to zero. For an explanation and derivation of this we refer to appendix B.3. The  $t_{\text{flat}}^2$  behavior is only valid for  $f \ll 1$  so that the LDA can be applied, and is also the first term of the Taylor expansion of the  $\sin^2$  function. From this and Eq. (2.65) we can conclude  $ab^2 = |I_n|^2/2$ , so our approximation gives a constraint on the parameters of the full solution, but cannot determine them completely. This oscillating long term behavior is reminiscent of Rabi oscillations in (fermionic) two-level systems and was investigated in more detail in [96, 97]. It is, however, probably not relevant for experimental observations, since it would require unrealistically large laser intensities and pulse durations before it would set in.

We conclude that the time dependence of the full solution is well captured by our approximation. We can similarly compare the momentum dependence, as is shown in Fig. 2.10. We plot the full solution that was already shown in Fig. 2.5, but zoom into the region of the  $n = 651$  peak. Overlaid over this black curve is a fit of the numerical data to our derived shape  $a \frac{\sin^2[b(p-p_n)]}{[b(p-p_n)]^2}$  with variable parameters  $a$ ,  $b$  and  $p_n$ . The data and our predicted curve agree well close to the shell and deviate farther out. But keep in mind this is a log plot: The smaller peaks to the sides do not contribute much to the overall density, the deviations there are thus not as important as the agreement at the main peak. The relative error between the integrals over each curve, restricted to the  $p_{\perp}$  range in this window, is just 0.5%

Both the comparison of the time evolution in Fig. 2.9 and the momentum dependence in Fig. 2.10 validate our analytical derivation and the (sometimes non-systematic) approximations that were made.

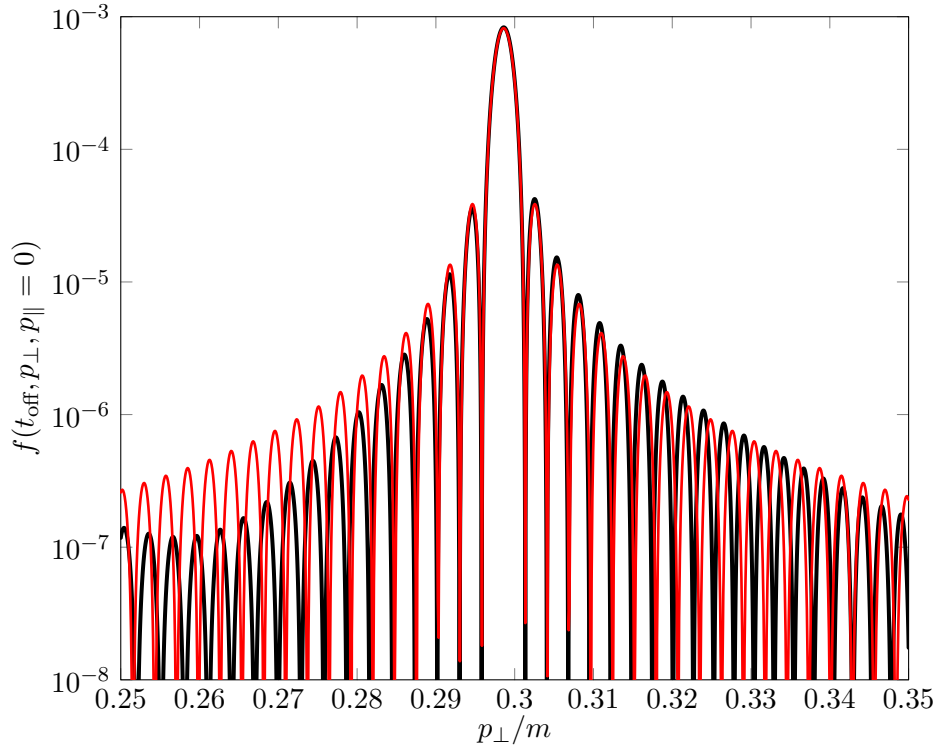


**Figure 2.10:** A zoom into the  $n = 651$  peak region in the left panel of Fig. 2.5 (black curve). In red is a fit of  $a \sin^2[b(p - p_n)]/[b(p - p_n)]^2$  to this data,  $a = 8.312 \times 10^{-4}$ ,  $b = 1.135 \times 10^3/m$  and  $p_n = 0.2986m$ .

### 2.5.3 Total pair number

From Eq. (2.63) it is straightforward to derive a formula for the total pair number  $n$  which is defined as

$$\begin{aligned} n(t_{\text{off}}) &= \int \frac{d^3p}{(2\pi)^3} f(t_{\text{off}}, \mathbf{p}) = \int \frac{dp_{\parallel} dp_{\perp}}{(2\pi)^2} p_{\perp} f(t_{\text{off}}, p_{\perp}, p_{\parallel}) \\ &= \int \frac{d\varphi dp}{(2\pi)^2} p^2 \cos \varphi f(t_{\text{off}}, p, \varphi). \end{aligned} \quad (2.66)$$

We cannot naively multiply the phase space factor  $p^2$  onto the  $f$  given in (2.63), because each term in the sum was derived under the assumption that  $p$  is close to  $p_n$ . The factor would blow up this error and make the integral not converge. Instead, we replace  $p^2 \rightarrow p_n^2$  in each summand to get

$$\begin{aligned} n(t_{\text{off}}) &= \frac{1}{2} \int \frac{d\varphi dp}{(2\pi)^2} \sum_{n \geq n_0} p_n^2 \cos \varphi |I_n(p_n)|^2 \frac{\sin^2 [\Omega'_0(p_n)(p - p_n)t_{\text{flat}}]}{[\Omega'_0(p_n)(p - p_n)]^2} \\ &= \frac{\pi}{2} t_{\text{flat}} \sum_{n \geq n_0} \int \frac{d\varphi}{(2\pi)^2} \cos \varphi \frac{p_n(\varphi)^2 |I_n(p_n(\varphi), \varphi)|^2}{\Omega'_0(p_n(\varphi), \varphi)}. \end{aligned} \quad (2.67)$$

We again inserted the  $\varphi$  dependence after the second equality sign to make it explicit. This formula has a nice interpretation: We can calculate the total number of produced pairs by integrating over a single shell and then summing over all shells. The integrand for each shell is made up out of its amplitude  $|I|^2$ , its width  $\Omega'_0$  and the phase space factor  $p_n^2$ . It is



interesting to note that, while the peak of each ridge grows  $\propto t_{\text{flat}}^2$ , the total pair number  $n$  only grows  $\propto t_{\text{flat}}$ . This is because the width of each ridge is proportional to  $1/t_{\text{flat}}$ .

## 2.6 Calculating the amplitudes $I_n$

In the preceding section, we derived an approximation for  $f$  which depends on two quantities: the amplitudes  $I_n$  and the derivative of the effective energy  $\Omega'_0$ , both evaluated on a shell. While  $\Omega_0$  is given by a simple integral, which cannot be simplified much further,  $I_n$  is more complicated. For its evaluation we will proceed as follows: We exploit the periodicity of the integrand in (2.57) to deform the integration contour into the complex  $t$ -plane. When the contour passes close to a singularity of the integrand, we can employ the method of steepest descent to calculate the integral. The residue theorem alone is not applicable because our integrand has branch cuts emerging from the poles of the integrand.

A similar analysis was done in [98]. Complex integration with critical poles and branch cuts appears generically in the context of pair production, it is not dependent on the approach via the quantum kinetic equation. For example, similar techniques are also employed when studying worldline instantons [61–63] or when using WKB-type approximations [59, 60]. This confirms the importance of the zeros of  $\Omega$  (which are the poles of the integrand) in the generic setting. In chapter 3, we will see that one can give the dynamically assisted Schwinger effect a nice interpretation in terms of how the second field influences the location of said zeros.

### 2.6.1 Singularity and integration contour

We will once again leave the  $\varphi$  dependence implicit. On a shell, Eq. (2.57) reduces to<sup>9</sup>

$$I_n(p_n) = \frac{1}{T} \int_{-T/2}^{T/2} dt \frac{eE(t)\epsilon_{\perp}}{\Omega(t, p_n)^2} e^{2i\Theta(t, p_n)}. \quad (2.68)$$

The integrand will have a singularity when  $\Omega^2 = 0$ . This is indeed the case for four points  $t_i$  in the strip  $-\frac{T}{2} \leq \text{Re}(t_i) \leq \frac{T}{2}$ , namely in counter clockwise order  $t_0$ ,  $-t_0^*$ ,  $-t_0$  and  $t_0^*$  with

$$t_0 = \frac{1}{\nu} \arccos \left[ \frac{\nu}{E_0} (p_{\parallel} + i\epsilon_{\perp}) \right], \quad \arccos z = \frac{\pi}{2} + i \ln \left( iz + \sqrt{1 - z^2} \right). \quad (2.69)$$

This looks like a case for the residue theorem, but unfortunately one fact prevents its use:  $\Omega$ , being the square root of  $\Omega^2$  has a branch cut emerging from each  $t_i$ , extending to infinity. This prevents us from closing a contour around any  $t_i$ . We will instead choose the contour depicted in Fig. 2.11 together with the zeros and branch cuts mentioned above. Our original integration path was on the real axis from  $-T/2$  to  $T/2$ , labeled  $\Gamma_1$  in the

<sup>9</sup>We also shift the integration interval by  $-T/2$  to make the equations more symmetric. The integrand is  $T$ -periodic, which makes this shift valid. If it were evaluated off a shell, it would not necessarily be periodic, because then  $2\Omega_0 \neq n\nu$  for integer  $n$ , which makes  $\Theta$  non-periodic and thus the entire integrand.

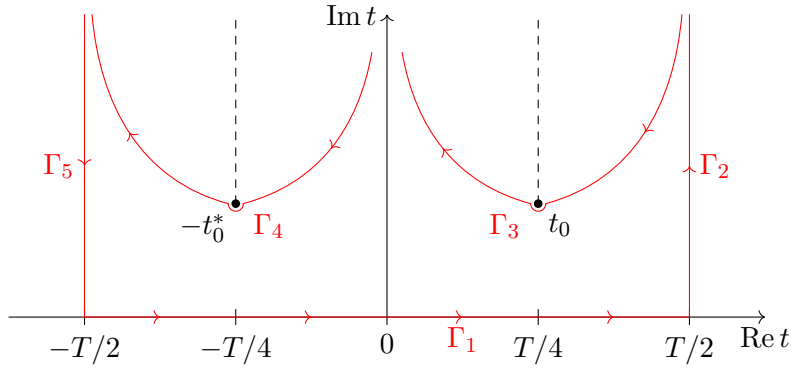


**Figure 2.11:** Schematic plot of the upper complex  $t$ -plane, showing two of the zeros of  $\Omega^2$  (dots labeled by  $t_0$  and  $-t_0^*$ ), the branch cuts emerging from them (dashed lines) and the integration contour chosen (red line, direction marked by arrows, partial contour paths labeled with  $\Gamma_i$ ).

figure. We form a closed contour by first following  $\Gamma_2$  to infinity, coming back along  $\Gamma_3$  to swing around  $t_0$  so that the pole lies *outside* the contour and head off to infinity again. We mirror this to the left to close the contour. The integrand is holomorphic within the region enclosed by this contour, since the only poles lie outside it. Since the integrand is periodic, the contributions from  $\Gamma_2$  and  $\Gamma_5$  cancel leaving us with (symbolically)  $\int_{\Gamma_1} = -\int_{\Gamma_3} - \int_{\Gamma_4}$ .

The shape of  $\Gamma_3$  and  $\Gamma_4$  is arbitrary, as long as their endpoints are fixed and they do not cross the branch cuts. The method of steepest descent that we will employ is based on the following observation: The real part of  $\Omega$  is always greater than zero, since it is a square root (and we follow the standard convention of placing the branch cut of the square root along the negative real axis). Therefore  $\text{Im } \Theta \rightarrow +\infty$  as  $\text{Im } t \rightarrow +\infty$  and the factor  $e^{2i\Theta}$  rapidly goes to zero. On the other hand,  $\Theta$  is stationary around  $t_0$  via the latter's definition:  $\Omega(t_0)^2 = 0 \implies \Omega(t_0) = \dot{\Theta}(t_0) = 0$ . We therefore choose a path infinitesimally close to  $t_0$  (symbolized by the cusp of  $\Gamma_3$  around  $t_0$  in Fig. 2.11) and following which  $\text{Im } \Theta$  grows the fastest moving away from  $t_0$ . This is the path of steepest descent.

We do, however, not need to derive a parametrization for the path because, again, the precise form of  $\Gamma_3$  and  $\Gamma_4$  is irrelevant: deforming them does not change the value of the integral along them, due to Cauchy's theorem. The above discussion is merely about making our next steps plausible.

### 2.6.2 Expanding the integrand and closing the contour

Since it is established that contributions to the integral along  $\Gamma_3$  and  $\Gamma_4$  are concentrated next to the poles  $t_0$  and  $-t_0^*$ , we expand the integrand around both points. But we must be careful to preserve the asymptotic behavior of  $\Theta$  as  $\text{Im } t \rightarrow +\infty$ . Otherwise we would add contributions far away from the poles, rendering the expansion invalid for approximating the integral.

Expanding  $Q$  is straightforward:  $\Omega(t)^2 = 2i\epsilon_\perp eE(t_0)(t - t_0) + \mathcal{O}((t - t_0)^2)$ , therefore

$$Q(t) = \frac{eE(t)\epsilon_\perp}{\Omega(t)^2} = \frac{1}{2i(t - t_0)} + \mathcal{O}((t - t_0)^0). \quad (2.70)$$

For the exponent we use<sup>10</sup>

$$\begin{aligned} \Theta(t) &= \int_0^t dt' \Omega(t') = \int_0^{t_0} dt' \Omega(t') + \int_{t_0}^t dt' \Omega(t') \\ &= \Theta(t_0) + \int_{t_0}^t dt' \sqrt{2i\epsilon_\perp eE(t_0)(t' - t_0)} + \mathcal{O}((t - t_0)^{5/2}) \\ &= \Theta(t_0) + \frac{2}{3} \frac{[2i\epsilon_\perp eE(t_0)(t - t_0)]^{3/2}}{2i\epsilon_\perp eE(t_0)} + \mathcal{O}((t - t_0)^{5/2}). \end{aligned} \quad (2.71)$$

We cannot combine the common factor  $2i\epsilon_\perp eE(t_0)$  into one expression since for complex numbers  $z_1$  and  $z_2$  in general  $\sqrt{z_1 z_2} \neq \sqrt{z_1} \sqrt{z_2}$  and we also cannot make a simple Taylor expansion for  $\Theta$  around  $t_0$ , both of which is obstructed by the branch cut of the square root function.

Let us define two shorthands:  $J$  for the part of our integral along  $\Gamma_3$  with the integrand expanded around  $t_0$  and  $z = 2i\epsilon_\perp eE(t_0)$  to get from Eq. (2.68)

$$J = \frac{1}{T} \int_{\Gamma_3} dt \frac{e^{2i\Theta(t_0)} \exp\left(\frac{4}{3}i[z(t - t_0)]^{3/2}/z\right)}{2i(t - t_0)} = \frac{e^{2i\Theta(t_0)}}{2iT} \int_{\tilde{\Gamma}_3} dx \frac{\exp\left(\frac{4i}{3z}x^{3/2}\right)}{x}. \quad (2.72)$$

The second equality sign follows from the substitution  $x = z(t - t_0)$ . The pole in the  $x$ -plane (where also the branch cut emerges) is at  $x = 0$ . There are two lines emerging from zero on which the exponent is strictly negative and goes to  $-\infty$ .<sup>11</sup> We choose the integration path  $\tilde{\Gamma}_3$  to follow these lines and swing around the pole similar to  $\Gamma_3$  in the  $t$ -plane. It is depicted schematically in the left panel of Fig. 2.12. Knowing this we make another substitution,  $y = \frac{4i}{3z}x^{3/2}$ . This closes the contour because both endpoints are mapped to  $-\infty$  and removes the branch cut, while the pole stays, as one can see in the right panel of Fig. 2.12. The final closed path is traversed in clockwise order, which accounts for a  $-1$  below. With the integral so transformed, we can finally use the residue theorem to evaluate  $J$ :

$$J = \frac{e^{2i\Theta(t_0)}}{2iT} \oint dy \frac{2}{3} \frac{e^y}{y} = -\frac{2\pi e^{2i\Theta(t_0)}}{3T}. \quad (2.73)$$

This procedure can be done the same way for  $\Gamma_4$  around the pole  $-t_0^*$ : the result is just  $-J^*$ . Adding both contributions we get

$$I_n(p_n) = -J + J^* = \frac{4\pi i}{3T} \text{Im} e^{2i\Theta(t_0)}. \quad (2.74)$$

<sup>10</sup>Such an expansion in fractional powers of the expansion parameter is called a Puiseux series.

<sup>11</sup>Showing this requires some care and rests upon the fact that  $\text{Re}(E(t_0)) > 0$ .

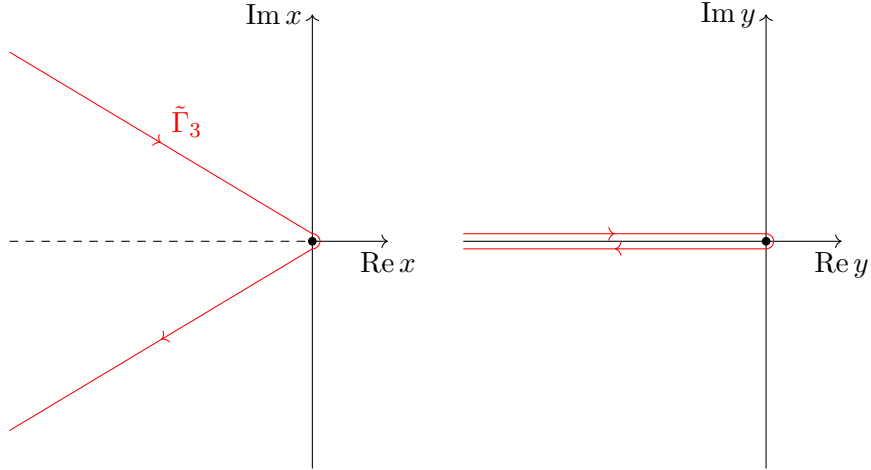


**Figure 2.12:** Schematic plot of the integration contours in the  $x$  and  $y$ -planes defined by the substitutions in the text.

## 2.7 Physics from the amplitudes

Equation (2.74) is remarkably simple: Find the shell momentum  $p_n$  from Eq. (2.59) for given values  $n$  and  $\varphi$ , from that compute  $t_0$  and then  $\Theta$  at that location. Insert it into (2.74) to get  $I_n$  which serves as the main input for all the analytical properties derived in section 2.5. We thus have to evaluate a simple integral in the complex plane, which is considerably simpler than solving the full quantum kinetic equations. This integral is also much simpler than the low density approximation. The quantity  $\Theta(t_0)$  lends itself well as a simple handle on the properties of the pair density  $f$  in phase and parameter space. We need to get a feeling for the former in order to understand the latter.

To do this, we will evaluate  $\Theta(t_0)$  in the special case  $p_{\parallel} = 0$  which is equivalent to  $\varphi = 0$ . This is sensible as it contains all the relevant physics, as will become clear later on. First, we specialize the location of the root from Eq. (2.69) to this case:

$$t_0 = \frac{T}{4} + \frac{iT}{2\pi} \operatorname{arsinh} \left( \frac{\nu \epsilon_{\perp}}{E_0} \right). \quad (2.75)$$

The perpendicular energy  $\epsilon_{\perp}$  now depends on the chosen shell number  $n$ , but we will leave that implicit. Any path in the complex  $t$  plane from 0 to  $t_0$  is equally good for computing the integral, provided it does not cross the branch cut. We will go from 0 to  $\operatorname{Re} t_0$  and  $\operatorname{Re} t_0$  to  $t_0$ . This yields

$$\Theta(t_0) = \left( \int_0^{T/4} dt + \int_{T/4}^{t_0} dt \right) \sqrt{\epsilon_{\perp}^2 + \frac{e^2 E_0^2}{\nu^2} \cos^2(\nu t)}. \quad (2.76)$$

Because we set  $p_{\parallel} = 0$  we get the simple  $\cos^2$  term under the root. Since  $\cos^2$  is  $T/2$ -periodic, the first integral (which is just  $\Theta(T/4)$ ) is in fact  $\Theta(T)/4$ . But since we are on a shell we also have  $\Theta(T) = T \cdot \Omega_0 = n\pi$ . For the second integral we use the shorthand  $\delta = \nu \epsilon_{\perp} / eE_0$ , which is just the Keldysh parameter scaled by  $\epsilon_{\perp} / m$ ,  $\delta = \gamma \sqrt{1 + p_{\perp}^2 / m^2}$ .

Now, we reparametrize the path and use some trigonometric identities to get

$$\begin{aligned}\Theta(t_0) &= \frac{n\pi}{4} + i\frac{\epsilon_\perp}{\nu} \int_0^{\operatorname{arsinh} \delta} dx \sqrt{1 - \frac{1}{\delta^2} \sinh^2 x} \\ &= \frac{n\pi}{4} + i\frac{\epsilon_\perp}{\nu} \delta \int_0^1 dx \sqrt{\frac{1-x^2}{1+\delta^2 x^2}}.\end{aligned}\tag{2.77}$$

We refactor the  $\delta \int dx \dots$  term into a function  $g(\delta)$ . It cannot be expressed in terms of elementary functions, but with the help of the hypergeometric function  $F = {}_2F_1$ , which has the integral representation

$$F(a, b; c; z) = \frac{\Gamma(c)}{\Gamma(b)\Gamma(c-b)} \int_0^1 dt \frac{t^{b-1}(1-t)^{c-b-1}}{(1-zt)^a}\tag{2.78}$$

for  $\operatorname{Re} c > \operatorname{Re} b > 0$ . With this

$$g(\delta) = \frac{\pi}{4} \delta F\left(\frac{1}{2}, \frac{1}{2}; 2; -\delta^2\right).\tag{2.79}$$

This function was introduced in [98] with a slightly different notation. Note that the assumptions made in [98] to integrate over phase space, namely that the frequency  $\nu$  be so low that the peaks are quasi-continuous, are not satisfied in our case, see also [99]. For the dynamic phase at the pole, we get

$$\Theta(t_0) = \frac{n\pi}{4} + i\frac{\epsilon_\perp}{\nu} g\left(\frac{\nu\epsilon_\perp}{eE_0}\right).\tag{2.80}$$

Inserting this into Eq. (2.74) gives

$$I_n = \frac{4\pi i}{3T} \sin\left(\frac{n\pi}{2}\right) \exp\left[-2\frac{\epsilon_\perp}{\nu} g\left(\frac{\nu\epsilon_\perp}{eE_0}\right)\right].\tag{2.81}$$

This formula is consistent with an observation we made earlier. Recall that in the left panel of Fig. 2.5 the peaks of the even shells do not appear. This is easy to understand from Eq. (2.81). For even  $n$ ,  $\sin(n\pi/2) = 0$  so  $I_n = 0$ . Technically, there is a shell and a peak at this location, but it has no amplitude and thus does not show up in the plot. In fact, on a shell  $I_n(p_n(\varphi), \varphi)$  has  $n+1$  roots, which must be symmetrical around  $\varphi = 0$ . Clearly for even  $n$  this implies a root at  $\varphi = 0$ .

Two similar formulas specializing the Fourier zero mode  $\Omega_0$  from Eq. (2.54) and its derivative  $\Omega'_0$  to  $p_\parallel = 0$  can be derived using analogous steps as above and also employing the hypergeometric function  $F$ . We only note the result:

$$\begin{aligned}\Omega_0(p_\perp, p_\parallel = 0) &= \epsilon_\perp F\left(-\frac{1}{2}, \frac{1}{2}; 1; -\delta^{-2}\right), \\ \Omega'_0(p_\perp, p_\parallel = 0) &= \frac{p_\perp}{\epsilon_\perp} F\left(\frac{1}{2}, \frac{1}{2}; 1; -\delta^{-2}\right),\end{aligned}\tag{2.82}$$

with the same  $\delta$  as above.<sup>12</sup>

<sup>12</sup>It is not quite obvious that the straightforward derivative of the first line in Eq. (2.82) should yield the second line. Showing this requires the use of some addition theorems for the hypergeometric function, or the integral representation (2.78).

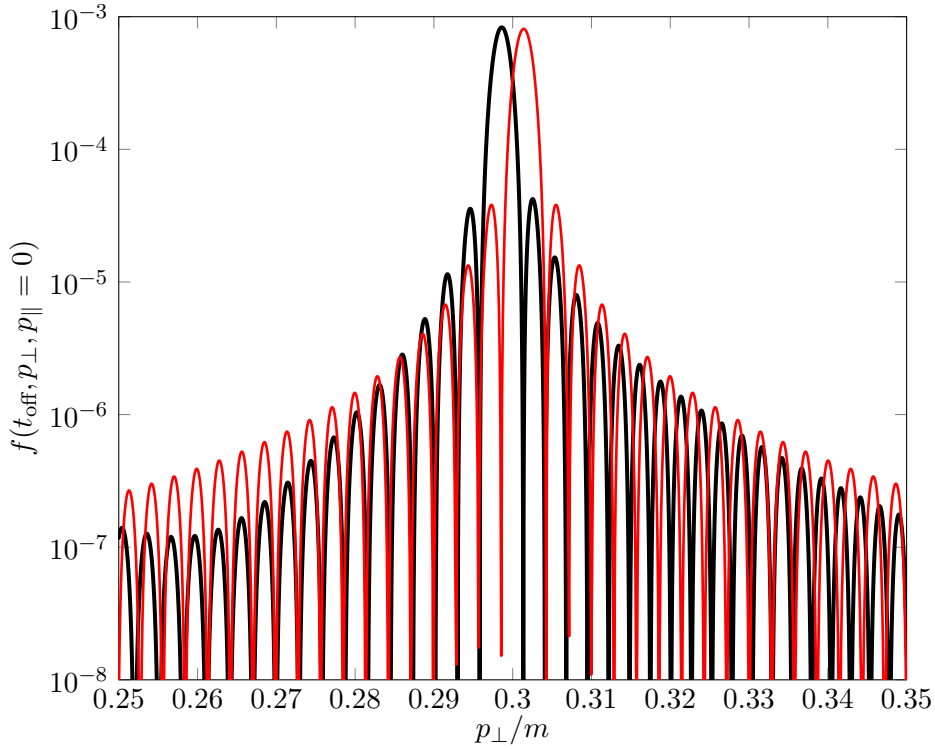


**Figure 2.13:** A zoom into the  $n = 651$  peak region in the left panel of Fig. 2.5 (black curve). See also Fig. 2.10. In red is a the analytically derived shell shape  $a \sin^2[b(p - p_n)]/[b(p - p_n)]^2$  with  $a = 8.121 \times 10^{-4}$ ,  $b = 1.097 \times 10^3/m$  and  $p_n = 0.3014m$ .

We finally have all the ingredients ready to compare the analytics with the numerics. As a comparison we will again use a zoom into the shell number  $n = 651$  region, as in Fig. 2.10, since there one can easily compare the three key characteristics we derived: shell position, peak height and shell shape. Let us note again the parameters used in this example:  $E_0 = 0.2E_c$ ,  $\nu = 0.02m$ ,  $t_{\text{ramp}} = 5T$ ,  $t_{\text{flat}} = 50T$ .

First we determine the position. The shell defining equation  $2\Omega_0(p_n, 0) = 651\nu$  must be solved numerically with  $\Omega_0$  given by Eq. (2.82). We get  $p_n = 0.3014m$ . With this we can calculate the derivative, again from Eq. (2.82), as  $\Omega'_0(p_n, 0) = 6.981 \times 10^{-2}$ . The amplitude is computed from Eq. (2.81) as  $I_n = -8.060 \times 10^{-4}i/T$ . The function to be compared to the numerics is then  $a \sin^2[b(p - p_n)]/[b(p - p_n)]^2$  (from (2.63)) with  $a = \frac{1}{2}|I_n|^2 t_{\text{flat}}^2 = 8.121 \times 10^{-4}$  and  $b = \Omega'_0(p_n, 0)t_{\text{flat}} = 1.097 \times 10^3/m$ . The result can be seen in Fig. 2.13. The biggest difference is between the peak positions, which is about  $0.0028m$  for a relative error of 0.9%. This error is actually introduced in the very first approximation we make, going from the full quantum kinetic equation (2.29) to the low-density approximation (2.31). This was verified by solving the LDA numerically, so that we need not rely on the Fourier analysis that led to the shell defining equation  $2\Omega_0 = n\nu$ . Otherwise we see an excellent agreement between theory and numerics. The peak height is off by just 2.3%,<sup>13</sup> and the derived  $\sin^2 x/x^2$  shell shape fits well close to the peak. The relative error between the integrals of both curves is 1.6%, slightly higher than the 0.5% of the fit in Fig. 2.10.

<sup>13</sup>If we manually correct the peak location in (2.81), the error is just 0.3%.

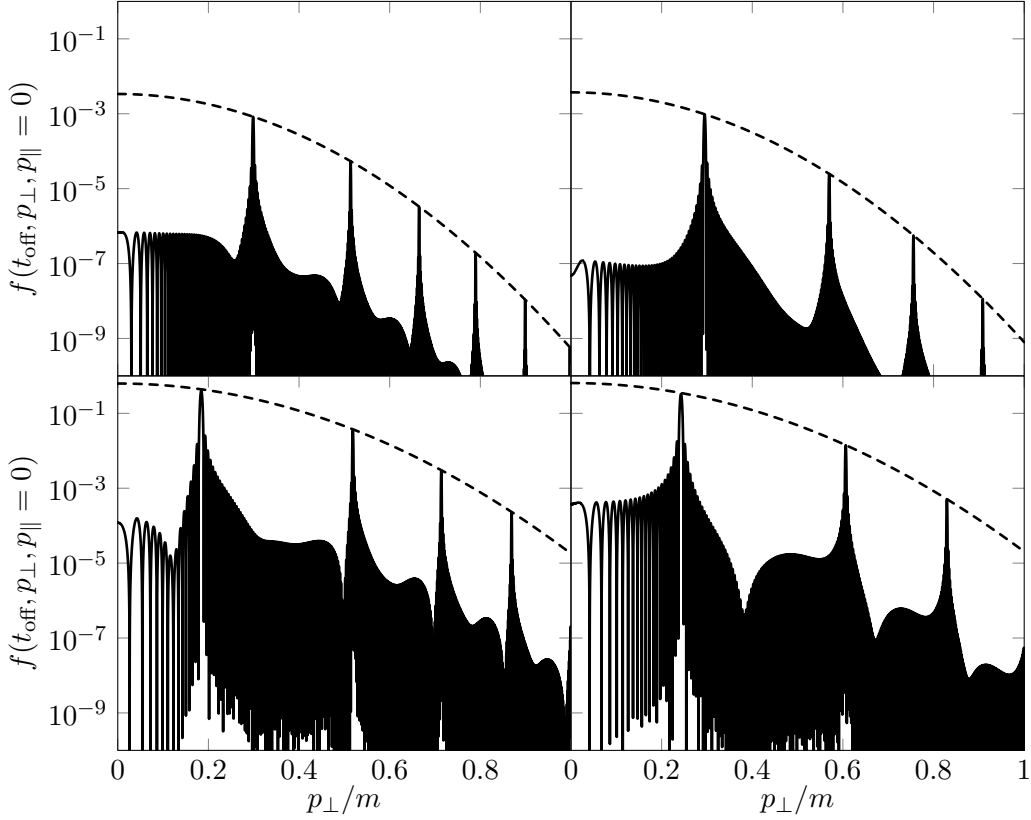


**Figure 2.14:** Comparison of the pair density  $f$  as a function of  $p_{\perp}$  at  $p_{\parallel} = 0$  with the envelope  $\mathcal{E}(p_{\perp})$  from Eq. (2.83) (dashed curve). Parameters are  $E_0 = 0.2E_c$ ,  $\nu = 0.02m$  (top left);  $E_0 = 0.2E_c$ ,  $\nu = 0.05m$  (top right);  $E_0 = 0.3E_c$ ,  $\nu = 0.02m$  (bottom left);  $E_0 = 0.3E_c$ ,  $\nu = 0.05m$  (bottom right). For all panels  $t_{\text{ramp}} = 5T$ ,  $t_{\text{flat}} = 50T$ . The top left panel uses the same parameters as the left panel of Fig. 2.5.

In Eq. (2.81),  $I_n$  is *not* a function of  $p_{\perp}$ , since it was derived under the assumption that the shell defining equation  $2\Omega_0(p_n(\varphi), \varphi) = n\nu$  holds. Because we set  $p_{\parallel} = 0$  this constrains  $p_{\perp}$  to the fixed value  $p_{\perp} = p_n(\varphi = 0)$ . The exponential part of  $I_n$  can, however, be treated as if  $p_{\perp}$  were variable and since by Eq. (2.65) the peak height of a shell is just  $\frac{1}{2}|I_n|^2 t_{\text{flat}}^2$ , we can define an envelope in phase space by

$$\mathcal{E}(p_{\perp}) = \frac{8\pi^2}{9T^2} \exp \left[ -4 \frac{\epsilon_{\perp}}{\nu} g \left( \frac{\nu \epsilon_{\perp}}{eE_0} \right) \right] t_{\text{flat}}^2. \quad (2.83)$$

We compare this envelope with the numerics in Fig. 2.14. The envelope fits the peaks very nicely for a number of different parameters. That together with the comparison of the ridge shape in Fig. 2.13 confirms the string of approximations we employed: We have accurate estimates for peak location, height, width and shape. It also enables us to take a more concise look at the parameter dependence: The phase space structure of  $f$  is quite involved and the peak heights (and total particle number  $n$ ) vary over many orders of magnitude with changing  $E_0$  and  $\nu$ . When we want to focus on that dependence, it is essential to mask out the “noise” of the phase space intricacies. Since the envelope bounds  $f$  from above and is monotonously decreasing,  $\mathcal{E}(p_{\perp} = 0)$  is a good rough measure for  $\max_{\mathbf{p}} f(t_{\text{off}}, \mathbf{p})$  for the purpose of order-of-magnitude estimation.

The important part of  $\mathcal{E}(0)$  is the exponent, which can be written using the Keldysh

parameter  $\gamma = \frac{E_c}{E_0} \frac{\nu}{m}$  as  $-4\frac{m}{\nu}g(\gamma)$ . For  $\gamma \ll 1$  we are in the adiabatic regime and for  $\gamma \gg 1$  in the multiphoton regime. This should be reflected in  $\mathcal{E}(0)$ . The leading order terms of  $g$  for small and large  $\gamma$  are  $g(\gamma) = \frac{\pi}{4}\gamma + \mathcal{O}(\gamma^3)$  and  $g(\gamma) = \ln \gamma + 2 \ln 2 - 1 + \mathcal{O}(1/\gamma^2)$ . Thus the  $E_0$  and  $\nu$  dependence of the exponent and  $\mathcal{E}(0)$  is

$$4\frac{m}{\nu}g(\gamma) \approx \pi \frac{E_c}{E_0}, \quad \mathcal{E}(0) \propto e^{-\pi \frac{E_c}{E_0}} \quad \text{for } \gamma \ll 1, \quad (2.84)$$

$$4\frac{m}{\nu}g(\gamma) \approx 4\frac{m}{\nu} \left( \ln \frac{E_c}{E_0} + \ln \frac{\nu}{m} + 2 \ln 2 - 1 \right), \quad \mathcal{E}(0) \propto \left( \frac{E_0}{E_c} \right)^{4\frac{m}{\nu}} \quad \text{for } \gamma \gg 1. \quad (2.85)$$

The first limit is the exponential behavior typical of the Schwinger effect, which is non-perturbative in  $e$  or  $E_0$ , respectively. In particular, the prefactor  $\pi$  of the exponent is correct. For the second limit, let us recall the Breit-Wheeler effect: In the simplest case, two photons of frequency  $\omega$  collide to create an  $e^+e^-$ -pair. In general, multiple photons may take a part in the collision. These two colliding photons correspond to one quantum of our homogeneous field with frequency  $\nu = 2\omega$ . Therefore, for the Breit-Wheeler effect at the pair-production threshold, where  $\omega = m$ , we have  $\nu = 2m$  and  $\mathcal{E}(0) \propto E_0^2$ . That is the same dependence that can be calculated for this effect perturbatively using Feynman diagrams. We see that the dynamical Schwinger effect interpolates smoothly between these two regimes and non-perturbative and perturbative behavior. It also reproduces correctly the behavior of the special cases in these parameter regions, the Schwinger and Breit-Wheeler effects. This separation of regimes by the Keldysh parameter also confirms our intuition that we laid out below Eq. (2.42).

The dependence of the envelope  $\mathcal{E}(0)$  on the parameters can be seen in Fig. 2.15. It shows a contour plot of the negative of the exponential part of  $\mathcal{E}(0)$ , i.e.  $4\frac{m}{\nu}g(\frac{\nu m}{eE_0})$ . The parameter space is sometimes also called the ‘‘landscape of pair creation’’; for a more detailed discussion, see [100]. There are lines of constant Keldysh parameter depicted as long dashed lines, in particular for  $\gamma = 1$ , to ease distinguishing the regions of different regimes. The contour lines of the exponent are parallel to the  $\nu$ -axis and evenly spaced from each other in the upper left part where  $\gamma \ll 1$ , indicating the Schwinger exponential behavior and independence of  $\nu$  in Eq. (2.84). In the lower right part, where  $\gamma \gg 1$ , on the other hand, we see the contour lines curve, from which we can only glean it depends on both  $E_0$  and  $\nu$ , but not easily the power law as in (2.85). Note that *small* negative exponents lead to a *large*  $\mathcal{E}(0)$  and thus to a large pair density  $f$ .

A more detailed picture is provided by looking at cuts in this parameter space for constant  $E_0$  and  $\nu$ , see Fig. 2.16. Let us first look at the pure field strength dependence at fixed  $\nu$  in the left panel. From Eq. (2.84) we expect a straight line in the left part of the plot (the adiabatic regime) signifying Schwinger-like pair production, which is exactly what we see. In the right part (the multiphoton regime),  $E_c/E_0 \gg 1$ , so  $\ln(4\frac{m}{\nu}g(\gamma)) \approx \ln \ln \frac{E_c}{E_0} + \text{const}$  which is reflected in the logarithmic curve. This indicates the power-law behavior manifest in the Breit-Wheeler effect. Conversely in the right panel the exponent is independent of  $\nu$  in the left part, therefore the plot is constant there. In the right part, again from Eq. (2.85) and because  $\nu/m \gg 1$ , we have  $\ln(4\frac{m}{\nu}g(\gamma)) \approx -\ln \frac{\nu}{m} + \ln \ln \frac{\nu}{m} + \text{const}$ , which can be seen as the almost straight downward sloping curve.

To show the behavior of  $\mathcal{E}$  and therefore  $f$  over a large region of the parameter space, we had to make a log plot of the exponent. This implies the right scale, at which to look at pair production, is in fact  $\ln |\ln f|$ . With different parameters, the pair density varies over



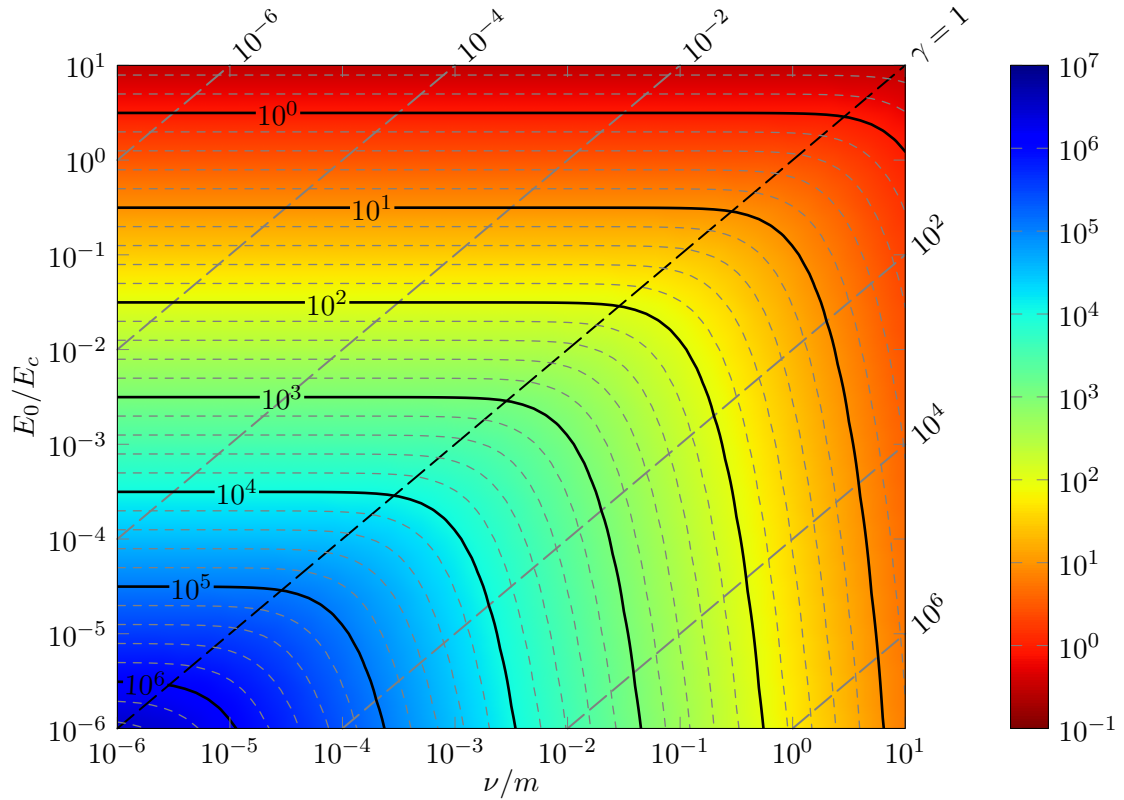


**Figure 2.15:** Contour plot of  $4\frac{m}{\nu}g(\gamma)$ , the negative of the exponent of  $\mathcal{E}(0)$ , over the parameter space. The solid black curves are contour lines at integer powers of 10, the gray short dashed curves at  $10^{0.2}, \dots, 10^{0.8}$  between them. The long dashed lines are the loci of constant Keldysh parameter  $\gamma$ . The color map is inverted compared to Fig. 2.4, because *small* exponents lead to *large*  $f$ . Therefore the same colors correspond to each other in this figure and Fig. 2.4. Red means large, blue small  $f$ .

just too many orders of magnitude to get an intuition for it otherwise. This also cautions us to carefully review and take with a grain of salt claims of enhanced particle production. Increasing  $f$  from  $10^{-1500}$  to  $10^{-500}$  may be a  $10^{1000}$ -fold increase, but the end result is still minuscule. Indeed,  $\ln |\ln 10^{-1500}| = 8.15$  and  $\ln |\ln 10^{-500}| = 7.05$ , not an impressive difference. To overcome the strong exponential suppression of the Schwinger effect, we must overcome this obstacle.

## 2.8 Summary

In this chapter we derived the QKE which is a set of coupled ODEs for the quasi-particle density  $f$ . This was done by diagonalizing the QED Hamiltonian via a Bogoliubov transform. Then we introduced the three types of fields we used, the Schwinger field, the Sauter pulse and the periodic pulse. We treated the first two ones as simple models for the latter one and gave analytical solutions to the QKE for them. We motivated the envelope we chose for the periodic pulse, emphasizing the importance of smoothly switching on and off. We mentioned some numerical implementation details, in particular how the integration over the flat-top interval can be done in logarithmic time and thus very fast, enabling

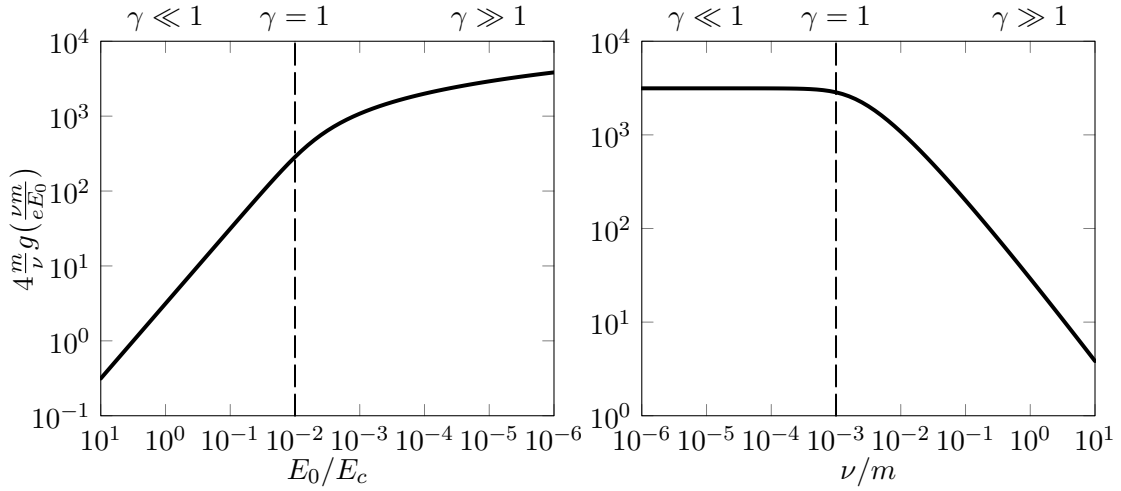


**Figure 2.16:** Cuts through the parameter space shown in Fig. 2.15 for  $\nu = 10^{-2}m$  (left) and  $E_0 = 10^{-3}E_c$  (right). The dashed line denotes  $\gamma = 1$ , left of which  $\gamma \ll 1$  (adiabatic regime) and right of which  $\gamma \gg 1$  (multiphoton regime). Note that the  $E_0$ -axis is reversed in the left panel to have the regimes be on the same side of the  $\gamma = 1$  line in both panels.

long-term studies of the pair density which confirmed Rabi-type oscillations. The residual density turned out to form ridges in the  $p_{\perp}$ - $p_{\parallel}$  phase space, for whose location we found a formula. We derived the behavior of  $f$  close to these ridges and compared the result with the numerics. An integral part of this analysis was performing an integration in the complex time domain via the method of steepest descent. This uncovered the importance of the zeros of the instantaneous energy in the background field  $\Omega(t, \mathbf{p})$  for understanding the residual spectrum  $f$ . We derived an envelope for the peaks of  $f$  and argued that the value of this envelope at  $\mathbf{p} = 0$  is good measure for the overall particle yield, masking out phase space intricacies. At last, we gave a large-scale overview over the parameter space using this particular value of the envelope and showed that in different parameter regions the periodic pulse shows signatures of purely Schwinger-type pair creation, or of Breit-Wheeler-type pair creation.

## 3 Dynamically assisted Schwinger effect

The key idea in the dynamically assisted Schwinger effect is to superpose two fields with different scales, namely a strong but slow field 1 with a weak but fast field 2. This was first put forward in [53, 54]. We laid out the physical intuition behind it in the introduction, but let us repeat briefly: We can imagine field 1 tilting the electron and positron bands in the Dirac sea picture. A particle will then tunnel from the lower to the upper band, leaving a hole (positron) and becoming an electron. The second field will assist this tunneling by lifting the particle a short distance, thus shortening the tunneling distance and exponentially increasing the tunneling probability. This is depicted schematically in Fig. 1.2.

### 3.1 Superposition of two Sauter pulses

#### 3.1.1 Field model

It is not sensible to superpose two Schwinger fields, as they have no inherent time scale that one could change. The sum of both would just be the same field but with a higher field strength. Thus for our first example, we employ two Sauter pulses with their individual  $A$  and  $E$  fields given by Eq. (2.40). Their superposition is then

$$A(t) = -E_1\tau_1 \tanh \frac{t}{\tau_1} - E_2\tau_2 \tanh \frac{t}{\tau_2}, \quad E(t) = \frac{E_1}{\cosh^2 \frac{t}{\tau_1}} + \frac{E_2}{\cosh^2 \frac{t}{\tau_2}}. \quad (3.1)$$

This pulse type was the first studied in context of the dynamically assisted Schwinger effect [53, 54], and also in [60, 101–103]. An interesting variation of this, superposing a spatial with a temporal Sauter-like inhomogeneity, was investigated in [104]. Note that for the Sauter-type pulses we use the time constants  $\tau_i$ , which are in one-to-one correspondence to the frequencies  $\nu_i = 1/\tau_i$  used for periodic pulses.

The rather sloppy terminology of “strong and slow” and “weak and fast” can be made more precise with the help of the Keldysh parameters  $\gamma_i = \frac{E_i}{E_c} \frac{1}{m\tau_i}$ . “Strong and slow” corresponds to  $\gamma_1 < 1$ , also called the adiabatic regime, and “weak and fast” to  $\gamma_2 > 1$ , the multiphoton regime. These are absolute quantifiers for each single field. We also want a relation between them. field 1 is supposed to be “stronger” than field 2,  $E_1 > E_2$ , and at the same time “slower”,  $\tau_1 > \tau_2$ . In the  $E_0$ - $\nu$ -plane as depicted e.g. in Fig. 2.15, this means the parameter point for field 1 must be above and to the left of the dividing  $\gamma = 1$ -line. The point for field 2 must then be below and to the right of that, and also below and to the right of the  $\gamma = 1$ -line. Or to put it more succinctly, the directed line from  $(1/\tau_1, E_1)$  to  $(1/\tau_2, E_2)$  must have a slope between 0 and  $-\pi/2$  and cross the  $\gamma = 1$ -line. We thus

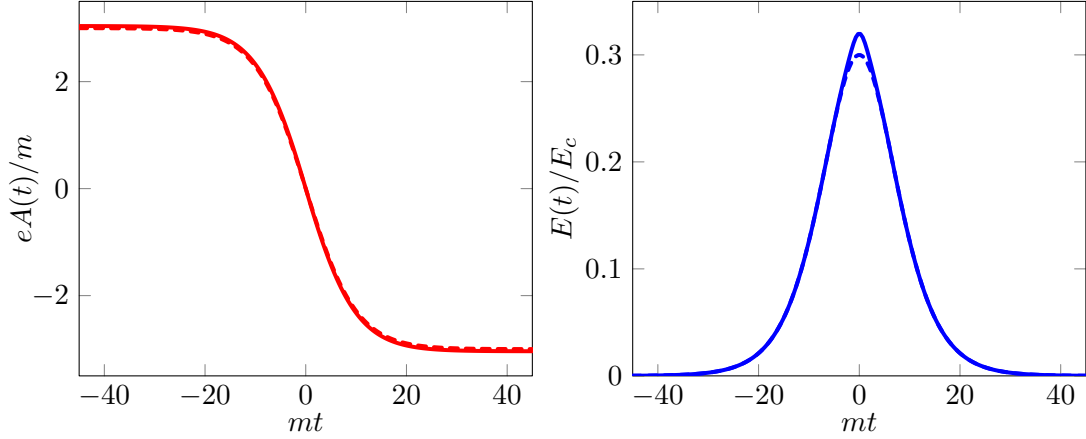


**Figure 3.1:** Plot of the time evolution of the vector potential (left) and electric field (right) for the superposition of two Sauter pulses (3.1) for  $E_1 = 0.3E_c$ ,  $\tau_1 = 10/m$ ,  $E_2 = 0.02E_c$ ,  $\tau_2 = 2/m$ . The dashed lines are for the field 1 alone.

have three constraints on our four parameters:

$$\frac{E_c}{E_1} \frac{1}{m\tau_1} < 1, \quad \frac{E_c}{E_2} \frac{1}{m\tau_2} > 1, \quad E_1 > E_2, \quad \tau_1 > \tau_2. \quad (3.2)$$

They are justified because:

1. If both fields are in the same domain (adiabatic or multiphoton), we can expect no qualitatively new behavior of the pair production. This forces our first two constraints, since the field with  $\gamma < 1$  will simply be named field 1.
2. If we suppose some laser realizes our idealized field models, a trade-off will surely have to be made so that higher field strengths can only be achieved with lower frequencies and vice versa.
3. In the same vein, there is no reason one should expect a second field with  $E_2 < E_1$  but  $\tau_2 > \tau_1$  to have a noticeable positive influence on pair creation. Being both weaker and slower, it cannot assist the first field in any way. (If it were both stronger and faster, we could switch the fields, leaving this argument intact.)

In Fig. 3.1, we show an example time evolution of these fields, where the Keldysh parameters are  $\gamma_1 = 1/3$  and  $\gamma_2 = 25$ . The dashed curves in both plots are for the field 1 alone, cf. Fig. 2.1. Indeed, for the  $A$  field (left panel), the difference between the two is hardly visible. It can be better seen for the  $E$  field in the right panel: the solid line rises in a small bump over the dashed line around  $t = 0$ .<sup>1</sup> The change from adding the field 2 when looking at the time dependence of  $A$  and  $E$  is thus very small.

One might expect such a small change would have only a small impact on the solution  $f$  of the quantum kinetic equation, but that turns out to be false. A hint of this can be seen in Fig. 3.2, where we plot the Fourier transform  $\tilde{E}(\omega)$  of the electric field  $E(t)$ . The maximum is not too much different between field 1 alone (the dashed line) and both combined (the solid line). Yet field 1 alone falls much faster than both fields combined

<sup>1</sup>The difference is bigger in the  $E$ -field, because  $E_2/E_1 > E_2\tau_2/E_1\tau_1$  for  $\tau_1 > \tau_2$ .

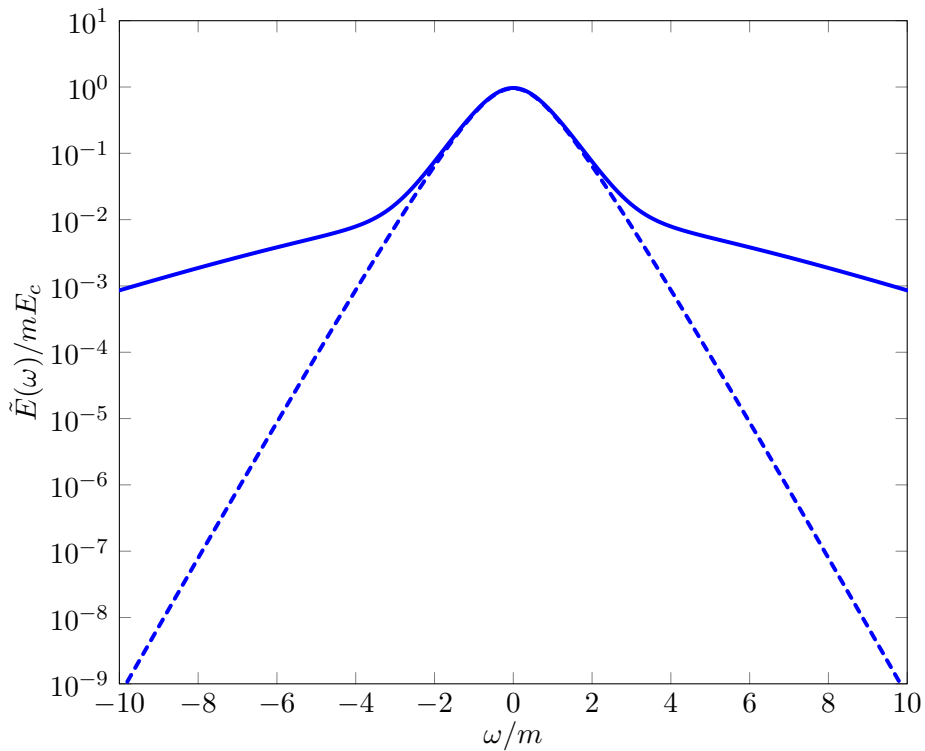


**Figure 3.2:** Plot of the Fourier transform  $\tilde{E}(\omega)$  of the electric field for the superposition of two Sauter pulses (3.1) for  $E_1 = 0.3E_c$ ,  $\tau_1 = 10/m$ ,  $E_2 = 0.02E_c$ ,  $\tau_2 = 2/m$ . The dashed line is for the field 1 alone.

for large frequencies  $\omega$ . In the time domain it is just the opposite, the  $t$  behavior is set by field 1 and does not change from the addition of field 2. This means that the superposition contains more higher-frequency modes. That is to be expected from our “faster” field: Its narrower peak in the time domain causes a wider peak in the frequency domain. These higher-frequency modes can potentially enhance pair creation by providing energy for stimulating the tunneling, as explained above.

### 3.1.2 Numerical results

To test whether this intuition is correct, we need to calculate  $f$  for the two-field case. Unfortunately, it does not have a known analytical solution in (relatively) simple functions as does the single field case (see Eq. (2.41)). So we have to turn to numerics. The implementation works just as for the periodic pulse which we outlined in section 2.4. The only complication is in the lack of definite switch-on/off times. There is no  $t_{\text{on}}$  and  $t_{\text{off}}$  for which  $E(t \leq t_{\text{on}}) = E(t \geq t_{\text{off}}) = 0$ , because the electric field only goes to zero asymptotically. We overcome this obstacle by setting  $t_{\text{on}} = -t_m$ ,  $t_{\text{off}} = t_m$  and successively increasing  $t_m$  until the solution becomes stable, i.e. independent of  $t_m$ . Trying this out for a few sets of parameters and momenta, and also comparing to the analytical solutions as a special case, we found the following rule of thumb:  $t_m$  must be so large, that  $E(-t_m)/E_c = E(t_m)/E_c$  is a few orders of magnitude smaller than the residual  $f$  so calculated.

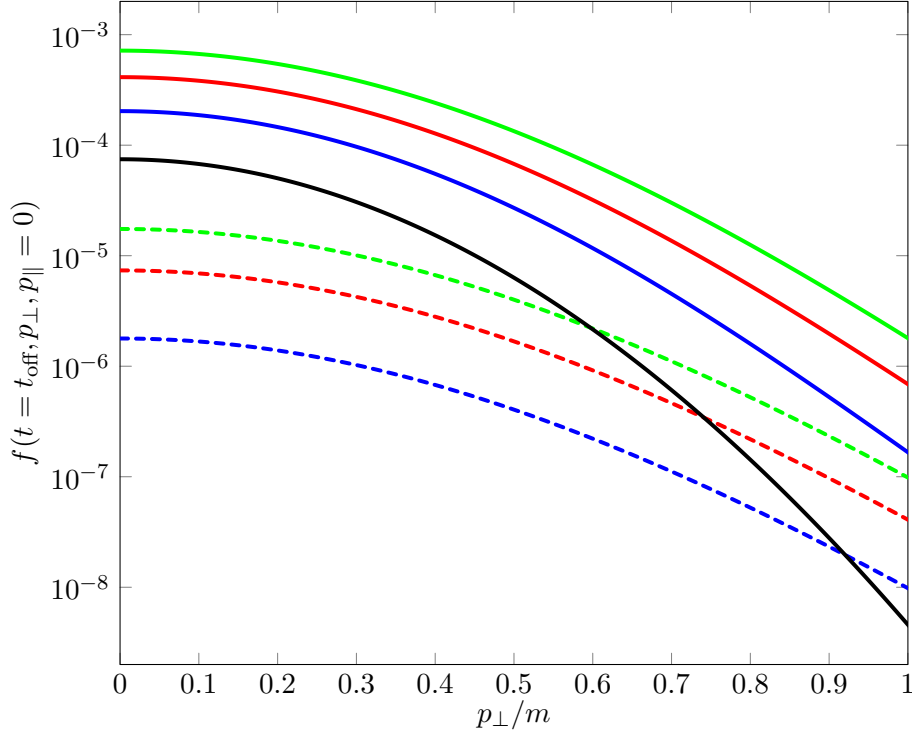


**Figure 3.3:** Plot of the residual pair density  $f$  for the Sauter pulse with two fields as a function of  $p_{\perp}$  at  $p_{\parallel} = 0$  for  $E_1 = 0.3E_c$ ,  $\tau_1 = 10/m$ ,  $\tau_2 = 2/m$  and  $E_2 = 0.02E_c$  (blue),  $E_2 = 0.04E_c$  (red),  $E_2 = 0.06E_c$  (green). The dashed lines are for the first field switched off,  $E_1 = 0$ , and the black curve for the second switched off,  $E_2 = 0$ .

In Fig. 3.3 we show numerical solutions for a set of parameters over  $p_{\perp}$  at  $p_{\parallel} = 0$ . The black curve is the baseline, where only the first field active. The parameters  $E_1$  and  $\tau_1$  are the same as  $E_0$  and  $\tau$  for the green curve in the left panel of Fig. 2.2, but there we plotted the time evolution, not the final state spectrum. So the  $p_{\perp} = 0$  point of the black curve reproduces the out-state ( $t \rightarrow \infty$ ) of this green curve.

To this baseline we add the second field with  $\tau_2 = 2/m$  and increasing  $E_2$  shown by different colors. All three chosen  $E_2$ s put field 2 solidly in the multiphoton regime, with  $\gamma_2 = 25, 12.5, 8.3$ . For small  $p_{\perp}$ , the increase in  $f$  when increasing  $E_2$  is an almost constant factor (as seen by the almost constant distances of the curves in the log plot). It is thus superlinear in  $E_2$ . One might object that this large value of  $f$  is entirely due to field 2, but this is wrong as one can see from the dashed curves. They show the  $f$  that results from only switching on the second field, that is setting  $E_1 = 0$ . Each dashed curve is between one and two orders of magnitude smaller than its corresponding solid counterpart, in which the field 1 is also active. They are also smaller or at most comparable to the black curve. Also note the different large- $p_{\perp}$  asymptotic behavior of  $f$  for the three different cases. The unassisted field falls fastest, the assisting fields slowest, and both combined take the middle ground.

To summarize: fields 1 and 2 on their own produce a moderately large pair density  $f$ , as shown by the black and the dashed curves respectively. But combining both fields yields a far greater  $f$  as both alone, or even as the sum of both single  $f$ s, see the solid curves.

## 3.2 Superposition of two periodic pulses

Our second case is a straightforward generalization of Eq. (2.43):

$$\begin{aligned} A(t) &= K(t) \left[ \frac{E_1}{\nu_1} \cos \nu_1 t + \frac{E_2}{\nu_2} \cos \nu_2 t \right], \\ E(t) &= K(t) [E_1 \sin \nu_1 t + E_2 \sin \nu_2 t] - \dot{K}(t) \left[ \frac{E_1}{\nu_1} \cos \nu_1 t + \frac{E_2}{\nu_2} \cos \nu_2 t \right]. \end{aligned} \quad (3.3)$$

See the text below Eq. (2.43) for an explanation of the envelope  $K(t)$ . This is similar to (3.1) and the motivation for choosing such a field outlined there applies here as well. We will assume  $\nu_2 = N\nu_1$  for  $N \in \mathbb{N}$  because that keeps the pulse periodic in the flat-top regime of  $K$ , which will allow us to adapt the analysis based on the Fourier decomposition from section 2.5.

### 3.2.1 Numerical results

As in the single field case, we are first going to look at a few examples of numerical solutions, see Fig. 3.4. The Keldysh parameter of the first field is  $\gamma_1 = 0.1$  and for the second  $\gamma_2 = 10$  in the upper row and  $\gamma_2 = 6.8$  in the lower. The exact parameters can be found in the figure caption, but for field 1 we chose the same as our model example from the last chapter. This puts the first field in the adiabatic and the second in the multiphoton regime. In the left panels, only the first field is turned on, in the right panels, only the second and in the middle panels, both fields. Both left panels show the same density since only the frequency of the second field changes between them but its field strength is zero in both. As expected we see the same spectrum as in the last chapter for the single field, e.g. in Fig. 2.5 left panel or Fig. 2.14 top left panel.

In both right panels of Fig. 3.4, there is a single sharp peak. In the upper panel, it is higher and at a larger  $p_\perp$  than in the lower due to the larger frequency,  $\nu_2 = 0.5m$  versus  $\nu_2 = 0.34m$ . This spectrum for the weak and fast field<sup>2</sup> looks quite different compared to the strong and slow field, but they are both equally well described by our Fourier-analytic approach. The peaks for field 1 alone simply start at smaller values of  $p_\perp$  and are closer together. In the limit  $\gamma_1 \rightarrow 0$  they become quasi-continuous.

The middle panels of Fig. 3.4 are for the superposition of both pulses. They look very similar to the left panels, but lifted by a factor of about 100. The difference in peak locations is minuscule. Our intuition of the second field assisting the first is thus confirmed. It does not change the spectrum produced by the first field qualitatively, only quantitatively by lifting the shell structures. The enhancement is also relatively robust to changes of  $\nu_2 = N\nu_1$  from  $N = 25$  (upper row) to  $N = 17$  (lower row). The peak height drops by factor of 1.5, while for field 2 alone in the right panel it is a factor of 1000.

<sup>2</sup>We note a caveat about the pulse duration. The envelope function  $K$  has a parameter  $t_{\text{flat}}$  effectively counting how many oscillations occur in the flat-top regime. These are counted using  $\nu_1$ , even when the first field is turned off as in this case. So if there are 50 oscillations for field 1 and  $N = 25$ , field 2 will have made 1250 oscillations. This is an easy mistake to make when doing numerics: Simply inserting the wanted parameters for field 2 into those for field 1 would have field 2 oscillating for only 50 of its periods.

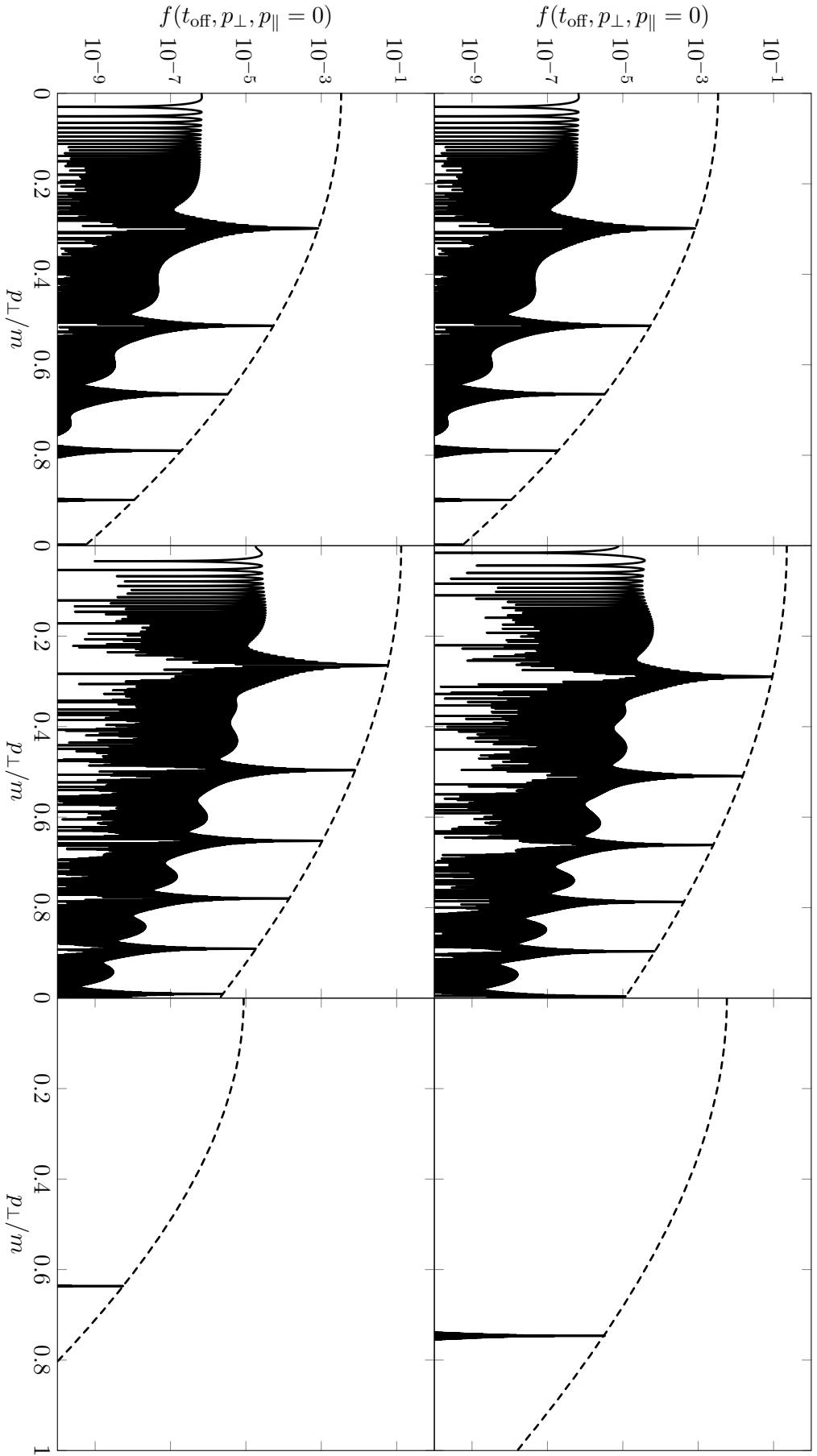


**Figure 3.4:** Plot of the residual phase space density  $f$  as a function of  $p_{\perp}$  at  $p_{\parallel} = 0$  for  $E_1 = 0.22E_c$ ,  $E_2 = 0.05E_c$ ,  $\nu = 0.02m$ ,  $N = 25$  (top) and  $N = 17$  (bottom). In the left panels, only the strong, slow field 1 is turned on; in the right panels, only the weak, fast field 2; in the middle panels, both fields are superimposed.



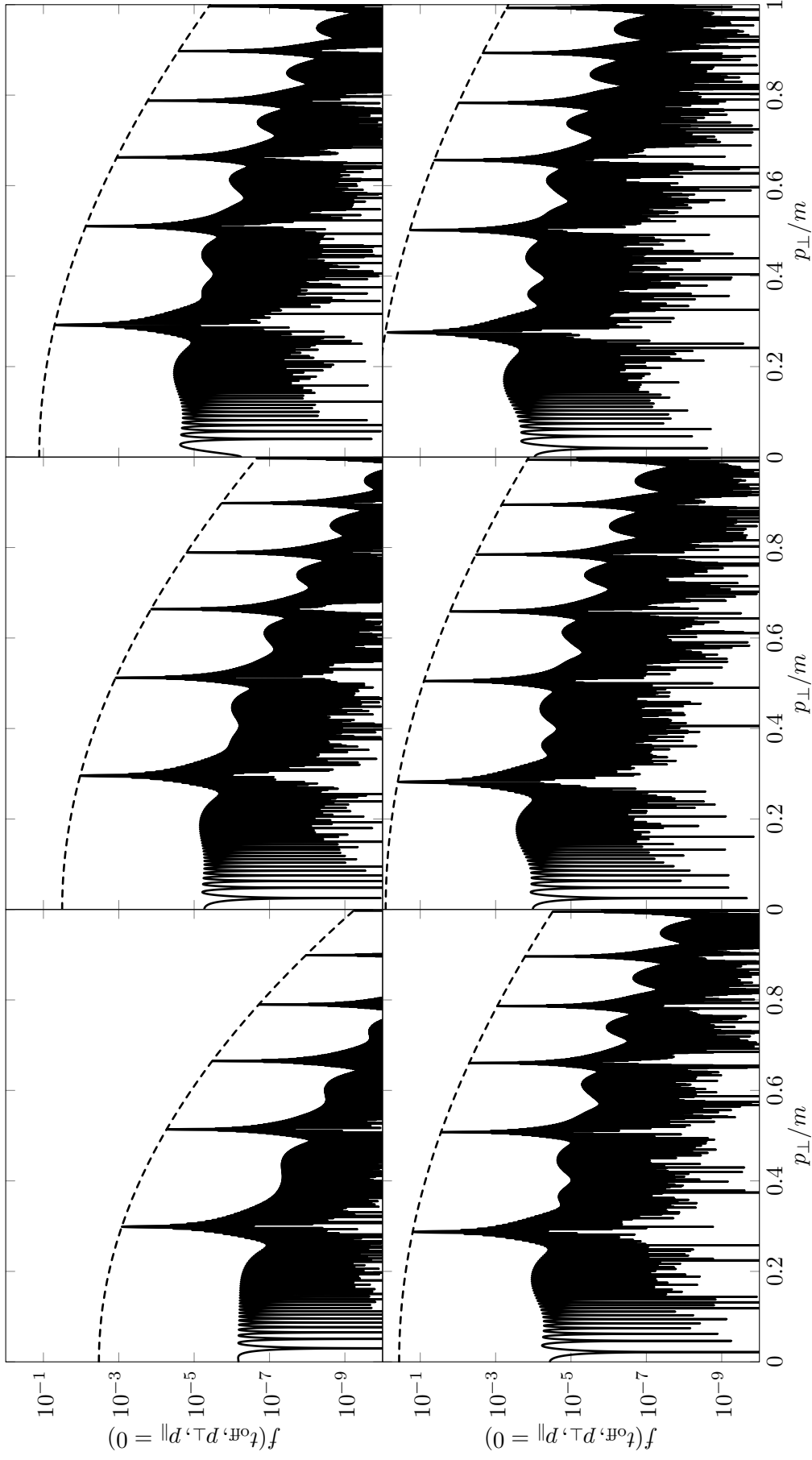


**Figure 3.5:** Plot of the residual phase space density  $f$  as a function of  $p_{\perp}$  at  $p_{\parallel} = 0$  for  $E_1 = 0.2E_c$ ,  $\nu = 0.02m$ ,  $N = 25$  and  $E_2 = 0$  (top left),  $E_2 = 0.02E_c$  (top middle),  $E_2 = 0.04E_c$  (top right),  $E_2 = 0.06E_c$  (bottom left),  $E_2 = 0.08E_c$  (bottom middle),  $E_2 = 0.1E_c$  (bottom right).

In Fig. 3.5, we show more examples, with  $E_2$  increasing from 0 to  $0.1E_c$ . The top left and top middle panels are identical between Figs. 3.4 and 3.5. As one can see, increasing  $E_2$  yields only diminishing returns from some point forth, even in absolute terms (that is, not relative to both pair yields alone; the yield for field 2 alone increases as we increase  $E_2$ ). The intuition behind this is that field 1 can only be assisted so much before its pair production potential is “saturated”. In the Dirac-sea picture, the amount the second field lifts the negative-energy particles is determined by its frequency  $\nu_2$ . The probability for this by  $E_2$ . Once that probability gets large, a significant (order of magnitude) further increase could only come from “double kicks”, i.e. the particle absorbing two quanta of field 2. This would shorten the tunneling length by the same amount as the first kick, yielding another factor of exponential enhancement. But that two-step process is so strongly suppressed that, once  $E_2$  became large enough to make it significant, it would have ceased to be a weak field and entered the  $\gamma_2 < 1$  adiabatic regime, where it behaves not by emitting single quanta but by tilting the energy bands.

Note that in both Figs. 3.4 and 3.5 the dashed lines depict an envelope similar to the one in Fig. 2.14. We have not yet derived its form for the two field case. In the single field case it is given by (2.83). Recall that the key quantity determining the envelope was the location of the zero  $t_0$  in the complex time domain of the quasi-energy  $\Omega(t, p_\perp, p_\parallel)$ . In the two field case, there will turn out to be multiple zeros, so we will first study where they turn up and how they depend on  $E_2$ .

#### 3.2.2 Location and movement of the zeros

Like in the single field case, we will set  $p_\parallel = 0$  to keep things simpler without losing relevant physical details. If the second field is not turned on,  $E_2 = 0$ , there is one zero in the relevant region  $0 \leq \text{Re } t \leq T/2, \text{Im } t > 0$  given by Eq. (2.69). If  $E_2 > 0$  there will be additional zeros. For some integer  $k$ ,  $\cos(kx)$  will be a polynomial of degree  $k$  in  $\cos x$ , the so called Chebyshev polynomials of the first kind  $T_k$ . Applying this to finding our roots we get

$$\begin{aligned} 0 = \Omega(t, \mathbf{p})^2 &= \epsilon_\perp^2 + \left( \frac{eE_1}{\nu_1} \cos(\nu_1 t) + \frac{eE_2}{N\nu_1} \cos(N\nu_1 t) \right)^2 \\ &= \epsilon_\perp^2 + \left( \frac{eE_1}{\nu_1} \cos(\nu_1 t) + \frac{eE_2}{N\nu_1} T_N(\cos(\nu_1 t)) \right)^2. \end{aligned} \quad (3.4)$$

This is a polynomial of degree  $2N$  in  $\cos(\nu_1 t)$ , having  $4N$  solutions  $t_i$  with  $-T/2 \leq \text{Re } t_i \leq T/2$ ,<sup>3</sup> but only  $N$  in the relevant region given above. Their precise locations will of course depend on  $E_2$ , tracing paths as we increase  $E_2$ . There are four different cases of how the zeros move, depending on the remainder of  $N$  modulo 4. We characterize them by how the main zero, already present from the first field alone, moves:

**$N = 4n + 0$**  The main zero moves down and right, the rest of the zeros scattered asymmetrically around (upper left panel of Fig. 3.6).

**$N = 4n + 1$**  The main zero moves straight down, the rest are symmetric around it (upper right panel of Fig. 3.6).

---

<sup>3</sup>We do not attach a subscript to the period  $T$  of field 1. Its definition is the same as in the one field case:  $T = 2\pi/\nu_1$ .

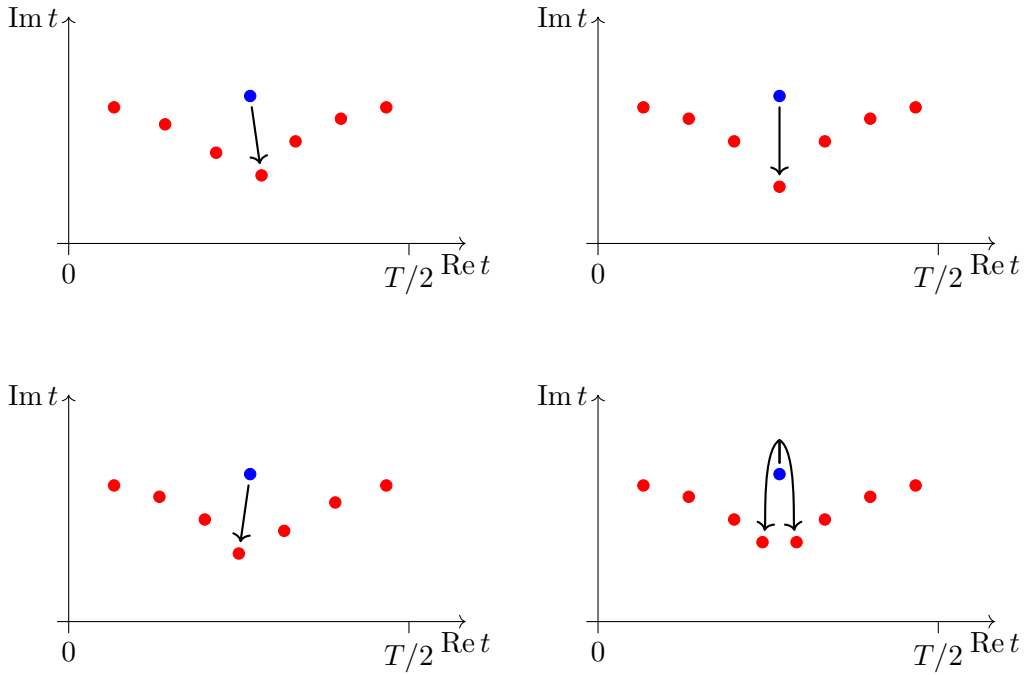


**Figure 3.6:** Schematic plot of the movement of the zeros of  $\Omega^2$  when increasing  $E_2$  in Eq. (3.3). Upper left:  $N = 4n + 0$ ; upper right:  $N = 4n + 1$ ; lower left:  $N = 4n + 2$ ; lower right:  $N = 4n + 3$  for some  $n \in \mathbb{N}$ . The blue point is the only zero when  $E_2 = 0$ . The arrow indicates the way that main zero moves when  $E_2$  increases.

**$N = 4n + 2$**  Just as the case  $N = 4n + 0$ , except the main zero moves to the left and down, instead of right and down (lower left panel of Fig. 3.6).

**$N = 4n + 3$**  The main zero first moves straight up, then collides with a new zero moving down. They then move symmetrically to the left and right respectively, and downwards. The rest of the zeros are symmetric around them (lower right panel of Fig. 3.6).

In the first three cases, the main zero will continue to have an imaginary value smaller than the other zeros. The fourth case is odd, in that the main zero first moves up, and then becomes two zeros once the field strength  $E_2$  passes some threshold. Yet even here their imaginary value is smaller than the rest's. A schematic representation of the movement of the zeros just described can be found in Fig. 3.6.

As long as  $E_2$  is sufficiently smaller than  $E_1$ , the imaginary value of the main zero(s) will be much smaller than that of the others'. The contribution of each zero to  $f$  is  $\propto e^{-\text{Im } \nu_1 t_i}$ . Consequently, if field 2 is really just an assisting field, the main zero will give the main contribution to  $f$ , all others being suppressed exponentially. If  $E_2$  gets too large, all zeros will line up at equal  $\text{Im } t_i$ . That is to be expected, because in that case one can simply neglect  $E_1$  and we are back in the one-field case, but with a "skewed" base frequency of  $\nu_1$  instead of  $N\nu_1$  as would befit field 2 alone. Then we basically just zoomed out of Fig. 2.11, with all the other zeros that are due to the periodicity visible. Summing over all of them will yield a factor of  $N$ , combining with the prefactor  $\nu_1$  to give the previous result.

Distinguishing between the four cases of zero movement is just bookkeeping without

additional physical insight. We will therefore restrict ourselves to  $N = 4n + 1$ , since it is the simplest. Additionally the enhancement will be the largest in this case. In the other cases, the main zero does not move down as much, or it will even move up first (for  $N = 4n + 3$ ), leading to the paradoxical situation that the second field diminishes the pair yield due to some destructive interference.

#### 3.2.3 Envelope for the two field case

All the derivations we did in the sections 2.5 and 2.6 are still valid since they only depend on the field being periodic in the flat-top regime, and  $\Omega$  having a number of zeros from which branch cuts extend. Then, by the method of steepest descent, we arrived at Eq. (2.74) which gives us the amplitude  $I_n$  from the value of  $\Theta(t_0)$  at the root  $t_0$ . This amplitude enters into the formula for the spectrum of  $f(t_{\text{off}})$ , Eq. (2.63), and the envelope (2.83) follows from it. Now we have multiple zeros, but the only change we have to introduce is to extend Eq. (2.74) by a sum over all roots  $t_i$  in the relevant region, i.e.  $0 \leq \text{Re } t_i \leq T/2$  and  $\text{Im } t_i > 0$ . The adapted formula is

$$I_n(p_n) = \frac{4\pi i}{3T} \sum_i \text{Im } e^{2i\Theta(t_i)} \quad (3.5)$$

and we have not yet introduced a further approximation. From our discussion of the location of the zeros it is clear that one zero (or two in the odd case  $N = 4n + 3$ ) will have an imaginary value smaller than the rest. The terms for each  $t_i$  in Eq. (3.5) are suppressed with  $e^{-2\text{Im}\Theta(t_i)} \sim e^{-\text{Im } t_i}$ , that is the root with the smallest imaginary value will dominate the sum. Consequently we only consider the term from that dominating zero and drop the rest. This zero is also just the main zero from field 1 which moved towards the real axis upon increasing  $E_2$ ; we will keep calling it  $t_0$ . Since our focus, as mentioned, is on the  $N = 4n + 1$  case and we have also set  $p_{\parallel} = 0$ , that dominating zero will have  $\text{Re } t_0 = T/4$ . This allows a simplification of  $\Theta(t_0)$  similar to the one-field case given in Eq. (2.77),

$$\begin{aligned} \Theta(t_0) &= \left( \int_0^{T/4} dt + \int_{T/4}^{t_0} dt \right) \sqrt{\epsilon_{\perp}^2 + \left( \frac{eE_1}{\nu_1} \cos(\nu_1 t) + \frac{eE_2}{N\nu_1} \cos(N\nu_1 t) \right)^2} \\ &= \frac{n\pi}{4} + i \frac{\epsilon_{\perp}}{\nu_1} \int_0^{\text{Im } \nu_1 t_0} dx \sqrt{1 - \left( \frac{1}{\delta_1} \sinh x + \frac{1}{\delta_2} \sinh(Nx) \right)^2} \end{aligned} \quad (3.6)$$

with  $\delta_i = \nu_i \epsilon_{\perp} / eE_i$ . We factor the remaining integral into a function  $G(\delta_1, \delta_2, N)$ . In the case  $E_2 = 0$  that corresponds to  $\delta_2 \rightarrow \infty$ ,  $G$  reduces to  $g$  as given by Eq. (2.79):

$$G(\delta_1, \delta_2 \rightarrow \infty, N) = g(\delta_1). \quad (3.7)$$

In that case, we were able to give an explicit expression for the function  $g$  in terms of the hypergeometric function  ${}_2F_1$ , but that does not work here in general. Nevertheless, with the function  $G$  we can define the desired envelope for the two field case, the generalization of Eq. (2.83), as

$$\mathcal{E}(p_{\perp}) = \frac{8\pi^2}{9T^2} \exp \left[ -4 \frac{\epsilon_{\perp}}{\nu_1} G \left( \frac{\nu_1 \epsilon_{\perp}}{eE_1}, \frac{N\nu_1 \epsilon_{\perp}}{eE_2}, N \right) \right] t_{\text{flat}}^2. \quad (3.8)$$

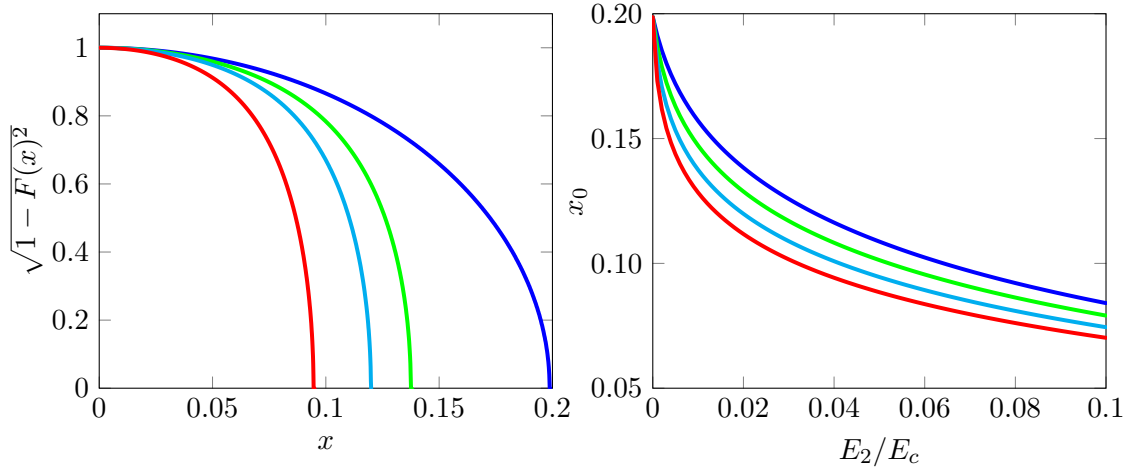


**Figure 3.7:** Left panel: Plot of the integrand in Eq. (3.6) as a function of the imaginary part of the dimensionless time  $x = \text{Im } \nu_1 t$  at  $p_\perp = 0$  for the parameters  $E_1 = 0.1E_c$ ,  $\nu_1 = 0.02m$ ,  $N = 25$  and  $E_2 = 0$  (blue),  $E_2 = 0.01E_c$  (green),  $E_2 = 0.02E_c$  (cyan),  $E_2 = 0.05E_c$  (red). The curves end at  $x_0 = F^{-1}(1)$ . Right panel: Plot of  $x_0$  as a function of  $E_2$  for  $p_\perp = 0$ ,  $E_1 = 0.1E_c$ ,  $\nu_1 = 0.02m$  and  $N = 17$  (blue),  $N = 21$  (green),  $N = 25$  (cyan),  $N = 29$  (red).

This is the envelope shown as a dashed line in Figs. 3.4, 3.5. Although we still have to do a numerical integration to evaluate the envelope, it is considerably simpler than the oscillatory integral from which we started. Only taking into account the main zero in the sum and the envelope is still a good approximation, as the dashed line hugs the peaks just as closely as in the single field case.

To see this and understand the enhancement from field 2, define the function  $F(x)$  as the term in the brackets under the root in Eq. (3.6), that is  $F(x) = \delta_1^{-1} \sinh x + \delta_2^{-1} \sinh(Nx)$ . It is strictly monotonous (thus having an inverse) and  $F(\text{Im } \nu_1 t_0) = 1$ . In terms of this function the integrand is  $\sqrt{1 - F(x)^2}$ . The integral in (3.6) runs from the maximum of the integrand at  $x = 0$  to where it is zero at  $x_0 = F^{-1}(1) = \text{Im } \nu_1 t_0$ . This can be seen in the left panel of Fig. 3.7. The area under the curves plotted there is proportional to  $G$ . As the field strength  $E_2$  is increased from  $E_2 = 0$  for the blue curve, the location of the root  $x_0$  moves further left and the area under the curve gets smaller. Already at  $E_2 = 0.01E_c$  (the green curve), the area is about 26% smaller, reducing the value of  $G$  at  $p_\perp = 0$  from 0.1563 to 0.1151. This does not look like much, but the difference between the two enters in the exponential function multiplied by  $4m/\nu_1$  and thus lifts the envelope by a factor of  $e^{4 \cdot 50 \cdot (0.1563 - 0.1151)} = 3771$ .

The value of  $G$  depends monotonically on  $x_0$ , which is just the imaginary part of the root  $\nu_1 t_0$  in the complex plane. The right panel of Fig. 3.7 shows how  $x_0$  changes with increasing  $E_2$  and for different values of  $N$ . It drops rapidly for even very small  $E_2$ , because the combination  $E_2 \sinh(Nx)$  enters  $F(x)$ . This term grows much faster than  $E_1 \sinh x$  for the first field, thus even starting much smaller it soon becomes comparable to it and can lower  $x_0$  substantially. This is the key insight why the weak second field can lift the shell structures by orders of magnitude. The higher the frequency  $\nu_2 = N\nu_1$ , the larger the effect, as can be seen by the curves for higher  $N$  being lower in the right panel of Fig. 3.7.

The diminishing returns of increasing  $E_2$  are also visible in that the curves' slope becomes much lower at large  $E_2$ .

### 3.3 Summary

In this chapter we superposed two fields of different field strength and time scales. The motivation behind this is that a strong and slow field can be assisted by a weak and fast field to enhance the particle yield by orders of magnitude. We showed this is true for the superposition of two Sauter pulses with the help of numerical solutions. Then we turned to periodic pulses, showed numerical examples and then adapted our previous analysis for one field to this case. This led to a generalized envelope for the peaks of the spectrum. The enhancement effect can be well understood by the movement of the main zero of  $\Omega(t, \mathbf{p})$  upon increasing the field strength of the second field. This movement diminishes an integral entering in the exponent for the envelope and thus causes the order of magnitude enhancement even for small field strengths of the second field.

## 4 Photon signature

So far we have considered an external spatially homogeneous electric field driving the dynamics of the fermions and we studied the  $e^+e^-$ -pairs produced from it. We now want to look at secondary effects, in particular photons created by these pairs. This is motivated by the fact that even when dynamically assisting the pair creation as in chapter 3, the residual density is too small for currently achievable laser fields to be directly experimentally verified. But as mentioned, the intermediate density is in general orders of magnitude larger than the residual density. Since photons could also be sourced by these intermediate pairs, there is the possibility that this large density creates a large observable photon signal. This would also be interesting from a general QFT point of view: In the standard interpretation of QFT only asymptotic states can be meaningfully assigned a particle content. What they represent at intermediate times is not clear. If the asymptotic photons could provide a “snapshot” of the fermions at finite times this could shed light on to what extent they are “real” or “quasi”-particles.

In the probe limit, the background field has no dynamics of its own and is not influenced by the produced pairs. We want to take this one step further by coupling the fermions to a quantized photon field. It will split in two parts, a semiclassical and a quantum part. The former will turn out to be a homogeneous electric field, just as the background field. We can thus add it to the former, which produces a backreaction of the fermions on the background field. This has already been studied in [105–108], so we focus on the second quantum part. We will calculate it in first-order perturbation theory, as in standard QED, and its interpretation is that of photons radiated from the homogeneity region of the background field.

A different approach to ours for studying the photons is deriving equations of motion for correlation functions, which form the so called BBGKY hierarchy, see [109–111].

### 4.1 Backreaction

#### 4.1.1 Normal order and mean-field current

Let us recall our second-quantized Hamiltonian that we diagonalized in the operators  $C_r$  and  $D_r$  with the help of the Bogoliubov transform, see Eq. (2.25). The vacuum expectation value (VEV) of this Hamiltonian has a well-known divergent term, just as in “normal” QED. There one gets rid of this divergence by normal-ordering the Hamiltonian, denoted by  $:H:$ . One computes the normal order by rearranging all  $c_r$ s and  $d_r$ s and their adjoints so that all creation operators appear to the left of all annihilation operators. Whenever one has to exchange two operators, one inserts a minus sign to respect the fermion statistics.

For example,  $:c_r^\dagger c_s: = c_r^\dagger c_s$  but  $:c_r c_s^\dagger: = -c_s^\dagger c_r$ . The VEV of every operator normal-ordered this way is zero, thus also for our  $H$ :  $\langle 0|:H(t):|0\rangle = 0$ . In standard QED this is an intuitively correct result, since the ground state energy does not change with time, and we set it to zero by this procedure. In strong-field QED, however, with the ground state time dependent and the background field creating particles there should be, in general, a non-zero ground state energy. Having it zero at all times is thus undesirable.

A different approach is not normal-ordering w.r.t. the “small” operators  $c_r$  and  $d_r$ , but to the “big” ones,  $C_r$  and  $D_r$ . We denote this by  $\bullet H \bullet$ . For our Hamiltonian, this yields

$$\bullet H(t) \bullet = \int \frac{d^3 p}{(2\pi)^3} \sum_r \Omega(t, \mathbf{p}) \left[ C_r^\dagger(t, \mathbf{p}) C_r(t, \mathbf{p}) + D_r^\dagger(t, -\mathbf{p}) D_r(t, -\mathbf{p}) \right], \quad (4.1)$$

$$\langle 0| \bullet H(t) \bullet |0\rangle = (2\pi)^3 \delta(\mathbf{0}) \int \frac{d^3 p}{(2\pi)^3} 2f(t, \mathbf{p}) \Omega(t, \mathbf{p}). \quad (4.2)$$

The factor  $(2\pi)^3 \delta(\mathbf{0})$  can again be identified with the volume of the system. An educated guess for determining the energy of the system would go like this: We take the number of pairs ( $f$ ), multiply it by two (for particle and anti-particle) and by the effective energy ( $\Omega$ ). Then we sum over all momentum modes (the integral) to get the total energy. This is exactly our result in Eq. (4.2), which tells us that our modified normal-ordering prescription  $\bullet \dots \bullet$  is reasonable and gives physical results. We can define the local energy density  $\epsilon$  so that  $\langle 0| \bullet H(t) \bullet |0\rangle = \int d^3 x \epsilon(t, \mathbf{x})$  holds by setting

$$\epsilon(t, \mathbf{x}) = 2 \int \frac{d^3 p}{(2\pi)^3} f(t, \mathbf{p}) \Omega(t, \mathbf{p}). \quad (4.3)$$

We now apply this to the current by defining the current operator as  $j^\mu(t, \mathbf{x}) = \bullet \bar{\Psi}(t, \mathbf{x}) \gamma^\mu \Psi(t, \mathbf{x}) \bullet$ . Since it will be often referenced later, we give its VEV a symbol of its own,  $\bar{j}^\mu$ , and call it the mean-field part of the operator  $j$ . It is a c-number and with  $\Psi$  from Eqs. (2.8) and (2.22) we find  $\bar{j}^0 = \bar{j}^1 = \bar{j}^2 = 0$  and

$$\bar{j}^3(t, \mathbf{x}) = 2 \int \frac{d^3 p}{(2\pi)^3} \left[ f(t, \mathbf{p}) \frac{p_{\parallel} - eA(t)}{\Omega(t, \mathbf{p})} + u(t, \mathbf{p}) \frac{\epsilon_{\perp}}{\Omega(t, \mathbf{p})} \right]. \quad (4.4)$$

Note that without our adapted normal order,  $\bar{j}^0 \neq 0$ , which is not sensible: the external field cannot create net charge. The current (4.4) is the same as found in [105] from the conservation of energy,  $\frac{1}{2} E(t)^2 + \epsilon(t) = \text{const}$ , and Maxwell's equation  $\dot{E}(t) = -e\bar{j}^3(t)$ .

### 4.1.2 Equation of motions

We will keep using the symbol  $A$  for our background field, and we introduce  $\mathcal{A}$  to designate the operator valued radiation field. The Heisenberg equation of motions for full QED are now coupled equations for the fermion field operator  $\Psi$  and the boson field operator  $\mathcal{A}$ :

$$\begin{aligned} i\partial_t \Psi(t, \mathbf{x}) &= \gamma^0 \left[ -\gamma(i\nabla + e\mathcal{A}(t, \mathbf{x})) + m \right] \Psi(t, \mathbf{x}), \\ \square \mathcal{A}(t, \mathbf{x}) &= e\mathbf{j}(t, \mathbf{x}) + e\mathbf{j}_{\text{ex}}(t, \mathbf{x}), \end{aligned} \quad (4.5)$$

where the current  $j$  is defined by the procedure outlined above as  $j^\mu = \bullet \bar{\Psi} \gamma^\mu \Psi \bullet$ . The external current  $j_{\text{ex}}$  is a c-number in one-to-one correspondence with the external field  $A$ .



Their precise relationship depends on the renormalization which we will do later. Spitting  $j$  into its VEV  $\bar{j}$  and a rest  $j_q$ ,  $j = \bar{j} + j_q$ , motivates a similar split for  $\mathcal{A}$ :  $\mathcal{A} = \bar{\mathcal{A}} + \mathcal{A}_q$ . We split the two equations (4.5) *qua definitione* into three:

$$i\partial_t\Psi(t, \mathbf{x}) = \gamma^0\left[-\gamma(i\nabla + e\bar{\mathcal{A}}(t, \mathbf{x}) + e\mathcal{A}_q(t, \mathbf{x})) + m\right]\Psi(t, \mathbf{x}), \quad (4.6)$$

$$\square\bar{\mathcal{A}}(t, \mathbf{x}) = e\bar{j}(t, \mathbf{x}) + ej_{\text{ex}}(t, \mathbf{x}), \quad (4.7)$$

$$\square\mathcal{A}_q(t, \mathbf{x}) = ej_q(t, \mathbf{x}). \quad (4.8)$$

Putting  $j_{\text{ex}}$  into Eq. (4.7) so that it drives the dynamics of  $\bar{\mathcal{A}}$  is arbitrary (we could also have let it drive  $\mathcal{A}_q$  through (4.8)) but sensible, since both  $\bar{\mathcal{A}}$  and  $\bar{j}$  are c-numbers. That guarantees  $\bar{\mathcal{A}}$  to also be a c-number. We can then interpret  $\bar{\mathcal{A}}$  as the ‘‘classical’’ part of the electromagnetic field, consisting of our background field  $A$  and the backreaction from the created pairs, e.g. the Coulomb force between separated charges. In contrast,  $\mathcal{A}_q$  contains the ‘‘quantum’’ part<sup>1</sup> and refers to the radiation photons.

This split so far does not help us solving the equations. Therefore, we assume  $\mathcal{A}_q$  has no interaction with the fermions, i.e. our system is transparent to the photons. This decouples Eq. (4.8) from both (4.6) and (4.7), resulting in the unperturbed equations

$$i\partial_t\Psi(t, \mathbf{x}) = \gamma^0\left[-\gamma(i\nabla + e\bar{\mathcal{A}}(t, \mathbf{x})) + m\right]\Psi(t, \mathbf{x}), \quad (4.9)$$

$$\square\bar{\mathcal{A}}(t, \mathbf{x}) = e\bar{j}(t, \mathbf{x}) + ej_{\text{ex}}(t, \mathbf{x}). \quad (4.10)$$

Equation (4.9) is just the same as the Dirac equation (2.6) but with  $A$  replaced by  $\bar{\mathcal{A}}$ . The only difference to the dynamical Schwinger effect explored in chapter 2 is the addition of  $\bar{j}$  in Eq. (4.10). Without  $\bar{j}$  and only  $j_{\text{ex}}$  in (4.10) one would have  $\bar{\mathcal{A}} = A$  and Eq. (4.9) would reduce to Eq. (2.6), which in turn leads to the equation of motion for the Bogoliubov coefficients (2.21) and the quantum kinetic equation (2.29). Since the external field and current are spatially homogeneous, so are  $\bar{j}$  and  $\bar{\mathcal{A}}$  and we can carry out the same derivations to reduce Eq. (4.9) to the QKE, but with  $A$  replaced by  $\bar{\mathcal{A}}$ . Furthermore we can insert the current (4.4) into Eq. (4.10). Altogether we get four coupled equations<sup>2</sup>

$$\begin{aligned} \dot{f}(t, \mathbf{p}) &= Q(t, \mathbf{p})u(t, \mathbf{p}), \\ \dot{u}(t, \mathbf{p}) &= Q(t, \mathbf{p})(1 - f(t, \mathbf{p})) - 2\Omega(t, \mathbf{p})v(t, \mathbf{p}), \\ \dot{v}(t, \mathbf{p}) &= 2\Omega(t, \mathbf{p})u(t, \mathbf{p}), \end{aligned} \quad (4.11)$$

$$\ddot{\bar{\mathcal{A}}}(t) = 2e \int \frac{d^3p}{(2\pi)^3} \left[ f(t, \mathbf{p}) \frac{P_{\parallel}}{\Omega(t, \mathbf{p})} + u(t, \mathbf{p}) \frac{\epsilon_{\perp}}{\Omega(t, \mathbf{p})} \right] + ej_{\text{ex}}(t),$$

the three original quantum kinetic equations and one additional describing the backreaction and influence of the external field/current. The auxiliary quantities are

$$\begin{aligned} P_{\parallel} &= p_{\parallel} - e\bar{\mathcal{A}}(t), \\ \Omega(t, \mathbf{p}) &= \Omega(\mathbf{p} - e\bar{\mathcal{A}}(t)) = \sqrt{m^2 + p_{\perp}^2 + P_{\parallel}^2}, \\ Q(t, \mathbf{p}) &= \frac{e\bar{\mathcal{E}}(t)\epsilon_{\perp}}{\Omega(t, \mathbf{p})^2} = -\frac{e\dot{\bar{\mathcal{A}}}(t)\epsilon_{\perp}}{\Omega(t, \mathbf{p})^2}, \end{aligned} \quad (4.12)$$

and the initial conditions  $f(t_{\text{on}}) = u(t_{\text{on}}) = v(t_{\text{on}}) = \bar{\mathcal{A}}(t_{\text{on}}) = \dot{\bar{\mathcal{A}}}(t_{\text{on}}) = 0$ . This set of equations is not well defined, however, because the integral for the mean field current (4.4)

<sup>1</sup>Hence the subscript.

<sup>2</sup>Actually three for each  $\mathbf{p}$  plus one, but we are counting liberally.

is divergent. One can determine the degree of divergence from the asymptotic large  $|\mathbf{p}|$  behavior of  $f$  and  $u$ . Expanding both in powers of  $1/|\mathbf{p}|$ , inserting into (4.11) and comparing equal powers, we find the leading terms

$$f = \frac{1}{8}(e\dot{\bar{\mathcal{A}}})^2 \frac{p_\perp^2}{|\mathbf{p}|^6} + \mathcal{O}(|\mathbf{p}|^{-5}) \quad \text{and} \quad u = -\frac{1}{4}e\ddot{\bar{\mathcal{A}}}\frac{p_\perp}{|\mathbf{p}|^4} + \mathcal{O}(|\mathbf{p}|^{-4}). \quad (4.13)$$

Thus the integral is logarithmically divergent due to the term  $\propto u$  in the integrand. We regularize this similarly to [105] by writing<sup>3</sup>

$$u = u + \frac{e\ddot{\bar{\mathcal{A}}}\epsilon_\perp}{4\Omega^4} - \frac{e\ddot{\bar{\mathcal{A}}}\epsilon_\perp}{4\Omega^4} \quad (4.14)$$

and including the second term on the r.h.s. into the momentum integral, while splitting the third off into a separate integral. The additional terms have the right asymptotic behavior to cancel the divergence, letting us define a regularized version of (4.11) (suppressing time and momentum arguments)

$$\begin{aligned} \ddot{\bar{\mathcal{A}}} &= 2e \int \frac{d^3p}{(2\pi)^3} \left[ f \frac{P_\parallel}{\Omega} + u \frac{\epsilon_\perp}{\Omega} + \frac{e\ddot{\bar{\mathcal{A}}}\epsilon_\perp^2}{4\Omega^5} \right] - e^2 \ddot{\bar{\mathcal{A}}}I(\Lambda) + ej_{\text{ex}}, \\ I(\Lambda) &= 2 \int_{|\mathbf{p}| \leq \Lambda} \frac{d^3p}{(2\pi)^3} \frac{\epsilon_\perp^2}{4\Omega^5}. \end{aligned} \quad (4.15)$$

We made the integral finite by introducing a momentum cutoff  $\Lambda$  which in the end must be sent to infinity,  $\Lambda \rightarrow \infty$ . Now we bring the term  $\propto I(\Lambda)$  on the other side of the equation and define the renormalization factor  $Z = 1/(1 + e^2I(\Lambda))$ , along with the renormalized charge  $e_R = \sqrt{Z}e$  and field  $\bar{\mathcal{A}}_R = \bar{\mathcal{A}}/\sqrt{Z}$ . Note that  $e_R\bar{\mathcal{A}}_R = e\bar{\mathcal{A}}$  and only this combination enters in the first three equations of (4.11), which are thus not affected by the renormalization. A fully renormalized version of Eq. (4.11) is then

$$\begin{aligned} \dot{f} &= Qu, \quad \dot{u} = Q(1-f) - 2\Omega v, \quad \dot{v} = 2\Omega u, \\ \ddot{\bar{\mathcal{A}}}_R &= 2e_R \int \frac{d^3p}{(2\pi)^3} \left[ f \frac{P_\parallel}{\Omega} + u \frac{\epsilon_\perp}{\Omega} + \frac{e_R\ddot{\bar{\mathcal{A}}}_R\epsilon_\perp^2}{4\Omega^5} \right] + e_R j_{\text{ex}}, \end{aligned} \quad (4.16)$$

with

$$P_\parallel = p_\parallel - e_R\bar{\mathcal{A}}_R, \quad \Omega = \sqrt{m^2 + p_\perp^2 + P_\parallel^2}, \quad Q = -\frac{e_R\dot{\bar{\mathcal{A}}}_R\epsilon_\perp}{\Omega^2}. \quad (4.17)$$

Now that the equations are renormalized, we can identify the background field. It couples to the external current through the renormalized charge,  $\ddot{\bar{\mathcal{A}}} = e_R j_{\text{ex}}$ . For typographic reasons we rename  $e_R \rightarrow e$  from now on.

In the following we will need a variant of Eq. (4.16), where we replace the QKE part corresponding to Eq. (2.29) with one for the Bogoliubov coefficients, see Eq. (2.21). Both (2.29) and (2.21) are equivalent,<sup>4</sup> so this is permissible. Additionally we need to replace  $f \rightarrow 2|\beta|^2$  and  $u \rightarrow -2\text{Re}(\alpha^*\beta)$  in the backreaction part and get

$$\begin{aligned} \dot{\alpha} &= -i\Omega\alpha + \frac{1}{2}Q\beta, \quad \dot{\beta} = -\frac{1}{2}Q\alpha + i\Omega\beta, \\ \ddot{\bar{\mathcal{A}}} &= 2e \int \frac{d^3p}{(2\pi)^3} \left[ 2|\beta|^2 \frac{P_\parallel}{\Omega} - 2\text{Re}(\alpha^*\beta) \frac{\epsilon_\perp}{\Omega} + \frac{e\ddot{\bar{\mathcal{A}}}\epsilon_\perp^2}{4\Omega^5} \right] + ej_{\text{ex}}. \end{aligned} \quad (4.18)$$

<sup>3</sup>The asymptotic behavior of  $f$  and  $u$  and thus the regularization is not correct in [105], because the asymmetry in  $p_\perp$  and  $p_\parallel$  was not taken into account.

<sup>4</sup>To see this, see appendix B.2.

## 4.2 A formula for the photon spectrum

We now want to determine the photon spectrum resulting from the quantum part of the electromagnetic field  $\mathcal{A}_q$ . In this we follow [50, 51], where this was done for a time dependent effective mass resulting from the chiral phase transition. This mass takes the role of our background field and drives the time evolution of  $\Psi$  producing pairs. The rest of the logic is the same, although the backreacting  $\bar{\mathcal{A}}$  part was not addressed in [50, 51].

Consider a solution of Eq. (4.8) which we expand in spatial Fourier modes as

$$\mathcal{A}_q(t, \mathbf{x}) = \int \frac{d^3k}{\sqrt{2\omega}(2\pi)^3} \sum_{\lambda} \left[ a_{\lambda}(t, \mathbf{k}) \epsilon_{\lambda}(\mathbf{k}) e^{i\mathbf{k}\mathbf{x}} + \text{c.c.} \right] \quad (4.19)$$

with  $\omega = |\mathbf{k}|$  the photon frequency and  $\epsilon_{\lambda}(\mathbf{k})$  the two polarization vectors ( $\lambda = 1, 2$ ) for each wave-vector  $\mathbf{k}$ . If  $\mathcal{A}_q$  were a free field, i.e.  $\square \mathcal{A}_q = 0$ , then  $a_{\lambda}(t, \mathbf{k}) = a_{\lambda}(\mathbf{k}) e^{-i\omega t}$ , where  $a_{\lambda}(\mathbf{k})$  are the base bosonic operators building up the Fock space. In particular  $a_{\lambda}(\mathbf{k}) |0\rangle = 0$ .<sup>5</sup> The full equation (4.8) can be generated by an interaction Hamiltonian

$$H_{\text{int}}(t) = -e \int d^3x \mathcal{A}_q(t, \mathbf{x}) \mathbf{j}_q(t, \mathbf{x}) \quad (4.20)$$

via Heisenberg's equations of motion. This suggests solving (4.8) with the help of Dyson's series in a standard QED perturbation series. We restrict ourselves to the non-trivial leading order and arrive at (omitting a few steps and intricacies of shuffling operators back and forth between pictures)

$$\begin{aligned} a_{\lambda}(t, \mathbf{k}) &= a_{\lambda}(\mathbf{k}) e^{-i\omega t} + i \int_{t_0}^t dt' \left[ H_{\text{int}}(t'), a_{\lambda}(\mathbf{k}) e^{-i\omega t'} \right] + \mathcal{O}(e^2) \\ &= \left[ a_{\lambda}(\mathbf{k}) + i \frac{e}{\sqrt{2\omega}} \int_{t_0}^t dt' \int d^3x \epsilon_{\lambda}^*(\mathbf{k}) \mathbf{j}_q(t', \mathbf{x}) e^{i\mathbf{k}\mathbf{x}} \right] e^{-i\omega t} + \mathcal{O}(e^2). \end{aligned} \quad (4.21)$$

The renormalized QKE with backreaction (4.16) together with Eq. (4.21) constitutes a solution to the original operator equations (4.5) up to order  $\mathcal{O}(e)$ , but with the mean-field part of the current taken into account exactly. Since the first order correction in Eq. (4.21) is  $\propto e \epsilon_{\lambda}^*$ , the charge renormalization as described above does not change it.

Let us now turn to the expectation value of  $a_{\lambda}^{\dagger}(t) a_{\lambda}(t)$ . For its evaluation it is important to note  $\mathbf{j}_q = \mathbf{j} - \bar{\mathbf{j}} = \bullet \bar{\Psi} \boldsymbol{\gamma} \Psi \bullet - \langle 0 | \bullet \bar{\Psi} \boldsymbol{\gamma} \Psi \bullet | 0 \rangle = : \bar{\Psi} \boldsymbol{\gamma} \Psi :$ . That is, the difference between our ‘‘improved’’ normal order of the current and its VEV is just the standard normal order. This is also the current used in [50, 51] from the outset and because of this the mean-field part is neglected there. Note the spatially Fourier transformed current in Eq. (4.21),  $\int d^3x \mathbf{j}_q(t', \mathbf{x}) e^{i\mathbf{k}\mathbf{x}}$ . We can express that current with the spinor field operator from Eq. (2.8) as

$$\int d^3x \mathbf{j}_q(t', \mathbf{x}) e^{i\mathbf{k}\mathbf{x}} = \int \frac{d^3p}{(2\pi)^3} : \bar{\psi}(t', \mathbf{p}) \boldsymbol{\gamma} \psi(t', \mathbf{p} - \mathbf{k}) :. \quad (4.22)$$

<sup>5</sup>Technically speaking,  $a_{\lambda}(t, \mathbf{k})$  is in the Heisenberg picture of time evolution, while  $a_{\lambda}(\mathbf{k})$  is in the Schrödinger picture and  $a_{\lambda}(\mathbf{k}) e^{-i\omega t}$  in the Interaction picture. We do not, however, distinguish between pictures typographically, as we assume no confusion will arise.

In computing the expectation value from Eq. (4.21), all the mixed terms drop out leaving eventually

$$\begin{aligned} \langle 0 | a_\lambda^\dagger(t, \mathbf{k}) a_\lambda(t, \mathbf{k}) | 0 \rangle &= \frac{e^2}{2\omega} \sum_{ij} \epsilon_\lambda^i(\mathbf{k}) \epsilon_\lambda^{j*}(\mathbf{k}) \int_{t_0}^t dt_1 \int_{t_0}^t dt_2 \int \frac{d^3 p_1}{(2\pi)^3} \int \frac{d^3 p_2}{(2\pi)^3} \\ &\times \langle 0 | : \bar{\psi}(t_1, \mathbf{p}_1) \gamma_i \psi(t_1, \mathbf{p}_1 - \mathbf{k}) :^\dagger : \bar{\psi}(t_2, \mathbf{p}_2) \gamma_j \psi(t_2, \mathbf{p}_2 - \mathbf{k}) : | 0 \rangle. \end{aligned} \quad (4.23)$$

The expectation value of the normal ordered currents can be computed more easily by first observing that from the decomposition (2.22) the relation

$$: \bar{\psi}(t, \mathbf{p}) \gamma \psi(t, \mathbf{p} - \mathbf{k}) : | 0 \rangle = \sum_{rs} \bar{u}_r(t, \mathbf{p}) \gamma v_s(t, -\mathbf{p} + \mathbf{k}) c_r^\dagger(\mathbf{p}) d_s^\dagger(-\mathbf{p} + \mathbf{k}) | 0 \rangle \quad (4.24)$$

follows. The remaining operators create two delta functions,  $\delta(\mathbf{0})$  and  $\delta(\mathbf{p}_1 - \mathbf{p}_2)$ , when Eq. (4.24) is inserted into Eq. (4.23). This cancels one momentum integration. The two time integrals turn out to be the complex conjugate of each other and are grouped together as the squared modulus of one time integral. When all is sorted out, we arrive at

$$\begin{aligned} \langle 0 | a_\lambda^\dagger(t, \mathbf{k}) a_\lambda(t, \mathbf{k}) | 0 \rangle &= \\ &= \frac{e^2}{2\omega(2\pi)^3} (2\pi)^3 \delta(\mathbf{0}) \int d^3 p \sum_{r,s} \left| \int_{t_0}^t dt' \bar{v}_r(t', -\mathbf{p}) \epsilon_\lambda(\mathbf{k}) \gamma u_s(t', \mathbf{p} - \mathbf{k}) e^{-i\omega t'} \right|^2. \end{aligned} \quad (4.25)$$

Here  $u_r$  and  $v_r$  are the solutions of Dirac's equation that we used in the derivation of the QKE and which follow from the Bogoliubov coefficients through Eq. (2.20). We once again encounter the divergent volume factor due to the spatial homogeneity of our system. It forces us to norm our photon spectrum to the volume. We also want to send  $t_0 \rightarrow -\infty$  and  $t \rightarrow \infty$ .<sup>6</sup> For this we need to regularize the time integral by a factor that adiabatically switches the interaction with the radiation field on and off. Otherwise, the photon spectrum would be non-zero even without an external field. Therefore, we let

$$\int_{t_0}^t dt' \rightarrow \lim_{\varepsilon \rightarrow 0} \int_{-\infty}^{\infty} dt' e^{-\varepsilon|t'|} \quad (4.26)$$

in Eq. (4.25). Finally we can define and compute the differential photon spectrum  $f_\gamma(\mathbf{k})$  as

$$\begin{aligned} f_\gamma(\mathbf{k}) &= \frac{1}{(2\pi)^3 V} \sum_\lambda \langle 0 | a_\lambda^\dagger(t, \mathbf{k}) a_\lambda(t, \mathbf{k}) | 0 \rangle \Big|_{t_0 \rightarrow -\infty}^{t \rightarrow \infty} \\ &= \frac{e^2}{2\omega(2\pi)^6} \int d^3 p \sum_{\lambda, r, s} \left| \epsilon_\lambda^i(\mathbf{k}) C_{rsi}(\mathbf{p}, \mathbf{k}) \right|^2 \end{aligned} \quad (4.27)$$

with

$$C_{rsi}(\mathbf{p}, \mathbf{k}) = \lim_{\varepsilon \rightarrow 0} \int_{-\infty}^{\infty} dt e^{-\varepsilon|t|} \bar{v}_r(t, -\mathbf{p}) \gamma_i u_s(t, \mathbf{p} - \mathbf{k}) e^{-i\omega t}. \quad (4.28)$$

<sup>6</sup>Note that both  $t_0$  and  $t$  are independent of the switch-on/off times of the external field  $A$ ,  $t_{\text{on}}$  and  $t_{\text{off}}$ . Also  $t_0$  has no relation to the zero of  $\Omega$  in the complex plane that we also called  $t_0$ .

### 4.2.1 Evaluation of $C_{rsi}$

To evaluate  $C_{rsi}$  from Eq. (4.28) which we want to plug into (4.27) to compute  $f_\gamma$ , we have to first solve (4.18). For this we will neglect the backreaction, that is ignore the second line of Eq. (4.18) and set  $\bar{A} = A$ ; or, to put it differently, we simply use the original equation for the Bogoliubov coefficients (2.21). One might wonder why we went through the trouble of implementing the backreaction, when we ignore it for computing the photon spectrum. The answer is twofold: First, it is the correct approach since, in particular, we used the correctly normal ordered current. Second, it was needed to carry out the renormalization. Neglecting the properly renormalized equation is then a systematic approximation, in contrast to leaving it out a priori.

For evaluating  $C_{rsi}$  from Eq. (4.28), the limiting procedure  $\varepsilon \rightarrow 0$  poses a problem. It is difficult and expensive to implement numerically. One would have to cache the solutions of  $\alpha$  and  $\beta$  from which  $u_r$  and  $v_r$  are computed at all time steps, then compute the time integral for different  $\varepsilon$  and extrapolate the limit. This forces a fixed set of points  $t_i$  on which to evaluate the integrand, foiling attempts of our chosen integrator to be more intelligent. Additionally we have to integrate over a large time interval to correctly capture the asymptotic oscillatory behavior (and we would have to do extra analysis to avoid aliasing issues in the integration). An alternative would be doing the entire time evolution again for each  $\varepsilon$ , but that seems even more prohibitively computationally expensive. (Remember that we have to do this for a probably very large number of momenta  $\mathbf{p}$ , over which we also have to integrate in Eq. (4.27).)

We therefore seek to do the limit analytically, with a remainder to be evaluated numerically. For this we need to look at the asymptotic form of  $u_r$  and  $v_r$  before the external field was switched on at  $t_{\text{on}}$  and after it was switched off at  $t_{\text{off}}$ . This makes the time evolution of  $\alpha$  and  $\beta$  simple before switching on and after switching off. Define  $\mathbf{P}_{\text{on/off}} = \mathbf{p} - e\mathbf{A}(t_{\text{on/off}})$  as the canonical momentum before/after switching on/off. Then from Eq. (2.21) we get

$$\begin{aligned} \alpha(t \leq t_{\text{on}}) &= e^{-i\Omega(\mathbf{P}_{\text{on}})(t-t_{\text{on}})}, & \beta(t \leq t_{\text{on}}) &= 0, \\ \alpha(t \geq t_{\text{off}}) &= e^{-i\Omega(\mathbf{P}_{\text{off}})(t-t_{\text{off}})}\alpha(t_{\text{off}}), & \beta(t \geq t_{\text{off}}) &= e^{i\Omega(\mathbf{P}_{\text{off}})(t-t_{\text{off}})}\beta(t_{\text{off}}) \end{aligned} \quad (4.29)$$

and with these inserted into Eq. (2.20)

$$\begin{aligned} u_r(t \leq t_{\text{on}}, \mathbf{p}) &= e^{-i\Omega(\mathbf{P}_{\text{on}})(t-t_{\text{on}})}u_r(\mathbf{P}_{\text{on}}), \\ v_r(t \leq t_{\text{on}}, -\mathbf{p}) &= e^{i\Omega(\mathbf{P}_{\text{on}})(t-t_{\text{on}})}v_r(-\mathbf{P}_{\text{on}}), \\ u_r(t \geq t_{\text{off}}, \mathbf{p}) &= e^{-i\Omega(\mathbf{P}_{\text{off}})(t-t_{\text{off}})}\alpha(t_{\text{off}}, \mathbf{p}) u_r(\mathbf{P}_{\text{off}}) \\ &\quad + e^{i\Omega(\mathbf{P}_{\text{off}})(t-t_{\text{off}})} \beta(t_{\text{off}}, \mathbf{p}) v_r(-\mathbf{P}_{\text{off}}), \\ v_r(t \geq t_{\text{off}}, -\mathbf{p}) &= -e^{-i\Omega(\mathbf{P}_{\text{off}})(t-t_{\text{off}})}\beta^*(t_{\text{off}}, \mathbf{p})u_r(\mathbf{P}_{\text{off}}) \\ &\quad + e^{i\Omega(\mathbf{P}_{\text{off}})(t-t_{\text{off}})} \alpha^*(t_{\text{off}}, \mathbf{p})v_r(-\mathbf{P}_{\text{off}}). \end{aligned} \quad (4.30)$$

The time independent base spinors  $u_r(\mathbf{p})$  and  $v_r(\mathbf{p})$  are given by Eq. (2.14). Now that we know the behavior of the solutions  $u_r(t)$  and  $v_r(t)$ , we can carry out the limiting procedure in the definition (4.28) of  $C_{rsi}$ . We split the time integral into three parts,  $\int_{-\infty}^{t_{\text{on}}} + \int_{t_{\text{on}}}^{t_{\text{off}}} + \int_{t_{\text{off}}}^{\infty}$ , and use the expressions (4.30) to do the half-infinite integrals. For

example, the first summand is

$$\begin{aligned}
 & \int_{-\infty}^{t_{\text{on}}} dt e^{-\varepsilon|t|} \bar{v}_r(t, -\mathbf{p}) \gamma_i u_s(t, \mathbf{p} - \mathbf{k}) e^{-i\omega t} \\
 &= \int_{-\infty}^{t_{\text{on}}} dt e^{\varepsilon t} e^{-i\Omega(\mathbf{P}_{\text{on}})(t-t_{\text{on}})} e^{-i\Omega(\mathbf{P}_{\text{on}}-\mathbf{k})(t-t_{\text{on}})} e^{-i\omega t} \bar{v}_r(-\mathbf{P}_{\text{on}}) \gamma_i u_s(t, \mathbf{P}_{\text{on}} - \mathbf{k}) \quad (4.31) \\
 &= \frac{\bar{v}_r(-\mathbf{P}_{\text{on}}) \gamma_i u_s(t, \mathbf{P}_{\text{on}} - \mathbf{k}) e^{\varepsilon t_{\text{on}} - i\omega t_{\text{on}}}}{\varepsilon - i\Omega(\mathbf{P}_{\text{on}}) - i\Omega(\mathbf{P}_{\text{on}} - \mathbf{k}) - i\omega} \xrightarrow{\varepsilon \rightarrow 0} i \frac{\bar{v}_r(-\mathbf{P}_{\text{on}}) \gamma_i u_s(t, \mathbf{P}_{\text{on}} - \mathbf{k})}{\omega + \Omega(\mathbf{P}_{\text{on}}) + \Omega(\mathbf{P}_{\text{on}} - \mathbf{k})} e^{-i\omega t_{\text{on}}}.
 \end{aligned}$$

The integral  $\int_{t_{\text{off}}}^{\infty}$  can be done in the same way. The middle integral is over a finite length of time, therefore the limit  $\varepsilon \rightarrow 0$  can be done immediately. Collecting all terms gives

$$\begin{aligned}
 C_{rsi}(\mathbf{p}, \mathbf{k}) &= \int_{t_{\text{on}}}^{t_{\text{off}}} dt \bar{v}_r(t, -\mathbf{p}) \gamma_i u_s(t, \mathbf{p} - \mathbf{k}) e^{-i\omega t} + i \frac{\bar{v}_r(-\mathbf{P}_{\text{on}}) \gamma_i u_s(\mathbf{P}_{\text{on}} - \mathbf{k})}{\omega + \Omega(\mathbf{P}_{\text{on}}) + \Omega(\mathbf{P}_{\text{on}} - \mathbf{k})} e^{-i\omega t_{\text{on}}} \\
 &\quad - i\alpha(t_{\text{off}}, \mathbf{p}) \alpha(t_{\text{off}}, \mathbf{p} - \mathbf{k}) \frac{\bar{v}_r(-\mathbf{P}_{\text{off}}) \gamma_i u_s(\mathbf{P}_{\text{off}} - \mathbf{k})}{\omega + \Omega(\mathbf{P}_{\text{off}}) + \Omega(\mathbf{P}_{\text{off}} - \mathbf{k})} e^{-i\omega t_{\text{off}}} \\
 &\quad - i\alpha(t_{\text{off}}, \mathbf{p}) \beta(t_{\text{off}}, \mathbf{p} - \mathbf{k}) \frac{\bar{v}_r(-\mathbf{P}_{\text{off}}) \gamma_i v_s(-\mathbf{P}_{\text{off}} + \mathbf{k})}{\omega + \Omega(\mathbf{P}_{\text{off}}) - \Omega(\mathbf{P}_{\text{off}} - \mathbf{k})} e^{-i\omega t_{\text{off}}} \quad (4.32) \\
 &\quad + i\beta(t_{\text{off}}, \mathbf{p}) \alpha(t_{\text{off}}, \mathbf{p} - \mathbf{k}) \frac{\bar{u}_r(\mathbf{P}_{\text{off}}) \gamma_i u_s(\mathbf{P}_{\text{off}} - \mathbf{k})}{\omega - \Omega(\mathbf{P}_{\text{off}}) + \Omega(\mathbf{P}_{\text{off}} - \mathbf{k})} e^{-i\omega t_{\text{off}}} \\
 &\quad + i\beta(t_{\text{off}}, \mathbf{p}) \beta(t_{\text{off}}, \mathbf{p} - \mathbf{k}) \frac{\bar{u}_r(\mathbf{P}_{\text{off}}) \gamma_i v_s(-\mathbf{P}_{\text{off}} + \mathbf{k})}{\omega - \Omega(\mathbf{P}_{\text{off}}) - \Omega(\mathbf{P}_{\text{off}} - \mathbf{k})} e^{-i\omega t_{\text{off}}}.
 \end{aligned}$$

This is as far as analytical considerations will take us. Now, for a given  $A$  field we have to solve Eq. (2.21) numerically and with this solution do the remaining time integral in (4.32) also numerically. The values of  $\alpha$  and  $\beta$  at the end of the numerical solution are used to compute the remaining terms arising from the asymptotic behavior in (4.32).

#### 4.2.2 Small- and large-frequency behavior of $C_{rsi}$

When we let  $\omega \rightarrow 0$ , most terms in Eq. (4.32) are of order  $\mathcal{O}(1)$ ,<sup>7</sup> except the two in the third and fourth line proportional to  $\alpha\beta$ . For them we need to look at the denominators  $\omega \pm (\Omega(\mathbf{P}_{\text{off}}) - \Omega(\mathbf{P}_{\text{off}} - \mathbf{k}))$ . To the lowest non vanishing order  $\Omega(\mathbf{P}_{\text{off}} - \mathbf{k}) = \Omega(\mathbf{P}_{\text{off}}) - \mathbf{P}_{\text{off}} \cdot \mathbf{k} / \Omega(\mathbf{P}_{\text{off}})$  and inserting this in the denominators in Eq. (4.32) yields

$$\begin{aligned}
 C_{rsi}(\mathbf{p}, \mathbf{k}) &= -i\alpha(t_{\text{off}}, \mathbf{p}) \beta(t_{\text{off}}, \mathbf{p}) \left[ \frac{\bar{v}_r(-\mathbf{P}_{\text{off}}) \gamma_i v_s(-\mathbf{P}_{\text{off}})}{\omega + \frac{\mathbf{P}_{\text{off}} \cdot \mathbf{k}}{\Omega(\mathbf{P}_{\text{off}})}} + \frac{\bar{u}_r(\mathbf{P}_{\text{off}}) \gamma_i u_s(\mathbf{P}_{\text{off}})}{\omega - \frac{\mathbf{P}_{\text{off}} \cdot \mathbf{k}}{\Omega(\mathbf{P}_{\text{off}})}} \right] \\
 &\quad + \mathcal{O}(\omega^0). \quad (4.33)
 \end{aligned}$$

The new denominators in the brackets look suspicious, but in fact  $\omega\Omega(\mathbf{P}_{\text{off}}) > |\mathbf{P}_{\text{off}} \cdot \mathbf{k}|$ , so they can only become zero when  $\omega$  does. By writing  $\mathbf{k} = \omega \mathbf{e}_k$  we can factor  $\omega$  out as

<sup>7</sup>Since Eq. (2.21) is a well posed problem, both  $\alpha$  and  $\beta$  are at least continuous in the momentum argument  $\mathbf{p}$ . Therefore,  $\alpha(t_{\text{off}}, \mathbf{p} - \mathbf{k}) \xrightarrow{\omega \rightarrow 0} \alpha(t_{\text{off}}, \mathbf{p})$ .

$\omega \pm \mathbf{P}_{\text{off}} \cdot \mathbf{k} / \Omega(\mathbf{P}_{\text{off}}) = \omega [1 \pm \mathbf{P}_{\text{off}} \cdot \mathbf{e}_k / \Omega(\mathbf{P}_{\text{off}})]$  which makes this even clearer. Asymptotically for small  $\omega$ ,  $C_{rsi} \propto 1/\omega$  with the constant of proportionality only dependent on  $\mathbf{p}$  and the direction of  $\mathbf{k}$ ,  $\mathbf{e}_k$ . Inserted into Eq. (4.27) we see this constant gets squared and integrated over all  $\mathbf{p}$ , turning it into another constant only depending on  $\mathbf{e}_k$ . Therefore,

$$f_\gamma(\mathbf{k}) = \frac{e^2 c(\mathbf{e}_k)}{\omega^3} + \mathcal{O}(\omega^{-2}) \quad (4.34)$$

with all constants except  $e^2$  collected into  $c(\mathbf{e}_k)$ . This behavior is a typical QED infrared divergence. Note that although the total number of photons  $\int d^3k f_\gamma$  is also divergent, the total energy  $\int d^3k \omega f_\gamma$  remains finite.<sup>8</sup>

How can we interpret this divergence? Inspecting the terms in Eq. (4.32), the divergence can be traced back to lines three and four. These are proportional to  $\bar{v}_r \gamma_i v_s$  and  $\bar{u}_r \gamma_i u_s$ , which are amplitudes for scattering of a quasi-anti-particle to quasi-anti-particle and quasi-particle to quasi-particle respectively while emitting a photon. The divergence can thus be interpreted as bremsstrahlung from virtual quasi-particles. Handling this divergence proceeds in the same way as in standard QED. Informally speaking: Since every photon detector has a minimal energy resolution  $\omega_{\text{min}}$ , any photon with  $\omega < \omega_{\text{min}}$  is unobservable to this detector. One cannot then distinguish between a particle and a particle accompanied by such a photon. By identifying both scenarios as one state, the divergence moves to the out-state of the particle and is canceled by higher-order loop contributions. The details of this can be found in any textbook on QFT, e.g. [112].

For the case  $\omega \rightarrow \infty$  we need to look at the original equation (4.28) defining  $C_{rsi}$ . The scalar product between the spinors becomes independent of  $\mathbf{k}$  and therefore also independent of  $\omega$  for large  $\mathbf{k}$ , and we are left with a Fourier transform  $\tilde{F}(\omega)$  of some function, which we call  $F(t)$ . There is a general argument about the large- $\omega$  expansion of  $\tilde{F}(\omega)$ . By repeatedly applying partial integration,

$$\tilde{F}(\omega) = \int_{-\infty}^{\infty} dt F(t) e^{-i\omega t} = -\frac{i}{\omega} \int_{-\infty}^{\infty} dt F'(t) e^{-i\omega t} = -\frac{1}{\omega^2} \int_{-\infty}^{\infty} dt F''(t) e^{-i\omega t}, \quad (4.35)$$

we can generate ever more inverse powers of  $\omega$ . This only stops when  $F^{(n)}(t)$  is not differentiable anymore for some value  $n$ . For example, if  $F$  is four times continuously differentiable, then  $\tilde{F}(\omega) = c/\omega^4 + \mathcal{O}(\omega^{-5})$  with some constant  $c$ . In our case,  $A$  is infinitely often differentiable, which carries over to the Bogoliubov coefficients and the base spinors  $u_r(t, \mathbf{p})$ ,  $v_r(t, \mathbf{p})$ . Thus, our  $F$  is in  $C^\infty(\mathbb{R})^9$  which means  $\tilde{F}$  shrinks faster than *any* power of  $1/\omega$ , that is at least exponentially. As promised above, this also guarantees the integrability of the total energy in the large  $\omega$  regime.

By the same argument, one can show that  $C_{rsi}(\mathbf{p}, \mathbf{k})$  falls faster than any power of  $|\mathbf{p}|$ . (This behavior comes from the hidden factors  $\sim e^{ipt}$  in  $v_r$  and  $u_s$  in Eq. (4.28).) This guarantees the convergence of the momentum integral in Eq. (4.27), as long as the background field  $A$  is at least continuous. If we used, for example, two step functions for  $A$ , then  $C$  would only fall as fast as  $1/p$  and the whole integrand as  $1/p^2$ , which would be non-integrable

<sup>8</sup>Barring unexpected large  $\omega$  behavior. But without spoiling later results:  $f_\gamma$  behaves well in this other regime, so no further problems arise.

<sup>9</sup>The absolute value function in  $e^{-\varepsilon|t|}$  would obviously spoil this, but the precise form of the regulator function is not relevant, and we can replace it with a  $C^\infty$  variant for the purpose of this argument.



in the large- $p$  domain. In that case, one would have to use a regulator, most simply realized by just cutting of the momentum integration at some large value, see [50, 51]. A discontinuity is there physically motivated as an instantaneous mass shift, but in our case this would introduce delta-like spikes in the electric field, which are clearly unphysical. This is therefore not relevant for us and thus we do not need the momentum cutoff. Our fields will always make Eq. (4.27) integrable.

### 4.3 Application of the photon spectrum formula

#### 4.3.1 Numerics

The remarks we made about solving the QKE in section 2.4 still apply. Additional complexity comes from calculating the quantities  $C_{rsi}$  as a time integral over some function depending on the Bogoliubov coefficients and then doing the momentum integral over  $\mathbf{p}$ . The first one is straightforwardly achieved with the analytical split of the infinite time integration domain in Eq. (4.32). We do the remaining finite integral by “adjoining” the corresponding simple one-dimensional ODE to our already existing set of ODEs (2.21). This allows the solver to better control the steps it takes and increases both accuracy and speed compared to for example first computing the coefficients on some grid and then adding those terms up.

The momentum integral in (4.27) is three-dimensional and cannot be further reduced by symmetries. To compute it we use the Vegas algorithm from the Cuba library [113]. As its name suggests, it is a Monte Carlo algorithm, which will prove especially useful when using the periodic pulse as input. As a rule of thumb, the integrand in (4.27) will look similar to the corresponding pair spectrum. That is, smooth for the Sauter pulse, but exhibiting sharp ridges as in Fig. 2.4 for the periodic pulse. Integrating over such an intricate structure in three dimensions is only feasible with Monte Carlo methods. Still, the periodic pulse needs about an order of magnitude more points in the  $\mathbf{p}$  plane to achieve the same accuracy as the for Sauter pulse. Since the resulting spectrum in the  $\mathbf{k}$  plane is also much more intricate, one needs an order of magnitude more resolution in it. We thus need about 100 times as much time to produce a cut in the momentum plane, or a factor of 1000 for the entire plane. This is why we will mainly restrict us to the Sauter pulse for the numerics, with only a few results for the periodic pulse.

As a first example we will look at the photon spectrum generated by a single Sauter pulse as given by Eq. (2.40). Like for the pair spectrum, this runs into the slight problem of the Sauter pulse not having sharp a  $t_{\text{on}}$  and  $t_{\text{off}}$ . We solve it in the same way by varying them and verifying the result is independent of their precise value. This then yields asymptotic matching times which are “large enough” to give us the correct result.

#### 4.3.2 Numerical results

First we show a contour plot over the momentum plane for a single parameter point in Fig. 4.1. One can clearly see the infrared singularity as  $\omega \rightarrow 0$ . Furthermore the spectrum



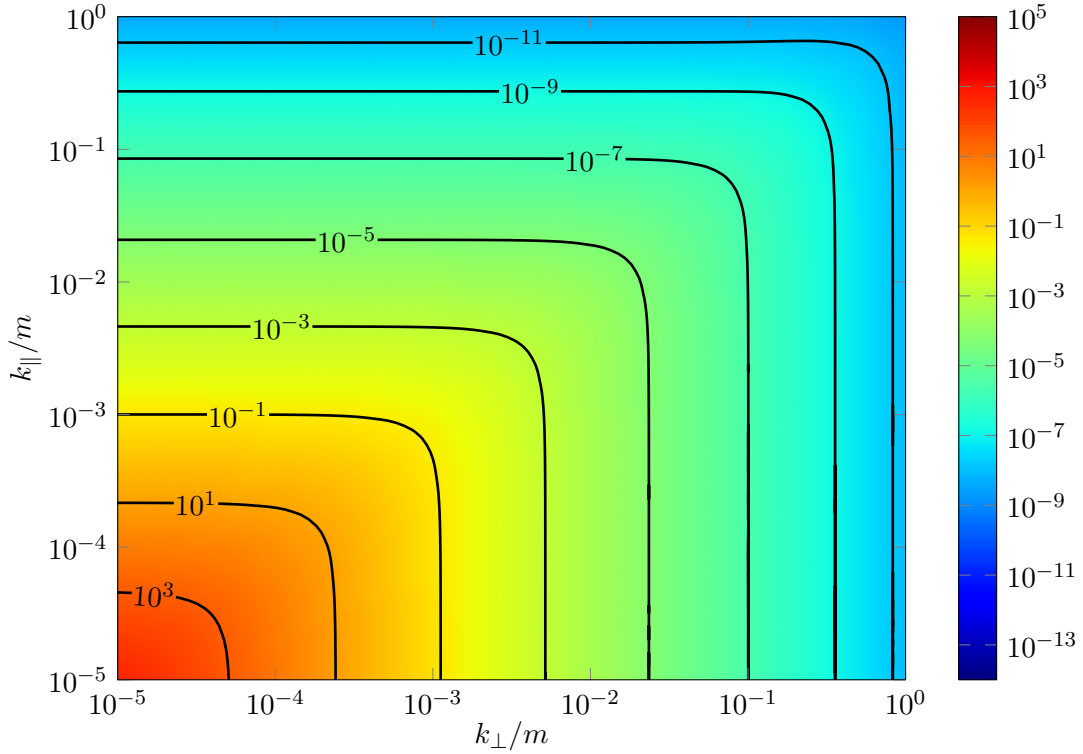


**Figure 4.1:** Contour plot of the residual photon phase-space distribution  $f_\gamma$  over the  $k_\parallel$ - $k_\perp$  plane for the Sauter pulse with  $E_0 = 0.2E_c$  and  $\tau = 2/m$ . The solid black curves are contour lines at integer powers of 10.

is rather smooth and isotropic, which carries over from the pair spectrum of the Sauter pulse. The anisotropy between  $k_\perp$  and  $k_\parallel$  increases for larger values of  $E_0$ . For smaller  $\omega$ , the contour lines are at an equal distance, indicating a polynomial dependence of  $f_\gamma$  on  $\omega$ . Farther out they are closer together. This is where our predicted small- $\omega$  asymptotics ( $\propto \omega^{-3}$ ) change over to the large- $\omega$  behavior (faster than any polynomial decline).

This can be more clearly seen in Fig. 4.2, where the blue curve depicts  $f_\gamma$ . In addition, we plot the different contributions to  $f_\gamma$  arising from the split (4.32). While there are two contributions to  $C_{rsi}$  – the integral over the intermediate time, when the electric field is turned on, and the asymptotic terms – there are three for the final photon spectrum, since it involves  $|C_{rsi}|^2$ : the squared modulus of the intermediate part is shown as the green curve, that of the asymptotic part as the cyan curve and the interference term between both as the red curve. The asymptotic term follows our predicted  $\omega^{-3}$  behavior for small values of  $\omega$ . Interestingly, even after it deviates from it for  $\omega > 1 \times 10^{-3}m$ , the full spectrum continues falling  $\propto \omega^{-3}$ . We ascribe this to the very large matching times  $t_{\text{on}}$  and  $t_{\text{off}}$  we used in the numerics, which essentially shifts some part of the asymptotics into the intermediate terms. The intermediate and mixed contributions, on the other hand, only diverge as  $\omega^{-1}$ . This is obvious for the former, while for the latter one would expect  $\omega^{-2}$ , but the interference of the complex terms actually cancels that out.

As for the large- $\omega$  behavior, the individual terms continue falling with some power of  $\omega$ , since they are defined by cut off integrals, which are in effect Fourier transforms of discontinuous functions (see our discussion of this in section 4.2.2). However, coherently

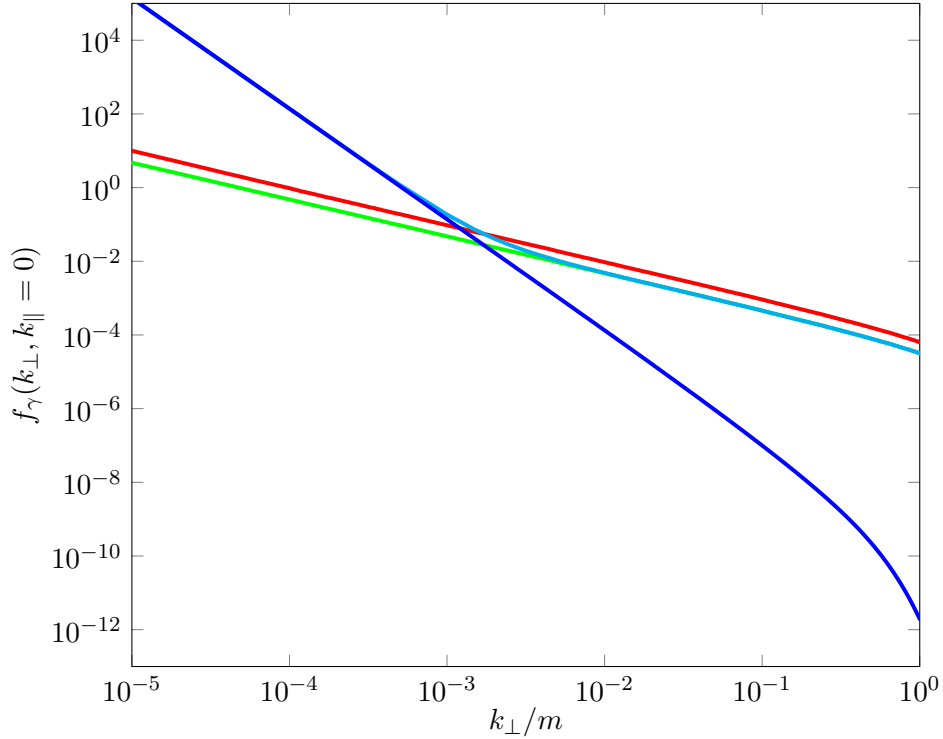


**Figure 4.2:** Plot of the residual photon phase-space distribution  $f_\gamma$  as a function of  $k_\perp$  at  $k_\parallel = 0$  for the Sauter pulse with  $E_0 = 0.2E_c$  and  $\tau = 2/m$ . The blue curve is the full result. The green curve depicts the contribution from the intermediate integral, the cyan curve from the asymptotic terms and the red curve from the mixed terms.

adding them up cancels out almost everything and lets  $f_\gamma$  fall faster than every power of  $\omega$ . The numerical investigation actually yields exponential behavior, i.e.  $f_\gamma \propto e^{-\omega/m}$  as  $\omega \rightarrow \infty$ .

Separating the contributions does thus not provide a clear signal of the intermediate large particle yield, as we hoped. This should manifest as the intermediate contribution dominating the total spectrum in some region of the momentum space, but instead we see it is dominated by the asymptotic terms for  $\omega \rightarrow 0$ . For  $\omega \rightarrow \infty$  the intermediate and asymptotic terms are of almost the same magnitude, with their exponentially shrinking difference accounting for the spectrum. Between these two regimes, the intermediate contribution is always smaller than the asymptotic one and also produces no distinguishable features in the spectrum. This leads to the conclusion that the intermediate quasi-particles are indeed non-physical, since their large occupancy leaves no trace in the photon spectrum.

Figure 4.3 shows the ratio of the photon to pair numbers at a fixed momentum as a contour plot over the parameter space. For the photons, we chose the momentum  $k_\perp = 10^{-4}m$ ,  $k_\parallel = 0$  and for the pairs  $\mathbf{p} = 0$  (which is where  $f$  has its maximum for the Sauter pulse). The number of photons is much greater than the number of pairs, even at readily observable energies in the optical range like our chosen  $\omega = 10^{-4}m$ . This could be a viable path for detecting the dynamical Schwinger effect even when the residual pair density is too low for detection. The ratio gets larger for smaller  $\omega$ , but then one runs into the problem of detecting very low frequency photons, which ties in with the treatment of the infrared

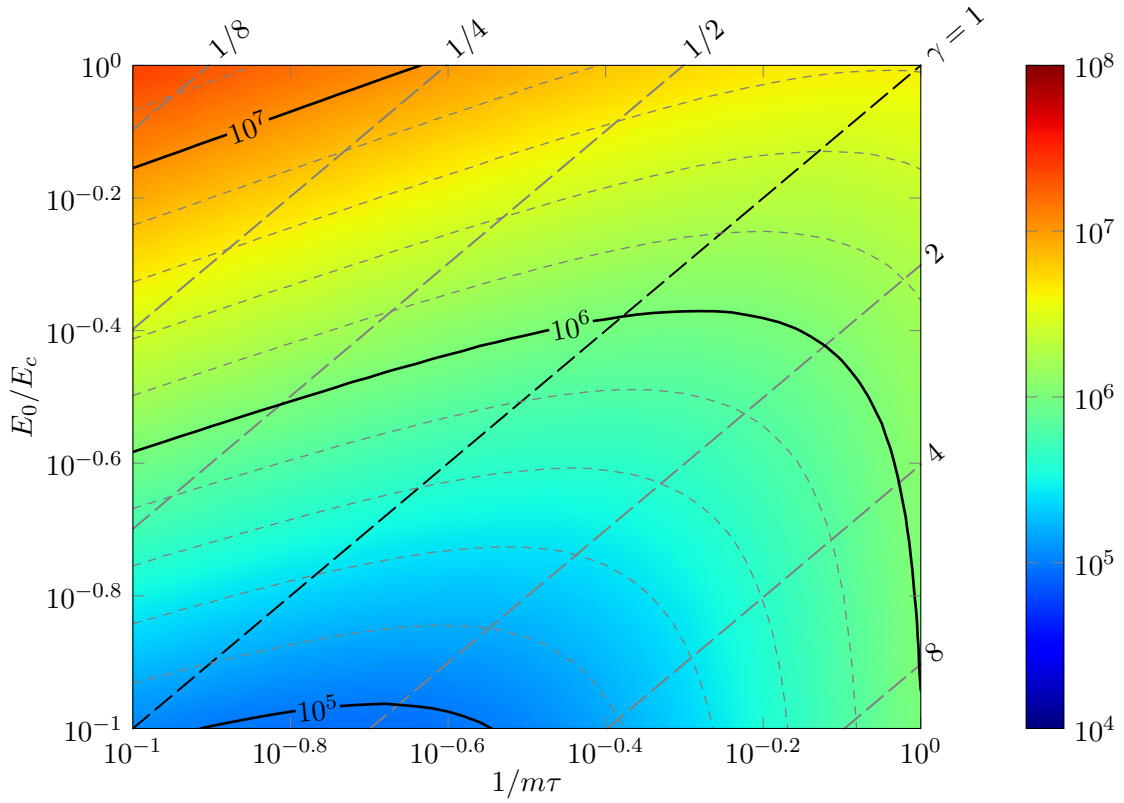


**Figure 4.3:** Contour plot of  $f_\gamma(k_\perp = 10^{-4}m, k_\parallel = 0)/f(\mathbf{p} = 0)$ , i.e. the ratio of the photon and pair spectrum at two points in phase space for the Sauter pulse, over the parameter space. The solid black curves are contour lines at integer powers of 10, the gray short dashed curves at  $10^{0.2}, \dots, 10^{0.8}$  between them. The long dashed lines are the loci of constant Keldysh parameter  $\gamma$ .

divergence. Also note there is no obvious simple dependence of  $f_\gamma$  on  $f$  with their ratio varying over orders of magnitude. If, for example, one imagined a scenario where the residual pair density appeared fully formed and then the electrons and positrons started annihilating with some momentum dependent cross section, the resulting photon spectrum should not explicitly depend on  $E_0$  and  $\tau$  but only implicitly through its linear dependence on  $f$ . Since  $f(\mathbf{p} = 0)$  is a good indicator of the overall pair spectrum, the depicted ratio should not vary as much as it does. This implies that intermediate quantum effects play a severe role, and a semi-classical approach is inadequate for explaining what is going on.

Since we have to rely on the numerical solutions to generate this plot, we can only take the parameters as low as  $E_0 = 0.1E_c$  and  $\tau = 10/m$ , in contrast to e.g. Fig. 2.15. Nonetheless the smooth pattern allows us to extrapolate to the rest of the parameter plane. In particular, for  $\gamma \ll 1$ , we have the apparent relation  $\ln f_\gamma = a \ln E_0/E_c + b \ln m\tau + c$  (as can be seen from the straight contour lines in this region).

Finally we look at the photon signature of the dynamically assisted Schwinger effect. We will use again our familiar setup: The superposition of two Sauter pulses as given by Eq. (3.1) and that of two periodic pulses from Eq. (3.3). The resulting spectra are plotted in Fig. 4.4. We see the same pattern of orders of magnitude enhancement from the second field (red curves) compared to the first field alone (blue curves). This is especially true at

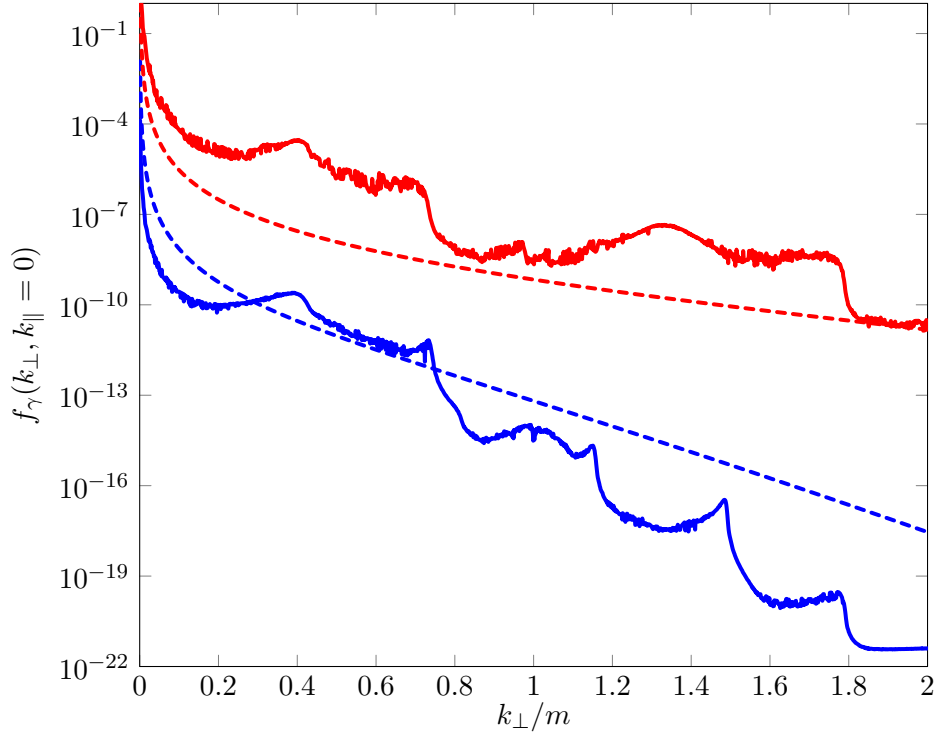


**Figure 4.4:** Plot of the photon spectrum over  $k_{\perp}$  at  $k_{\parallel} = 0$  for the superposition of two Sauter pulses (dashed curves) and two periodic pulses (solid curves). Parameters:  $E_1 = 0.1E_c$ ,  $\nu_1 = 0.5m$ ,  $\nu_2 = 2m$  and  $E_2 = 0$  (blue),  $E_2 = 0.05E_c$  (red). Additionally for the periodic pulse  $t_{\text{flat}} = 50T$  and  $t_{\text{ramp}} = 5T$ .

larger values of  $\omega$  with the second field apparently making the coefficient of the exponential decay smaller. The spectra for the Sauter pulse (dashed curves) show the smooth behavior we saw above in Fig. 4.2. In contrast for the periodic pulse, we see remnants of the ridge structures from the pair spectrum, see e.g. Fig. 3.5, although the peaks are not as pronounced. The location of the peaks follows no easily discernible pattern, in particular, they seem to have no relation to the base frequency  $\nu_1$ . The greater numerical difficulties that we mentioned for the periodic pulse can be seen in the bigger numerical noise in the solid curves. We are nonetheless confident in these numerical results as they are consistent with those for the Sauter pulse and earlier calculations and were cross-checked with different algorithms and meta parameters like cutoff for the numerical integration and desired accuracies for the solution of the ODEs.

## 4.4 Summary

In this chapter, we coupled the fermion dynamics that is driven by a background field to a quantized photon field. We motivated the correct normal order to be used for the current that arises from the pair density. That current has a vacuum expectation value causing a classical backreaction to the background field which must be renormalized. This lead to modified equations for the Bogoliubov coefficients with which we calculated the photon spectrum that the quantum part of the current sources. The resulting spectrum showed a typical QED infrared divergence which, however, can be dealt with in the standard way. In

the ultraviolet, the photon yield drops exponentially for well behaved external fields. We identified terms that arise from an intermediate time integration, where the external field is switched on and the quasi-particle density is high, and asymptotic terms, which only depend on the final pair spectrum. Despite this split, we found no evidence the quasi-particles leave a clear signal in the photon spectrum, which confirms the standard QFT interpretation that only final states have physical meaning. But that also diminishes the prospect of detecting the dynamical Schwinger effect through a signature of the large intermediate pair density. In comparing the photon to the pair spectrum, we saw the former does not depend in a simple way on the latter. In particular, a model where quasi-particles and antiparticles annihilate in a semiclassical manner is inadequate in explaining the photon spectrum. The Sauter pulse leads to a smooth photon spectrum, while the periodic pulse produced a peak structure, which resembles their respective pair spectra, although the correspondence is not one to one. Exploring the superposition of pulses with different parameters, we found an enhancement effect similar to the dynamically assisted Schwinger effect from chapter 3: the second field increases the photon yield by orders of magnitude.



## 5 Conclusion and outlook

In this thesis, we investigated the dynamical and dynamically assisted Schwinger effect. Our main tool was the quantum kinetic equation which we derived from diagonalizing the time dependent QED Hamiltonian via a Bogoliubov transform. We saw that taking the background electric field to be periodic produces shell structures in the phase space of produced pairs. This is in contrast to the smooth spectrum resulting from the Sauter pulse. We found analytical expressions well approximating this spectrum, in particular the position, height and width of the shells. Most information about them is encoded in the zeros of the quasi-energy  $\Omega$  in the complex time domain. As we restricted us to spatially homogeneous fields that were nonetheless intended to serve as a model for colliding laser pulses, one avenue for future work would be loosening that restriction by employing more realistic background fields and extending these results. We expect no qualitatively new behavior would occur for oscillating fields, but the analysis would likely be much more involved, since an inhomogeneous electro-magnetic field implies one has to deal with the full Dirac equation, which is a partial differential equation in contrast to the ordinary differential QKE. The groundwork for such a treatment was laid in appendix C.

For the dynamically assisted Schwinger effect we confirmed earlier results by other authors, who used a superposition of Sauter pulses, for periodic pulses. We found parameter sets for which the pair yield can be increased by 3–4 orders of magnitude. We gave an explanation for that in terms of the already mentioned zeros of  $\Omega$ . The further the main zero moves towards the real axis upon increasing the field strength of the second field, the larger the pair yield of the combined fields will be. The distance to the real axis enters in the exponential function, explaining why already a small field strength has orders-of-magnitude effects. Besides the generalization for the single field case, an obvious open question is whether the superposition of three fields can further increase the particle production. This line of investigation was already started in [85].

Despite the enhancement in the dynamically assisted Schwinger effect, we still need unrealistically high field strengths or frequencies to reach a measurable residual pair yield. Since the intermediate quasi-particle number is much larger than the residual, we wondered whether these quasi-particles can produce photons when we couple our system to a quantized radiation field. This proved to be true, but unfortunately no clear signal emerged which could serve as a verification of the dynamical Schwinger effect for pairs at intermediate times. Nonetheless the photon numbers are much greater than the pair numbers, thus potentially more easily observed, and we could also show an analog to the dynamically assisted Schwinger effect. Further research could focus on different secondary probes that could exploit the quasi-particle numbers. Also, in our analysis we neglected the backreaction, which should not change the result in the sub-critical regime, but could lead to interesting new phenomena otherwise, when properly incorporated.





## A A toy model for particle creation

We are going to explore the core concepts and techniques that come into play in the main text by investigating a toy model. Despite its simplicity, it exhibits many of the important characteristics of the more involved field theoretical model. Our notation will be similar to that employed for Dirac spinors, for example we write  $u, v$  for our base vectors to connect to the standard notation  $u_r(\mathbf{p}), v_r(\mathbf{p})$ .

We employ a variant of the ubiquitous two-level system, that is our Hilbert space is two dimensional,  $\mathcal{H} = \mathbb{C}^2$ , and we choose our first-quantized Hamiltonian as

$$h(t) = E \begin{pmatrix} \cos 2\varphi(t) & \sin 2\varphi(t) \\ \sin 2\varphi(t) & -\cos 2\varphi(t) \end{pmatrix}, \quad \varphi(t) = \begin{cases} 0, & t < 0 \\ \omega t, & 0 \leq t \leq \tau \\ \omega\tau, & \tau < t \end{cases}. \quad (\text{A.1})$$

Our Hamiltonian is constant for  $t < 0$  and  $t > \tau$ . We call  $h(t < 0)$  the free Hamiltonian. If  $\tau = n\pi/\omega$ ,  $n \in \mathbb{N}$  we even have  $h(t > \tau) = h(t < 0)$ , that is  $h$  returns to its free form. The eigenvalues of  $h(t)$  are  $+E, -E$  and are constant. The corresponding eigenvectors are

$$U(t) = \begin{pmatrix} \cos \varphi(t) \\ \sin \varphi(t) \end{pmatrix}, \quad V(t) = \begin{pmatrix} -\sin \varphi(t) \\ \cos \varphi(t) \end{pmatrix}, \quad (\text{A.2})$$

$$h(t)U(t) = EU(t), \quad h(t)V(t) = -EV(t),$$

and they form a basis of  $\mathcal{H}$  for all  $t$ . Another distinguished base is formed by solutions to Schrödinger's equation with specific initial conditions, that is we demand

$$i\partial_t u(t) = h(t)u(t), \quad i\partial_t v(t) = h(t)v(t), \quad (\text{A.3})$$

$$u(0) = U(0) = \begin{pmatrix} 1 \\ 0 \end{pmatrix}, \quad v(0) = V(0) = \begin{pmatrix} 0 \\ 1 \end{pmatrix}.$$

The transformation between these two bases must necessarily be unitary and is thus parametrized by two complex numbers,  $\alpha$  and  $\beta$ , with  $|\alpha|^2 + |\beta|^2 = 1$ . It reads

$$u(t) = \alpha(t)U(t) + \beta(t)V(t), \quad (\text{A.4})$$

$$v(t) = -\beta^*(t)U(t) + \alpha^*(t)V(t).$$

This is called the Bogoliubov transformation, and  $\alpha$  and  $\beta$  the Bogoliubov coefficients. Instead of solving the Schrödinger equation, we instead derive an equation for these coefficients, since it will be easier to solve and to connect to observables. Inserting one equation of (A.4) (both lead to the same set of equations) into (A.3) and using (A.2) we find

$$\partial_t \begin{pmatrix} \alpha(t) \\ \beta(t) \end{pmatrix} = \begin{pmatrix} -iE & 0 \\ 0 & iE \end{pmatrix} \begin{pmatrix} \alpha(t) \\ \beta(t) \end{pmatrix}, \quad t < 0, t > \tau,$$

$$\partial_t \begin{pmatrix} \alpha(t) \\ \beta(t) \end{pmatrix} = \begin{pmatrix} -iE & \omega \\ -\omega & iE \end{pmatrix} \begin{pmatrix} \alpha(t) \\ \beta(t) \end{pmatrix}, \quad 0 \leq t \leq \tau, \quad (\text{A.5})$$

$$\alpha(0) = 1, \quad \beta(0) = 0.$$

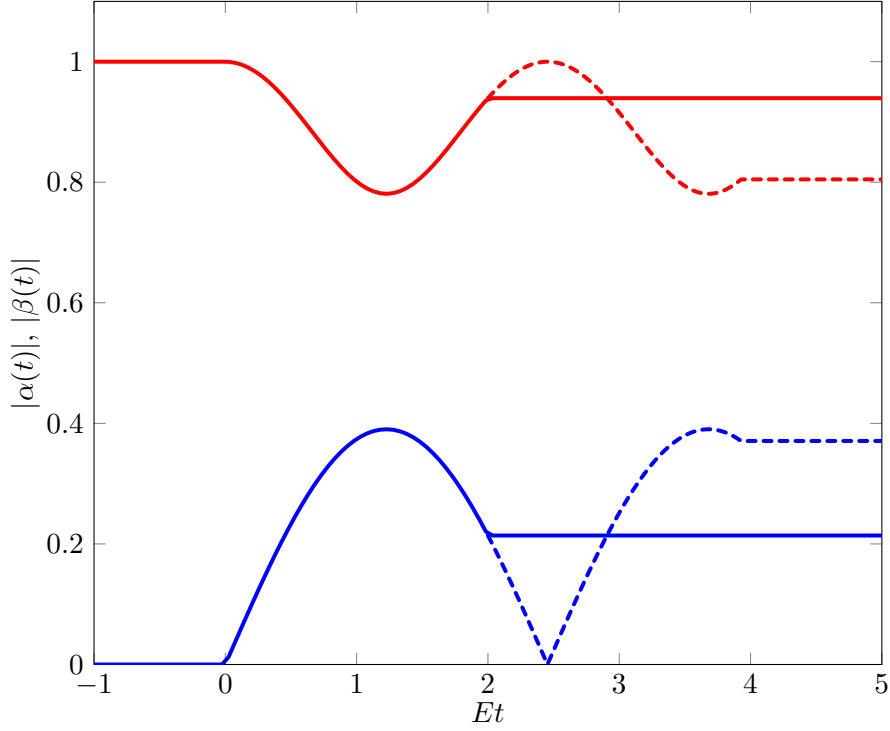


**Figure A.1:** Plot of the modulus of  $\alpha(t)$  (red) and  $\beta(t)$  (blue) given by (A.6) as a function of time. Parameters are  $\omega = 0.8E$  and  $\tau = 2/E$  (solid) as well as  $\tau = \pi/\omega = 5\pi/4E$  (dashed).

The time evolution is trivial for  $t < 0$  and  $t > \tau$ , when our Hamiltonian is constant. We can easily solve this set of coupled equations, resulting in

$$\alpha(t) = \begin{cases} e^{-iEt}, & t < 0 \\ \cos \Omega t - i \frac{E}{\Omega} \sin \Omega t, & 0 \leq t \leq \tau, \\ \left( \cos \Omega \tau - i \frac{E}{\Omega} \sin \Omega \tau \right) e^{-iE(t-\tau)}, & \tau < t \end{cases} \quad (\text{A.6})$$

$$\beta(t) = \begin{cases} 0, & t < 0 \\ -\frac{\omega}{\Omega} \sin \Omega t, & 0 \leq t \leq \tau, \\ -\frac{\omega}{\Omega} \sin \Omega \tau e^{iE(t-\tau)}, & \tau < t \end{cases}$$

$$\Omega = \sqrt{E^2 + \omega^2}.$$

A plot of these solutions is shown in Fig. A.1. Note that, although  $h(t > \tau)$  is the free Hamiltonian for the dashed lines where  $\tau = \pi/\omega$ , the system does not return to  $|\alpha(t > \tau)| = 1$ ,  $|\beta(t > \tau)| = 0$ , the initial state. It is indeed farther away from the initial state than the solid line, for which the Hamiltonian does not return to be free. If we wanted to reach the initial state, we would need to set  $\tau$  to for example  $\tau = \pi/\Omega = 5\pi/\sqrt{41}E$ , but then the Hamiltonian would not be free.

To study particle creation, we need to second-quantize the system. We do this in the standard way: Write a general solution  $\psi(t)$  of Schrödinger's equation in terms of  $u(t)$  and  $v(t)$ , and promote the coefficients to creation/annihilation operators with Fermi-Dirac statistics, that is

$$\psi(t) = c u(t) + d^\dagger v(t), \quad \{c, c^\dagger\} = \{d, d^\dagger\} = 1, \quad (\text{A.7})$$

with all other anticommutators zero. The vacuum is defined by  $c|0\rangle = d|0\rangle = 0$ . The Fock space thus created is very simple,  $\mathcal{F}(\mathcal{H}) = \mathbb{C}^4$  with base vectors  $|0\rangle$ ,  $c^\dagger|0\rangle$ ,  $d^\dagger|0\rangle$  and  $c^\dagger d^\dagger|0\rangle$ . The second-quantized Hamiltonian is then  $H(t) = \psi^\dagger(t)h(t)\psi(t)$ . The value of the Bogoliubov transform can now be seen by noting that the operator  $\psi$  may as well be expanded in the base  $U, V$ :  $\psi(t) = C(t)U(t) + D^\dagger(t)V(t)$ . Since both representations must be equal, the Bogoliubov transform from  $U, V$  to  $u, v$  implies one from  $c, d^\dagger$  to  $C, D^\dagger$ :

$$\begin{aligned} C(t) &= \alpha(t)c - \beta^*(t)d^\dagger, \\ D^\dagger(t) &= \beta(t)c + \alpha^*(t)d^\dagger. \end{aligned} \tag{A.8}$$

Crucially, this transform diagonalizes the Hamiltonian:

$$H(t) = E \left( C^\dagger(t)C(t) - D(t)D^\dagger(t) \right). \tag{A.9}$$

On the other hand, expanding in the operators  $c$  and  $d$ , it contains off-diagonal terms. One can easily verify that  $C$  and  $D$  obey the same canonical anticommutation relations as  $c$  and  $d$ . Thus they are creation/annihilation operators for some quasi particles. These quasi-particles can only be interpreted as real ones for  $t < 0$  or  $t > \tau$ , when the first-quantized Hamiltonian is constant. The vacuum corresponding to  $C$  and  $D$  will be different from  $|0\rangle$  and time dependent. We will call it  $|\Omega(t)\rangle$ . It is defined by  $C(t)|\Omega(t)\rangle = D(t)|\Omega(t)\rangle = 0$ . By inserting  $C$  and  $D$  from Eq. (A.8) one can check that

$$|\Omega(t)\rangle = (\alpha(t) + \beta^*(t)c^\dagger d^\dagger)|0\rangle \tag{A.10}$$

up to an irrelevant phase. The vacuum persistence amplitude is the overlap between the two vacua and with the above we easily find  $\langle\Omega(t)|0\rangle = \alpha^*(t)$ .

How can we now define the particle number? There are two obvious ways: How many quasi-particles does the vacuum contain, and how many particles does the time dependent vacuum contain? Luckily, both questions yield the same answer, and since our toy model was chosen so simple, the answer is also the same for particles and anti-particles:

$$\begin{aligned} \langle 0|C^\dagger(t)C(t)|0\rangle &= \langle\Omega(t)|c^\dagger c|\Omega(t)\rangle = |\beta(t)|^2, \\ \langle 0|D^\dagger(t)D(t)|0\rangle &= \langle\Omega(t)|d^\dagger d|\Omega(t)\rangle = |\beta(t)|^2. \end{aligned} \tag{A.11}$$

Comparing again with Fig. A.1, we see that the particle number is just the square of the function plotted in blue. In particular, even if the first-quantized Hamiltonian returns to its initial (free) state, a residual particle number will still remain. Also, the second-quantized Hamiltonian will not return to be free.

We end this exposition with a brief remark about normal ordering, which is useful to motivate our reasoning about the correct current to use for coupling to a radiation field in chapter 4. For an operator  $A$ , let  $:A:$  denote the standard normal ordering w.r.t.  $c$  and  $d$ : Move all  $c$  ( $d$ ) to the right of all  $c^\dagger$  ( $d^\dagger$ ), changing sign with every swap to respect the fermionic statistics. It is clear, that the expectation value of the ground state energy computed with this normal ordering is  $\langle E \rangle(t) = \langle 0|:H(t):|0\rangle = 0$ . Intuitively however, we would expect a non-zero value, since the creation of particles should add energy to the system. Computing without any normal ordering we get  $\langle E \rangle(t) = \langle 0|H(t)|0\rangle = E(1 - 2|\beta(t)|^2)$ . This is better, but for  $t = 0$  we get  $\langle E \rangle(0) = E$  where we would expect zero, since without particles the system contains no energy. Also in field theory, this term would become the well known infinite vacuum energy, which we need to subtract.

The correct way is consequently to normal order w.r.t. the operators  $C$  and  $D$ . We will denote this prescription by  $\bullet A \bullet$ . The normal ordered Hamiltonian is then  $\bullet H(t) \bullet = E \left( C^\dagger(t)C(t) + D^\dagger(t)D(t) \right)$  and  $\langle E \rangle(t) = \langle 0 | \bullet H(t) \bullet | 0 \rangle = 2E|\beta(t)|^2$ . This corrects the deficiencies of both previous attempts. It is also the result one would have guessed: energy per particle times number of particles times two (for particle + anti-particle). We conclude that the correct way to compute expectation values is to normal order the operator corresponding to the observable according to the prescription  $\bullet \dots \bullet$ .

## B Some mathematical remarks about the quantum kinetic equation

### B.1 Properties of the base spinors

The aim of this section is to show that Eqs. (2.15), (2.16) and (2.17) hold. First, we note the explicit form of the two eigenspinors to  $\gamma^0\gamma^3$  with eigenvalue  $-1$ ,  $R_1$  and  $R_2$ :

$$\gamma^0\gamma^3 = \begin{pmatrix} -\sigma_3 & 0 \\ 0 & \sigma_3 \end{pmatrix} = \begin{pmatrix} -1 & 0 & 0 & 0 \\ 0 & 1 & 0 & 0 \\ 0 & 0 & 1 & 0 \\ 0 & 0 & 0 & -1 \end{pmatrix}, \quad R_1 = \begin{pmatrix} 1 \\ 0 \\ 0 \\ 0 \end{pmatrix}, \quad R_2 = \begin{pmatrix} 0 \\ 0 \\ 0 \\ 1 \end{pmatrix}. \quad (\text{B.1})$$

Next, from the explicit form of the first-quantized Hamiltonian (2.10), it is easy to show that

$$h(\mathbf{p})^2 = \Omega(\mathbf{p})^2, \quad (\text{B.2})$$

$$R_r^\dagger h(\mathbf{p}) R_s = -p_z \delta_{rs}. \quad (\text{B.3})$$

The equations (B.2) and (B.3) are used to check the orthogonality, taking  $u$  and  $v$  from (2.14). First for  $u_r^\dagger u_s$  (which works the same for  $v_r^\dagger v_s$ ):

$$u_r(\mathbf{p})^\dagger u_s(\mathbf{p}) = \frac{R_r^\dagger [\Omega(\mathbf{p}) + h(\mathbf{p})]^2 R_s}{2\Omega(\mathbf{p})(\Omega(\mathbf{p}) - p_z)} = \frac{R_r^\dagger [2\Omega^2 + 2\Omega h] R_s}{2\Omega(\Omega - p_z)} = \frac{R_r^\dagger [\Omega + h] R_s}{\Omega - p_z} = \delta_{rs}. \quad (\text{B.4})$$

For  $u_r^\dagger v_s$  (same for  $v_r^\dagger u_s$ ):

$$u_r(\mathbf{p})^\dagger v_s(-\mathbf{p}) = \frac{R_r^\dagger [\Omega(\mathbf{p}) + h(\mathbf{p})] [-\Omega(\mathbf{p}) + h(\mathbf{p})] R_s}{2\Omega(\mathbf{p})\sqrt{\Omega(\mathbf{p})^2 - p_z^2}} = \frac{R_r^\dagger [-\Omega^2 + h^2] R_s}{2\Omega\sqrt{\Omega^2 - p_z^2}} = 0. \quad (\text{B.5})$$

This proves Eq. (2.15).

We can similarly show that  $u_r$  and  $v_r$  are eigenvectors of  $h$ ,

$$h(\mathbf{p})u_r(\mathbf{p}) = h \frac{\Omega + h}{\sqrt{2\Omega(\Omega - p_z)}} R_r = \frac{\Omega h + \Omega^2}{\sqrt{2\Omega(\Omega - p_z)}} R_r = \Omega(\mathbf{p})u_r(\mathbf{p}), \quad (\text{B.6})$$

$$h(\mathbf{p})v_r(-\mathbf{p}) = h \frac{-\Omega + h}{\sqrt{2\Omega(\Omega + p_z)}} R_r = \frac{-\Omega h + \Omega^2}{\sqrt{2\Omega(\Omega + p_z)}} R_r = -\Omega(\mathbf{p})v_r(\mathbf{p}) \quad (\text{B.7})$$

which proves Eq. (2.16).

For the last property first observe

$$\frac{d}{dt}u_r(\mathbf{P}(t)) = eE(t)\frac{\partial}{\partial P_{\parallel}(t)}u_r(\mathbf{P}(t)) = eE(t)\left.\frac{\partial}{\partial p_z}\right|_{\mathbf{p}=\mathbf{P}(t)}u_r(\mathbf{p}). \quad (\text{B.8})$$

To carry out the partial derivative we first calculate it for the denominator

$$\begin{aligned} \frac{\partial}{\partial p_z}\frac{1}{\sqrt{2\Omega(\mathbf{p})(\Omega(\mathbf{p})-p_z)}} &= \frac{-1}{\sqrt{2\Omega(\Omega-p_z)^3}}\left[\frac{p_z}{\Omega}(\Omega-p_z)+\Omega\left(\frac{p_z}{\Omega}-1\right)\right] \\ &= \frac{1}{2\Omega^2}\sqrt{\frac{\Omega-p_z}{2\Omega}} \end{aligned} \quad (\text{B.9})$$

and the remaining terms

$$\frac{\partial}{\partial p_z}(\Omega(\mathbf{p})+h(\mathbf{p}))R_r = \left(\frac{p_z}{\Omega}+\gamma^0\gamma^3\right)R_r = -\frac{\Omega-p_z}{\Omega}R_r. \quad (\text{B.10})$$

Adding both up using the product rule we get

$$\begin{aligned} \frac{\partial}{\partial p_z}u_r(\mathbf{p}) &= \frac{\partial}{\partial p_z}\frac{\Omega+h}{\sqrt{2\Omega(\Omega-p_z)}}R_r = \sqrt{\frac{\Omega-p_z}{2\Omega}}\left[\frac{\Omega+h}{2\Omega^2}-\frac{1}{\Omega}\right]R_r \\ &= \frac{1}{2\Omega^2}\sqrt{\Omega^2-p_z^2}\frac{-\Omega+h}{\sqrt{2\Omega(\Omega+p_z)}}R_r = \frac{\epsilon_{\perp}}{2\Omega^2}v_r(-\mathbf{p}). \end{aligned} \quad (\text{B.11})$$

This together with Eq. (B.8) yields

$$\frac{d}{dt}u_r(\mathbf{P}(t)) = \frac{eE(t)\epsilon_{\perp}}{2\Omega(\mathbf{P}(t))}v_r(-\mathbf{P}(t)). \quad (\text{B.12})$$

Together with a similar calculation for  $v_r(-\mathbf{P}(t))$  this proves Eq. (2.17).

## B.2 Lifting the quantum kinetic equation to the Lie algebra

Both the equation for the Bogoliubov coefficients (2.21) and the QKE (2.29) derived from it can be cast into matrix form which enables further analysis. We define two matrix differential equations

$$\begin{aligned} \dot{U} &= MU, & \dot{O} &= NO, \\ U, M &\in \mathbb{C}^2, & O, N &\in \mathbb{R}^3, \\ M &= \begin{pmatrix} -i\Omega & \frac{Q}{2} \\ -\frac{Q}{2} & i\Omega \end{pmatrix}, & N &= \begin{pmatrix} 0 & -Q & 0 \\ Q & 0 & -2\Omega \\ 0 & 2\Omega & 0 \end{pmatrix}, \\ U(t_{\text{on}}) &= \mathbb{1}, & O(t_{\text{on}}) &= \mathbb{1}. \end{aligned} \quad (\text{B.13})$$

Then, by setting

$$\begin{pmatrix} \alpha \\ \beta \end{pmatrix} = U \begin{pmatrix} 1 \\ 0 \end{pmatrix} \quad \begin{pmatrix} 1-f \\ u \\ v \end{pmatrix} = O \begin{pmatrix} 1 \\ 0 \\ 0 \end{pmatrix}, \quad (\text{B.14})$$

$\alpha, \beta$  fulfill Eq. (2.21) and  $f, u, v$  Eq. (2.29). Since  $M$  is skew-Hermitian,  $M^\dagger = -M$ ,  $U$  must be unitary,  $U^\dagger U = \mathbb{1}$ , and similarly, since  $O$  is skew-symmetric,  $N^T = -N$ ,  $O$  must be orthogonal,  $O^T O = \mathbb{1}$ . Furthermore,  $\det U = 1$  because  $\text{tr } M = 0$  and  $\det O = 1$  because  $\det O(t_{\text{on}}) = \det \mathbb{1} = 1$  and  $\det O$  is constant.

The deeper reason for such a behavior is because the skew-Hermitian matrices of trace zero,  $\mathfrak{su}(2)$ , form the Lie algebra of the Lie group  $SU(2)$ , the unitary matrices of determinant one (both in two dimensions). Similarly, the skew-symmetric matrices (which must necessarily be traceless),  $\mathfrak{so}(3)$ , form the Lie algebra to the Lie group  $O(3)$ , the orthogonal matrices (both in three dimensions). The group  $O(3)$  has two connected components, one where  $\det O = -1$ , and one where  $\det O = 1$  which is a Lie group of its own called  $SO(3)$ . The initial condition makes our  $O$  belong to  $SO(3)$ .

Both mentioned Lie algebras each have three generators. Let  $S_i$  generate  $\mathfrak{su}(2)$  and  $T_i$   $\mathfrak{so}(3)$ . One can use different representations of those generators; we fix

$$\begin{aligned} S_1 &= \frac{1}{2} \begin{pmatrix} 0 & i \\ i & 0 \end{pmatrix}, & S_2 &= \frac{1}{2} \begin{pmatrix} 0 & 1 \\ -1 & 0 \end{pmatrix}, & S_3 &= \frac{1}{2} \begin{pmatrix} -i & 0 \\ 0 & i \end{pmatrix}, \\ T_1 &= \begin{pmatrix} 0 & 0 & 1 \\ 0 & 0 & 0 \\ -1 & 0 & 0 \end{pmatrix}, & T_2 &= \begin{pmatrix} 0 & 0 & 1 \\ -1 & 0 & 0 \\ 0 & 0 & 0 \end{pmatrix}, & T_3 &= \begin{pmatrix} 0 & 0 & 0 \\ 0 & 0 & -1 \\ 0 & 1 & 0 \end{pmatrix}. \end{aligned} \quad (\text{B.15})$$

The generators fulfill  $[S_i, S_j] = \sum_k \epsilon_{ijk} S_k$  and  $[T_i, T_j] = \sum_k \epsilon_{ijk} T_k$ , so both Lie algebras are isomorphic. We group the generators into symbolic 3-vectors,  $\mathbf{S}$  and  $\mathbf{T}$ , which together with the 3-vector  $\mathbf{J}$  defined below allow a compact notation for  $M$  and  $N$ :

$$\begin{aligned} M &= \mathbf{J} \cdot \mathbf{S} = QS_2 + 2\Omega S_3 = \begin{pmatrix} -i\Omega & \frac{Q}{2} \\ -\frac{Q}{2} & i\Omega \end{pmatrix}, \\ N &= \mathbf{J} \cdot \mathbf{T} = QT_2 + 2\Omega T_3 = \begin{pmatrix} 0 & -Q & 0 \\ Q & 0 & -2\Omega \\ 0 & 2\Omega & 0 \end{pmatrix}, \\ \mathbf{J} &= \begin{pmatrix} 0 \\ Q \\ 2\Omega \end{pmatrix}. \end{aligned} \quad (\text{B.16})$$

Any solution  $U$  and  $O$  can be written as the exponential of some Lie algebra element. Let that be parametrized by a vector  $\boldsymbol{\theta}$ , then  $U = \exp(\boldsymbol{\theta} \cdot \mathbf{S})$  and  $O = \exp(\boldsymbol{\theta} \cdot \mathbf{T})$ . In general, if  $X(t)$  is some time-dependent matrix, then one can show

$$\frac{d}{dt} e^{X(t)} = \sum_n \frac{[X(t), \dot{X}(t)]_n}{(n+1)!} e^{X(t)}, \quad (\text{B.17})$$

where  $[\dots, \dots]_n$  is the  $n$ -times iterated commutator. For our (isomorphic) Lie algebras  $[\mathbf{a} \cdot \mathbf{S}, \mathbf{b} \cdot \mathbf{S}] = (\mathbf{a} \times \mathbf{b}) \cdot \mathbf{S}$  and therefore

$$\begin{aligned} [\boldsymbol{\theta} \cdot \mathbf{S}, \dot{\boldsymbol{\theta}} \cdot \mathbf{S}]_0 &= \dot{\boldsymbol{\theta}} \cdot \mathbf{S}, \\ [\boldsymbol{\theta} \cdot \mathbf{S}, \dot{\boldsymbol{\theta}} \cdot \mathbf{S}]_{2n+1} &= (-1)^n \theta^{2n} (\boldsymbol{\theta} \times \dot{\boldsymbol{\theta}}) \cdot \mathbf{S}, \\ [\boldsymbol{\theta} \cdot \mathbf{S}, \dot{\boldsymbol{\theta}} \cdot \mathbf{S}]_{2n+2} &= (-1)^n \theta^{2n} (\boldsymbol{\theta} \times (\boldsymbol{\theta} \times \dot{\boldsymbol{\theta}})) \cdot \mathbf{S}. \end{aligned} \quad (\text{B.18})$$

This allows summing the series in Eq. (B.17) for  $X = \boldsymbol{\theta} \cdot \mathbf{S}$ :

$$\frac{d}{dt} e^{\boldsymbol{\theta} \cdot \mathbf{S}} = \left[ \dot{\boldsymbol{\theta}} + \frac{1 - \cos \theta}{\theta^2} \boldsymbol{\theta} \times \dot{\boldsymbol{\theta}} + \frac{\theta - \sin \theta}{\theta^3} \boldsymbol{\theta} \times (\boldsymbol{\theta} \times \dot{\boldsymbol{\theta}}) \right] e^{\boldsymbol{\theta} \cdot \mathbf{S}}. \quad (\text{B.19})$$

Inserting this into Eq. (B.13) with  $M$  taken from Eq. (B.16) we find

$$\dot{\boldsymbol{\theta}} + \frac{1 - \cos \theta}{\theta^2} \boldsymbol{\theta} \times \dot{\boldsymbol{\theta}} + \frac{\theta - \sin \theta}{\theta^3} \boldsymbol{\theta} \times (\boldsymbol{\theta} \times \dot{\boldsymbol{\theta}}) = \mathbf{J} = \begin{pmatrix} 0 \\ Q \\ 2\Omega \end{pmatrix}. \quad (\text{B.20})$$

A more concise version of Eq. (B.20) is obtained by writing  $\boldsymbol{\theta} = \theta \mathbf{n}$  with  $\mathbf{n}$  a unit vector. This leads to

$$\dot{\theta} \mathbf{n} + \sin \theta \dot{\mathbf{n}} + (1 - \cos \theta) \mathbf{n} \times \dot{\mathbf{n}} = \mathbf{J} = \begin{pmatrix} 0 \\ Q \\ 2\Omega \end{pmatrix}. \quad (\text{B.21})$$

Notably the same solution  $\boldsymbol{\theta}(t)$  to Eq. (B.20) (or (B.21)) yields solutions of both equations (2.21) and (2.29). This shows that they are just different ways to write the same underlying equation for the coefficients  $\boldsymbol{\theta}$  of the generators in their respective Lie algebras. Equations (B.20) and (B.21) can therefore be thought of as a ‘‘lift’’ of the differential equations (B.13) from the Lie group to the Lie algebra.

### B.3 Long term evolution of $f$ for a periodic field

In section 2.5 we saw that in the low-density approximation the phase space distribution  $f$  will grow with  $t_{\text{flat}}^2$  on a shell. We also remarked that this growth cannot last forever, because  $f \leq 2$ , and even before the validity of the LDA would be in question. We will study the true long-term behavior of  $f$  using the matrix valued differential equation (B.13) for the Bogoliubov coefficients, and for the sake of simplicity, we set  $t_{\text{on}} = 0$ . Because we only consider a periodic field, the matrix  $M$  is also periodic, i.e.  $M(t + T) = M(t)$  with the period  $T$ . By Floquet’s theorem, the solution matrix  $U$  can be written as a product of a periodic matrix and an exponential,

$$U(t) = P(t) e^{Rt}, \quad (\text{B.22})$$

with  $P(t + T) = P(t)$ . In particular from the initial condition  $U(0) = \mathbb{1}$  we find  $P(0) = \mathbb{1}$ . Therefore, when  $t$  is an integer multiple of  $T$ ,  $t = nT$  with  $n \in \mathbb{N}$ , we have  $P(nT) = \mathbb{1}$  and  $U(nT) = e^{nTR}$ . We can again decompose  $R$  into the generators  $S_i$ :  $R = \mathbf{r} \cdot \mathbf{S}$ . With a bit of algebra one can find  $(\mathbf{r} \cdot \mathbf{S})^2 = -r^2/2$ , which enables us to sum the exponential:

$$U(nT) = e^{nTR} = \cos \left( \frac{nTr}{\sqrt{2}} \right) \mathbb{1} + \frac{\sqrt{2}}{r} \sin \left( \frac{nTr}{\sqrt{2}} \right) \mathbf{r} \cdot \mathbf{S}. \quad (\text{B.23})$$

From Eq. (B.14) we see

$$\beta = \begin{pmatrix} 0 & 1 \end{pmatrix} U \begin{pmatrix} 1 \\ 0 \end{pmatrix} = \frac{\sqrt{2}}{r} \sin \left( \frac{nTr}{\sqrt{2}} \right) \frac{ir_1 - r_2}{2}, \quad (\text{B.24})$$



which we can insert into  $f = 2|\beta|^2$  to get (upon observing  $r^2 = r_1^2 + r_2^2 + r_3^2$ )

$$f = \left(1 - \frac{r_3^2}{r^2}\right) \sin^2\left(\frac{nTr}{\sqrt{2}}\right). \quad (\text{B.25})$$

To connect this to the periodic field with switching-on/off, we will argue heuristically (for a more thorough discussion see [85]). The short-term oscillations of  $f$ , as for example seen in Fig. 2.7, are carried by the matrix  $P$ . The long-term behavior and thus the accumulated residual density are carried by  $e^{Rt}$ . The deviation of  $P$  from the unit matrix should be proportional to the instantaneous amplitude of the field,  $E(t)$ . If we let this amplitude go to zero slowly enough in the switching-off process, that is over a large number of oscillations,  $P$  will go to  $\mathbf{1}$ . Then the residual  $f$  is given by (B.25), but with  $nT$  replaced by  $t_{\text{flat}}$ . This then yields the result for the long-term time evolution seen in the right panel of Fig. 2.9.



# C Generalized Bogoliubov transform

## C.1 Linear transformation of creation and annihilation operators

This section develops the theory of general linear transformations of fermionic creation/annihilation operators. The Bogoliubov transformation as well as the time evolution in a background field are special cases thereof, so we deem it prudent to understand the generic case first before specializing further.

Suppose we have a set of fermionic annihilation operators  $e_i$  with some general index  $i$ , which could for example be composed of momentum and spin,  $i = (r, \mathbf{p})$ . The sum over  $i$  would then be understood as the sum over spin and integration over the momentum, with a corresponding Kronecker delta:

$$\sum_i = \sum_r \int \frac{d^3p}{(2\pi)^3}, \quad \delta_{ij} = (2\pi)^3 \delta_{rs} \delta(\mathbf{p} - \mathbf{q}). \quad (\text{C.1})$$

We denote by the vector  $\mathbf{e}$  the collection of all those operators, and by  $\mathbf{e}^\dagger$  the collection of the corresponding creation operators.<sup>1</sup> A general linear transformation mixing  $\mathbf{e}$  and  $\mathbf{e}^\dagger$ , which results in new operators  $\mathbf{f}$  is given by (see e.g. [114, 115] and section 2.4 in [116])

$$\begin{aligned} \mathbf{f} &= \mu \mathbf{e} + \nu \mathbf{e}^\dagger, & f_i &= \sum_j \mu_{ij} e_j + \sum_j \nu_{ij} e_j^\dagger, \\ \mathbf{f}^\dagger &= \mu^* \mathbf{e}^\dagger + \nu^* \mathbf{e}, & f_i^\dagger &= \sum_j \mu_{ij}^* e_j^\dagger + \sum_j \nu_{ij}^* e_j. \end{aligned} \quad (\text{C.2})$$

We want to restrict that transformation, so that  $\mathbf{f}$  obeys the canonical anticommutation relations when  $\mathbf{e}$  does and vice versa, i.e.  $\{e_i, e_j\} = \delta_{ij} \iff \{f_i, f_j\} = \delta_{ij}$ . This gives the following constraints for the matrices  $\mu$  and  $\nu$ :

$$\begin{aligned} \mu \mu^\dagger + \nu \nu^\dagger &= \mathbb{1}, & \mu \nu^T + \nu \mu^T &= 0, \\ \mu^\dagger \mu + (\nu^\dagger \nu)^* &= \mathbb{1}, & \mu^\dagger \nu + (\nu^\dagger \mu)^* &= 0. \end{aligned} \quad (\text{C.3})$$

The second line is equivalent to the first, so there are only two independent equations. We list it because it is needed for simplifying some expressions further on. These constraints also guarantee the invertibility of the transformation (C.2) with the inverse given by

$$\begin{aligned} \mathbf{e} &= \mu^\dagger \mathbf{f} + \nu^T \mathbf{f}^\dagger, \\ \mathbf{e}^\dagger &= \mu^T \mathbf{f}^\dagger + \nu^\dagger \mathbf{f}. \end{aligned} \quad (\text{C.4})$$

For further technical reasons, we also want  $\mu$  to be invertible, i.e.  $\mu^{-1}$  must exist.

<sup>1</sup>This dagger only affects the components of that vector; it does not change it from column to row or vice versa.

The transformation (C.2) can be implemented by a unitary operator, the so called squeeze operator  $S$  through

$$\mathbf{f} = S^\dagger \mathbf{e} S, \quad S = \exp \left[ -i \mathbf{e}^\dagger \sigma \mathbf{e} \right] \exp \left[ \frac{1}{2} \mathbf{e}^\dagger \rho^\dagger \mathbf{e}^\dagger - \frac{1}{2} \mathbf{e} \rho \mathbf{e} \right]. \quad (\text{C.5})$$

By a slight abuse of notation,  $\mathbf{e} \sigma \mathbf{e}$  stands for the bilinear product  $\sum_{ij} e_i \sigma_{ij} e_j$ ; analogously for  $\mathbf{e}^\dagger \sigma \mathbf{e}$  and  $\mathbf{e}^\dagger \sigma^\dagger \mathbf{e}^\dagger$ . Because the  $e_i$  are fermionic, we can restrict  $\rho$  to be skew-symmetric,  $\rho^T = -\rho$ . We also restrict  $\sigma$  to be Hermitian,  $\sigma^\dagger = \sigma$ . Then both exponentials are unitary and also  $S$  as the product of both. To evaluate  $\mathbf{f}$  from (C.5) we need the following iterated commutators

$$\begin{aligned} \left[ \frac{1}{2} \mathbf{e} \rho \mathbf{e} - \frac{1}{2} \mathbf{e}^\dagger \rho^\dagger \mathbf{e}^\dagger, \mathbf{e} \right]_{2n} &= (-1)^n |\rho|^{2n} \mathbf{e}, \\ \left[ \frac{1}{2} \mathbf{e} \rho \mathbf{e} - \frac{1}{2} \mathbf{e}^\dagger \rho^\dagger \mathbf{e}^\dagger, \mathbf{e} \right]_{2n+1} &= (-1)^n |\rho|^{2n} \rho^\dagger \mathbf{e}^\dagger, \\ \left[ i \mathbf{e}^\dagger \sigma \mathbf{e}, \mathbf{e} \right]_n &= (-i\sigma)^n \mathbf{e}, \end{aligned} \quad (\text{C.6})$$

with  $|\rho| = \sqrt{\rho^\dagger \rho}$ .<sup>2</sup> With this we can employ a variant of the Baker-Campbell-Hausdorff formula (also known as Hadamard's lemma) which states  $e^X Y e^{-X} = \sum_n [X, Y]_n / n!$  to get

$$\begin{aligned} \mathbf{f} &= S^\dagger \mathbf{e} S = e^{\frac{1}{2} \mathbf{e} \rho \mathbf{e} - \frac{1}{2} \mathbf{e}^\dagger \rho^\dagger \mathbf{e}^\dagger} \sum_{n=0}^{\infty} \frac{\left[ i \mathbf{e}^\dagger \sigma \mathbf{e}, \mathbf{e} \right]_n}{n!} e^{\frac{1}{2} \mathbf{e}^\dagger \rho^\dagger \mathbf{e}^\dagger - \frac{1}{2} \mathbf{e} \rho \mathbf{e}} \\ &= e^{-i\sigma} \sum_{n=0}^{\infty} \frac{\left[ \frac{1}{2} \mathbf{e} \rho \mathbf{e} - \frac{1}{2} \mathbf{e}^\dagger \rho^\dagger \mathbf{e}^\dagger, \mathbf{e} \right]_{2n}}{(2n)!} + e^{-i\sigma} \sum_{n=0}^{\infty} \frac{\left[ \frac{1}{2} \mathbf{e} \rho \mathbf{e} - \frac{1}{2} \mathbf{e}^\dagger \rho^\dagger \mathbf{e}^\dagger, \mathbf{e} \right]_{2n+1}}{(2n+1)!} \\ &= e^{-i\sigma} \cos |\rho| \mathbf{e} + e^{-i\sigma} \frac{\sin |\rho|}{|\rho|} \rho^\dagger \mathbf{e}^\dagger. \end{aligned} \quad (\text{C.7})$$

Note that the notation  $\sin |\rho| / |\rho|$  is sensible, since any two functions of the same matrix  $|\rho|$  commute. The matrix  $\sigma$  generates an ‘‘internal’’ unitary transformation, only mixing creation with creation and annihilation with annihilation operators, while  $\rho$  makes them mingle amongst each other. Comparing Eq. (C.2) with Eq. (C.7), we see

$$\mu = e^{-i\sigma} \cos |\rho|, \quad \nu = e^{-i\sigma} \frac{\sin |\rho|}{|\rho|} \rho^\dagger. \quad (\text{C.8})$$

The invertibility of  $\mu$  is then guaranteed if every eigenvalue of  $|\rho|$  is  $< \pi/2$ . The  $\mu$  and  $\nu$  thus defined by  $\rho$  and  $\sigma$  through the unitary transformation  $S$  already fulfill the constraints (C.3). The first is simple:

$$\begin{aligned} \mu \mu^\dagger + \nu \nu^\dagger &= e^{-i\sigma} \cos^2 |\rho| e^{i\sigma} + e^{-i\sigma} \frac{\sin |\rho|}{|\rho|} \rho^\dagger \rho \frac{\sin |\rho|}{|\rho|} e^{i\sigma} \\ &= e^{-i\sigma} \left( \cos^2 |\rho| + \sin^2 |\rho| \right) e^{i\sigma} = \mathbb{1}. \end{aligned} \quad (\text{C.9})$$

For the second we note  $\rho^\dagger |\rho|^2{}^T = |\rho|^2 \rho^\dagger$  (due to  $\rho^T = -\rho$ ), therefore for any even function of  $|\rho|$ :  $\rho^\dagger f(|\rho|^2)^T = f(|\rho|^2) \rho^\dagger$ . This applies to both  $\cos |\rho|$  and  $\sin |\rho| / |\rho|$  and we get

$$\begin{aligned} \mu \nu^T + \nu \mu^T &= e^{-i\sigma} \cos |\rho| \rho^\dagger{}^T \left( \frac{\sin |\rho|}{|\rho|} \right)^T e^{-i\sigma^T} + e^{-i\sigma} \frac{\sin |\rho|}{|\rho|} \rho^\dagger (\cos |\rho|)^T e^{-i\sigma^T} \\ &= e^{-i\sigma} \left( -\cos |\rho| \frac{\sin |\rho|}{|\rho|} \rho^\dagger + \frac{\sin |\rho|}{|\rho|} \cos |\rho| \rho^\dagger \right) e^{-i\sigma^T} = 0. \end{aligned} \quad (\text{C.10})$$

<sup>2</sup>Since  $\rho^\dagger \rho$  is a positive definite matrix, this square root is uniquely defined.

The relation (C.8) between  $\rho$ ,  $\sigma$  and  $\mu$ ,  $\nu$  is invertible (except for the branch cuts of the logarithm, when computing  $\sigma$  from  $e^{-i\sigma}$ ). First we calculate  $|\rho|$ , then  $e^{-i\sigma}$  (from which  $\sigma$ ) and at last with both the complete  $\rho$ :

$$|\rho| = \arccos \sqrt{\mu^\dagger \mu}, \quad e^{-i\sigma} = \mu(\mu^\dagger \mu)^{-1/2}, \quad \sigma = i \log e^{-i\sigma}, \quad \rho = \nu^\dagger e^{-i\sigma} \frac{|\rho|}{\sin |\rho|}. \quad (\text{C.11})$$

Note that we needed  $\mu$  to be invertible, as we demanded, to invert Eq. (C.8). We see that the transformations (C.2) and (C.5) changing  $\mathbf{e}$  to  $\mathbf{f}$  are equivalent as long as  $\mu$  is invertible and all eigenvalues of  $|\rho|$  are  $< \pi/2$ .<sup>3</sup> We will always assume this and use both transformations interchangeably from now on.

Let us denote the vacuum of the operators  $e_i$  by  $|0_e\rangle$  and that of the  $f_i$  by  $|0_f\rangle$ . All the operators annihilate their respective vacuum,  $e_i |0_e\rangle = 0$  and  $f_i |0_f\rangle = 0$ . From Eq. (C.5) we easily see  $|0_f\rangle = S^\dagger |0_e\rangle$ . An important quantity is the vacuum persistence amplitude (VPA)  $c_V$ , the overlap between  $|0_e\rangle$  and  $|0_f\rangle$

$$c_V = \langle 0_f | 0_e \rangle = \langle 0_e | S | 0_e \rangle = \langle 0_f | S | 0_f \rangle. \quad (\text{C.12})$$

We evaluate the new vacuum  $|0_f\rangle$  with the following ansatz

$$|0_f\rangle = S^\dagger |0_e\rangle = \exp \left[ \frac{1}{2} \mathbf{e} \rho \mathbf{e} - \frac{1}{2} \mathbf{e}^\dagger \rho^\dagger \mathbf{e}^\dagger \right] |0_e\rangle \stackrel{!}{=} c_V \exp \left[ \frac{1}{2} \mathbf{e}^\dagger \tau \mathbf{e}^\dagger \right] |0_e\rangle. \quad (\text{C.13})$$

This is justified since  $\mathbf{e} \mathbf{e}^{\dagger \tau \mathbf{e}^\dagger / 2} |0_e\rangle \propto \mathbf{e}^\dagger \mathbf{e}^{\dagger \tau \mathbf{e}^\dagger / 2} |0_e\rangle$  and therefore  $\mathbf{f} |0_f\rangle = (\mu \mathbf{e} + \nu \mathbf{e}^\dagger) |0_f\rangle = 0$  for the right  $\mu$  and  $\nu$ . We must determine  $\tau$  and  $c_V$  in the ansatz (C.13) from  $\rho$ . To do this, we employ the following trick. Define a vector depending on  $s \in [0, 1]$  by

$$|s\rangle = \exp \left[ \frac{s}{2} \mathbf{e} \rho \mathbf{e} - \frac{s}{2} \mathbf{e}^\dagger \rho^\dagger \mathbf{e}^\dagger \right] |0_e\rangle \stackrel{!}{=} f(s) \exp \left[ \frac{1}{2} \mathbf{e}^\dagger g(s) \mathbf{e}^\dagger \right] |0_e\rangle. \quad (\text{C.14})$$

Behind the second equals sign is an analogous ansatz as above for  $|0_f\rangle$ . The function  $f(s)$  is a scalar and because  $|s=1\rangle = |0_f\rangle$ ,  $f(0) = 1$  and  $f(1) = c_V$ ;  $g(s)$  is a matrix and  $g(0) = 0$  and  $g(1) = \tau$ . Our strategy is to compare the derivatives for both expressions of  $|s\rangle$  to derive a differential equation for  $f$  and  $g$ . Solving these and evaluating at  $f(1)$  and  $g(1)$  we will get  $c_V$  and  $\tau$ . The derivative of the first expression is

$$\begin{aligned} \frac{d}{ds} \exp \left[ \frac{s}{2} \mathbf{e} \rho \mathbf{e} - \frac{s}{2} \mathbf{e}^\dagger \rho^\dagger \mathbf{e}^\dagger \right] |0_e\rangle &= \left( \frac{1}{2} \mathbf{e} \rho \mathbf{e} - \frac{1}{2} \mathbf{e}^\dagger \rho^\dagger \mathbf{e}^\dagger \right) \exp \left[ \frac{s}{2} \mathbf{e} \rho \mathbf{e} - \frac{s}{2} \mathbf{e}^\dagger \rho^\dagger \mathbf{e}^\dagger \right] |0_e\rangle \\ &= \left( \frac{1}{2} \mathbf{e} \rho \mathbf{e} - \frac{1}{2} \mathbf{e}^\dagger \rho^\dagger \mathbf{e}^\dagger \right) f(s) \exp \left[ \frac{1}{2} \mathbf{e}^\dagger g(s) \mathbf{e}^\dagger \right] |0_e\rangle. \end{aligned} \quad (\text{C.15})$$

The second equals sign is using the ansatz (C.14). The derivative of the second expression is

$$\frac{d}{ds} f(s) \exp \left[ \frac{1}{2} \mathbf{e}^\dagger g(s) \mathbf{e}^\dagger \right] |0_e\rangle = \left( f'(s) + f(s) \frac{1}{2} \mathbf{e}^\dagger g'(s) \mathbf{e}^\dagger \right) \exp \left[ \frac{1}{2} \mathbf{e}^\dagger g(s) \mathbf{e}^\dagger \right] |0_e\rangle. \quad (\text{C.16})$$

<sup>3</sup>Interestingly this restriction is not needed for bosonic operators, where  $\mu$  is always invertible and  $\cosh$  takes the place of  $\cos$  in Eq. (C.7).

Setting both equal and multiplying from the left by  $e^{-e^\dagger g(s) e^\dagger / 2}$  we get<sup>4</sup>

$$\begin{aligned} f(s) \exp \left[ -\frac{1}{2} e^\dagger g(s) e^\dagger \right] \frac{1}{2} e \rho e \exp \left[ \frac{1}{2} e^\dagger g(s) e^\dagger \right] |0_e\rangle &- f(s) \frac{1}{2} e^\dagger \rho^\dagger e^\dagger |0_e\rangle \\ &= \frac{1}{2} f(s) \text{tr}(\rho g(s)) |0_e\rangle - \frac{1}{2} f(s) e^\dagger g(s) \rho g(s) e^\dagger |0_e\rangle - \frac{1}{2} f(s) e^\dagger \rho^\dagger e^\dagger |0_e\rangle \\ &\stackrel{!}{=} f'(s) |0_e\rangle + f(s) \frac{1}{2} e^\dagger g'(s) e^\dagger |0_e\rangle. \end{aligned} \quad (\text{C.17})$$

By comparing all the linearly independent vectors component wise we find the desired differential equations

$$\begin{aligned} f'(s) &= \frac{1}{2} \text{tr}(\rho g(s)) f(s), \quad f(0) = 1, \\ g'(s) &= -g(s) \rho g(s) - \rho^\dagger, \quad g(0) = 0. \end{aligned} \quad (\text{C.18})$$

Solving these and evaluating at  $s = 1$  yields

$$\begin{aligned} \tau &= -\frac{\tan |\rho|}{|\rho|} \rho^\dagger = -\mu^{-1} \nu, \\ c_V &= \sqrt{\det \cos |\rho|} = \sqrt{\det |\mu|}. \end{aligned} \quad (\text{C.19})$$

All put together we get the beautiful<sup>5</sup> formula

$$e^{\frac{1}{2} e \rho e - \frac{1}{2} e^\dagger \rho^\dagger e^\dagger} |0_e\rangle = \sqrt{\det \cos |\rho|} e^{-\frac{1}{2} e^\dagger \frac{\tan |\rho|}{|\rho|} \rho^\dagger e^\dagger} |0_e\rangle. \quad (\text{C.20})$$

In summary for the new vacuum we get two equivalent expressions, once expressed in  $\rho$ ,<sup>6</sup> and once in  $\mu$  and  $\nu$ :

$$|0_f\rangle = \sqrt{\det \cos |\rho|} e^{-\frac{1}{2} e^\dagger \frac{\tan |\rho|}{|\rho|} \rho^\dagger e^\dagger} |0_e\rangle = \sqrt{\det |\mu|} e^{-\frac{1}{2} e^\dagger \mu^{-1} \nu e^\dagger} |0_e\rangle. \quad (\text{C.21})$$

Having both vacua at our disposal, we can calculate expectation values and matrix elements with them. For example, the number of all old particles in the new vacuum is

$$\begin{aligned} \langle 0_f | e^\dagger e | 0_f \rangle &= \langle 0_f | (\mathbf{f}^\dagger \mu + \mathbf{f} \nu^*) (\mu^\dagger \mathbf{f} + \nu^T \mathbf{f}^\dagger) | 0_f \rangle = \langle 0_f | \mathbf{f} \nu^* \nu^T \mathbf{f}^\dagger | 0_f \rangle \\ &= \text{tr}(\nu \nu^\dagger) \end{aligned} \quad (\text{C.22})$$

which is the same as the number of new particles in the old vacuum

$$\langle 0_e | \mathbf{f}^\dagger \mathbf{f} | 0_e \rangle = \text{tr}(\nu \nu^\dagger). \quad (\text{C.23})$$

These calculations are straightforward: For example, when we have an expectation value w.r.t.  $\langle 0_f | \dots | 0_f \rangle$ , we express all sandwiched operators in terms of  $f_i$  and  $f_i^\dagger$  using Eq. (C.4). Then we can use the standard Wick's theorem to get the result (C.23).

Computing matrix elements is a bit harder, because there the operators get sandwiched between different vacua. Suppose we want to compute  $\langle 0_f | ABCD | 0_e \rangle$  with operators  $A$ ,

<sup>4</sup>Note that all bilinear products of the form  $e^\dagger \tau e^\dagger$  commute with all  $e_i^\dagger$ . Also note that we again used Hadamard's lemma.

<sup>5</sup>Beauty is in the eye of the beholder.

<sup>6</sup>The new vacuum does not depend on  $\sigma$ , since this matrix, as mentioned, only creates an internal transformation among creation and annihilation operators.

$\overline{ab}/c_V$	$e$	$e^\dagger$	$f$	$f^\dagger$
$e$	0	1	$\nu^T$	$\mu^\dagger$
$e^\dagger$	0	$\nu^\dagger \mu^{\dagger-1}$	$\nu^\dagger \mu^\dagger \nu^T$	$\nu^\dagger$
$f$	0	$\mu^{\dagger-1}$	$\mu^{\dagger-1} \nu^T$	1
$f^\dagger$	0	0	0	0

**Table C.1:** All generalized contractions between the operators  $e$ ,  $e^\dagger$ ,  $f$  and  $f^\dagger$  scaled by the vacuum persistence amplitude  $c_V = \langle 0_f | 0_e \rangle$ .

$B$ ,  $C$  and  $D$  linear in  $e$ ,  $e^\dagger$ ,  $f$  and  $f^\dagger$ . The trick is to express them only in terms of  $e$  and  $f^\dagger$ . This can be done because from Eq. (C.2), the constraints (C.3) and our assumption that  $\mu$  be invertible we find

$$\begin{aligned} e^\dagger &= \nu^\dagger \mu^{\dagger-1} e + \mu^{*-1} f^\dagger, \\ f &= \mu^{\dagger-1} e + \nu \mu^{*-1} f^\dagger. \end{aligned} \tag{C.24}$$

Therefore every such operator  $A$  can be split into a “positive” and “negative” part,  $A = A^{(+)} + A^{(-)} = \sum_i a_i^{(+)} f_i^\dagger + \sum_i a_i^{(-)} e_i$  with some coefficients  $a_i^{(+)}$  and  $a_i^{(-)}$ . Importantly  $\langle 0_f | A^{(+)} = 0$  and  $A^{(-)} | 0_e \rangle = 0$ . This is already enough to prove a generalized form of Wick’s theorem involving generalized contractions. For our example, this allows us to compute the value of the operators sandwiched between the two vacua as<sup>7</sup>

$$\langle 0_f | ABCD | 0_e \rangle = \overline{ABCD} - \overline{AB} \overline{CD} + \overline{AC} \overline{BD} \tag{C.25}$$

with the contraction defined as

$$\overline{AB} = \langle 0_f | AB | 0_e \rangle. \tag{C.26}$$

By knowing every such contraction between  $e$ ,  $e^\dagger$ ,  $f$  and  $f^\dagger$  we can calculate every matrix element. The most fundamental one to which the others can be reduced is

$$\overline{e_i f_j^\dagger} = \langle 0_f | e_i f_j^\dagger | 0_e \rangle = \{e_i, f_j^\dagger\} \langle 0_f | 0_e \rangle = c_V \mu_{ij}^\dagger. \tag{C.27}$$

The contractions will turn out to be proportional to  $c_V = \langle 0_f | 0_e \rangle$ . For completeness’ sake, we list them all in table C.1 (scaled by  $c_V$ ). Because  $e^\dagger$ ,  $e$  and  $f$ ,  $f^\dagger$  anticommute, the matrices of their contractions must be skew-symmetric. This is guaranteed by the constraints (C.3).

## C.2 Second quantization

We can use the machinery developed in the previous section to compute the dynamics generated by a time dependent Hamiltonian in the second-quantized Fock space by reducing them to the dynamics in the base Hilbert space. It is crucial to keep the Heisenberg and Schrödinger picture separate. We therefore consistently attach a subscript  $S$  to every

<sup>7</sup>The sign is due to the operators being fermionic. We have to make all contracted operators adjacent, introducing a  $-1$  every time we have to swap two operators to that end.

operator in the Schrödinger picture. Operators in the Heisenberg picture remain bare. Every index here is understood the same as in the preceding paragraph to possibly be composed of multiple sub-indices, some of which may be continuous.

The starting point is some time dependent Hamiltonian  $h(t)$  acting on some Hilbert space. Since this is a first-quantized operator, we denote it by a small  $h$  to distinguish it from the second-quantized  $H(t)$ . We assume  $\dot{h}(t \leq 0) = 0$  and call  $h(t \leq 0)$  the free Hamiltonian. We also want  $h(t)$  to have a spectrum not bounded from below, so that we can describe particles and anti-particles with it. The model for this is of course the free Dirac Hamiltonian. Thus at all times  $h(t)$  has an eigenbasis comprised of  $U_i(t)$  and  $V_i(t)$  with eigenvalues  $\epsilon_i^+(t)$  and  $\epsilon_i^-(t)$ , that is

$$h(t)U_i(t) = \epsilon_i^+(t)U_i(t), \quad h(t)V_i(t) = \epsilon_i^-(t)V_i(t). \quad (\text{C.28})$$

Another canonical basis is formed by solutions  $u_i(t)$ ,  $v_i(t)$  to Schrödinger's equation

$$\begin{aligned} i\partial_t u_i(t) &= h(t)u_i(t), & u_i(0) &= u_i = U_i(0), \\ i\partial_t v_i(t) &= h(t)v_i(t), & v_i(0) &= v_i = V_i(0). \end{aligned} \quad (\text{C.29})$$

We let both bases coincide at  $t = 0$  as the initial condition and name these vectors  $u_i$  and  $v_i$  by a slight abuse of notation. This is sensible since for  $t \leq 0$ ,  $U_i(t \leq 0) = U_i(t = 0) = u_i$  and  $u_i(t \leq 0) = e^{-i\epsilon_i^+(t=0)t}u_i$  (similarly for  $V_i(t)$  and  $v_i(t)$ ), i.e. the time evolution before the time dependence of the Hamiltonian is switched on is simple. A unitary matrix transforming one basis into the other must necessarily exist:

$$\begin{aligned} u_i(t) &= \sum_j U_j(t)B_{ji}^{++}(t) + \sum_j V_j(t)B_{ji}^{-+}(t), \\ v_i(t) &= \sum_j U_j(t)B_{ji}^{+-}(t) + \sum_j V_j(t)B_{ji}^{--}(t). \end{aligned} \quad (\text{C.30})$$

The transformation (2.20) is a special case of this. The matrices  $B^{\pm\pm}$  can be computed with the scalar product  $u^\dagger v$  between two vectors  $u$  and  $v$  in the first-quantized Hilbert space

$$\begin{aligned} B_{ij}^{++}(t) &= U_i^\dagger(t)u_j(t), & B_{ij}^{-+}(t) &= V_i^\dagger(t)u_j(t), \\ B_{ij}^{+-}(t) &= U_i^\dagger(t)v_j(t), & B_{ij}^{--}(t) &= V_i^\dagger(t)v_j(t). \end{aligned} \quad (\text{C.31})$$

Second quantization proceeds by creating a field operator  $\Psi_S$ , which is simply a linear combination of the base vectors with fermionic creation/annihilation operators

$$\Psi_S = \sum_i \left( c_{i,S} u_i + d_{i,S}^\dagger v_i \right). \quad (\text{C.32})$$

The coefficients  $c_{i,S}$  are annihilation operators for particles, the  $d_{i,S}^\dagger$  creation operators for anti-particles. This is the well known trick that solves the Dirac-sea problem in the quantum field theoretical setting. Note our labeling convention in the attached subscript  $S$ . The field operator obeys the relation  $\{\Psi_S, \Psi_S^\dagger\} = 1$ . The “1” acts on the space spanned by the  $u_i$  and  $v_i$ , the first-quantized Hilbert space. The vacuum is defined by  $c_{i,S} |0\rangle = d_{i,S} |0\rangle = 0$ .

With the field operator, we can lift the Hamiltonian to its second-quantized form  $H_S(t) = \Psi_S^\dagger h(t) \Psi_S$ . Both  $\Psi_S$  and  $H_S(t)$  are in the Schrödinger picture. Despite that,  $H_S(t)$



carries an explicit time dependence inherited from  $h(t)$ . The Schrödinger equation in its second-quantized form is best formulated in terms of the time evolution operator  $U$ :<sup>8</sup>

$$i\partial_t U(t) = H_S(t)U(t), \quad U(t=0) = \mathbb{1}. \quad (\text{C.33})$$

This time evolution allows us to move between the Schrödinger and Heisenberg picture. For any operator  $A$  (even having an explicit time dependency) we define  $A(t) = U^\dagger(t)A_S(t)U(t)$ . We can apply this to  $\Psi_S$  to form  $\Psi(t)$  and to  $H_S(t)$  resulting in  $H(t) = \Psi^\dagger(t)h(t)\Psi(t)$ . If  $\dot{H}_S(t)$  commuted with  $H_S(t)$  (e.g. when  $H_S$  is time independent),  $H_S(t)$  would also commute with  $U(t)$  and  $H_S(t) = H(t)$ . Using Eq. (C.33) it is easy to see  $\Psi(t)$  obeys Heisenberg's equation of motion

$$i\partial_t \Psi(t) = [\Psi(t), H(t)] = h(t)\Psi(t). \quad (\text{C.34})$$

We can decompose  $\Psi(t)$  in the three different bases we encountered, thereby shifting the time dependence between the operators and base vectors:

$$\begin{aligned} \Psi(t) &= \sum_i \left( c_i(t)u_i + d_i^\dagger(t)v_i \right) = \sum_i \left( c_{i,S}u_i(t) + d_{i,S}^\dagger v_i(t) \right) \\ &= \sum_i \left( C_i(t)U_i(t) + D_i^\dagger(t)V_i(t) \right). \end{aligned} \quad (\text{C.35})$$

From the second form it is clear, that the Heisenberg equation of motion (C.34) is equivalent to the Schrödinger equation (C.29) in first quantization. As per our convention,  $c_i(t) = U^\dagger(t)c_{i,S}U(t)$  (same for  $d_i$ ). The operators  $C_i(t)$  and  $D_i(t)$  have not yet been introduced. They are defined by the above expansion, and can be obtained from  $c_{i,S}$  and  $d_{i,S}$  by a suitable unitary operator  $B(t)$ . The component expression of that operator is given by the matrix  $B_{ij}^{\pm\pm}(t)$  from Eq. (C.31)

$$\begin{aligned} C_i(t) &= B^\dagger(t)c_{i,S}B(t) = \sum_j \left( B_{ij}^{++}(t)c_{j,S} + B_{ij}^{+-}(t)d_{j,S}^\dagger \right), \\ D_i^\dagger(t) &= B^\dagger(t)d_{i,S}^\dagger B(t) = \sum_j \left( B_{ij}^{-+}(t)c_{j,S} + B_{ij}^{--}(t)d_{j,S}^\dagger \right), \end{aligned} \quad (\text{C.36})$$

or written in matrix notation, with the operators collected into a vector as in the previous section:<sup>9</sup>

$$\begin{pmatrix} \mathbf{C} \\ \mathbf{D}^\dagger \end{pmatrix} = B^{\pm\pm} \begin{pmatrix} \mathbf{c}_S \\ \mathbf{d}_S^\dagger \end{pmatrix} = \begin{pmatrix} B^{++} & B^{+-} \\ B^{-+} & B^{--} \end{pmatrix} \begin{pmatrix} \mathbf{c}_S \\ \mathbf{d}_S^\dagger \end{pmatrix} = \begin{pmatrix} B^{++}\mathbf{c}_S + B^{+-}\mathbf{d}_S^\dagger \\ B^{-+}\mathbf{c}_S + B^{--}\mathbf{d}_S^\dagger \end{pmatrix}. \quad (\text{C.37})$$

The unitarity of the matrix  $B^{\pm\pm}(t)$  guarantees that  $B(t)$  is unitary, from which in turn the anticommutation relations for  $\mathbf{C}(t)$  and  $\mathbf{D}(t)$  follow at all times. We call  $B(t)$  the (generalized) Bogoliubov transform. It is a generalization of Eq. (2.23). This can be seen by specializing the index  $i$  to  $i = (r, \mathbf{p})$ ,  $r$  being the spin and  $\mathbf{p}$  the momentum. Then  $B_{ij}^{\pm\pm}(t) = B_{rs}^{\pm\pm}(t, \mathbf{p}, \mathbf{q})$  and by setting

$$\begin{pmatrix} B_{rs}^{++}(t, \mathbf{p}, \mathbf{q}) & B_{rs}^{+-}(t, \mathbf{p}, \mathbf{q}) \\ B_{rs}^{-+}(t, \mathbf{p}, \mathbf{q}) & B_{rs}^{--}(t, \mathbf{p}, \mathbf{q}) \end{pmatrix} = (2\pi)^3 \delta_{rs} \delta(\mathbf{p} - \mathbf{q}) \begin{pmatrix} \alpha(t, \mathbf{p}) & -\beta^*(t, \mathbf{p}) \\ \beta(t, \mathbf{p}) & \alpha^*(t, \mathbf{p}) \end{pmatrix} \quad (\text{C.38})$$

<sup>8</sup>The time evolution does not, strictly speaking, belong to any picture, therefore it is exempted from our convention. We also hope no confusion arises between the time dependent eigenvectors  $U_i(t)$  and  $U(t)$ .

<sup>9</sup>We also suppress the time argument, which we will sometimes do for legibility's sake from now on.

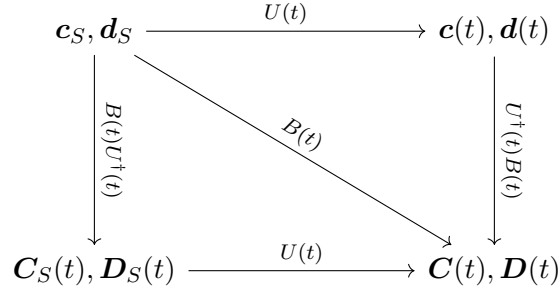


**Figure C.1:** The different annihilation operators from the text and the unitary transformations between them. In the left column, the operators are in the Schrödinger picture, in the right in the Heisenberg picture. The operators in the lower row are the Bogoliubov transformed versions of those in the upper row.

Eq. (C.36) reduces to Eq. (2.23). We see the Bogoliubov transformation (2.23) is diagonal in spin and momentum, which reduces Schrödinger’s (i.e. Dirac’s) equation to an ordinary differential equation, instead of the general partial differential equation. The eigenvectors  $U_i(t) = U_r(t, \mathbf{p})$  (same for  $V_i(t)$ ) are also easily obtained in this case. In general the eigenproblem is also a partial differential equation at each time  $t$ .

We have to introduce one more set of operators which are the Schrödinger-picture variants of  $C_i$  and  $D_i$ . They follow from an expansion of  $\Psi_S$  in the base vectors  $U_i$  and  $V_i$ , similar to above:

$$\Psi_S = \sum_i \left( c_{i,S} u_i + d_{i,S}^\dagger v_i \right) = \sum_i \left( C_{i,S}(t) U_i(t) + D_{i,S}^\dagger(t) V_i(t) \right). \quad (\text{C.39})$$

Evidently  $C_S(t) = U(t)C(t)U^\dagger(t)$  (same for  $D_S(t)$ ). To not get lost in this maze of operators and their transformations, we provide an overview in the form of a commutative diagram in figure C.1. The “big” operators are important, because they diagonalize  $H_S(t)$  and  $H(t)$ :

$$\begin{aligned} H_S(t) &= \Psi_S^\dagger h(t) \Psi_S = \sum_i \left( \epsilon_i^+(t) C_{i,S}^\dagger(t) C_{i,S}(t) + \epsilon_i^-(t) D_{i,S}(t) D_{i,S}^\dagger(t) \right), \\ H(t) &= \Psi^\dagger(t) h(t) \Psi(t) = \sum_i \left( \epsilon_i^+(t) C_i^\dagger(t) C_i(t) + \epsilon_i^-(t) D_i(t) D_i^\dagger(t) \right). \end{aligned} \quad (\text{C.40})$$

In terms of the “small” operators, both expansions would contain off-diagonal terms. The ground state of  $H_S(t)$  is given by the vacuum  $|\Omega_S(t)\rangle$  to  $C_{i,S}(t)$  and  $D_{i,S}(t)$ ,  $C_{i,S} |\Omega_S\rangle = D_{i,S} |\Omega_S\rangle = 0$ . For  $H(t)$  it is  $|\Omega(t)\rangle$  with  $C_i |\Omega\rangle = D_i |\Omega\rangle = 0$ . The vacuum  $|\Omega\rangle$  is *not* the time evolution of  $|\Omega_S\rangle$ , in fact the reverse holds:  $|\Omega(t)\rangle = U^\dagger(t) |\Omega_S(t)\rangle$ .

Precisely because they diagonalize the Hamiltonian, it is sensible to take these operators to represent the physical, measurable particles. If for example after some time  $t_{\text{off}}$ ,  $\dot{h}(t \geq t_{\text{off}}) = 0$  but  $h(t)$  did not return to be the free Hamiltonian, then  $C_{i,S}$  and  $D_{i,S}$  would become time independent and diagonalize the time independent Hamiltonian. Just as  $c_{i,S}$  and  $d_{i,S}$  diagonalize the free Hamiltonian. Yet  $C_{i,S}$ ,  $D_{i,S}$  would still be different from  $c_{i,S}$ ,  $d_{i,S}$ . So in this case there could be no prescription for two observers living in  $t < 0$  and  $t > t_{\text{off}}$  saying  $c_{i,S}$ ,  $d_{i,S}$  represent measurable particles but  $C_{i,S}$ ,  $D_{i,S}$  don’t. Consequently we take  $C_{i,S}(t)$  and  $D_{i,S}(t)$  to span our instantaneous Fock space and calculate expectation values and matrix elements with them.

For example, by the standard rules of quantum mechanics, if we want to know the number of particles of type  $i$  the vacuum contains we proceed as follows: Time evolve the state, i.e.  $U(t)|0\rangle$ , and sandwich the corresponding operator in between,  $\langle 0|U^\dagger(t)C_{i,S}^\dagger(t)C_{i,S}(t)U(t)|0\rangle = \langle 0|C_i^\dagger(t)C_i(t)|0\rangle$ . This is easily expressed by converting the “big” to the “small” operators with the Bogoliubov transformation (C.36) and its representation matrices  $B^{\pm\pm}$  as

$$\begin{aligned}\langle 0|C_i^\dagger C_i|0\rangle &= \sum_{kl} \langle 0| \left( B_{ik}^{+++*} c_{k,S}^\dagger + B_{ik}^{+-*} d_{k,S} \right) \left( B_{il}^{++} c_{l,S} + B_{il}^{+-} d_{l,S}^\dagger \right) |0\rangle \\ &= \sum_{kl} B_{ik}^{+-*} B_{il}^{+-} \langle 0|d_{k,S} d_{l,S}^\dagger|0\rangle = \left( B^{+-} B^{+-\dagger} \right)_{ii}.\end{aligned}\tag{C.41}$$

If we again specialize to the matrices (C.38) we find

$$\langle 0|C_i^\dagger(t)C_i(t)|0\rangle = (2\pi)^3 \delta(\mathbf{0}) \delta_{rr} |\beta(t, \mathbf{p})|^2\tag{C.42}$$

which is just the result from (2.27).

Any sensible expectation value can thus be expressed as

$$\langle 0|U^\dagger E(\mathbf{C}_S, \mathbf{D}_S, \mathbf{C}_S^\dagger, \mathbf{D}_S^\dagger)U|0\rangle = \langle 0|E(\mathbf{C}, \mathbf{D}, \mathbf{C}^\dagger, \mathbf{D}^\dagger)|0\rangle\tag{C.43}$$

with some function  $E$  of the “big” (Bogoliubov transformed) operators and the initial vacuum  $|0\rangle$ . Its value then follows from the matrices  $B^{\pm\pm}$ .

For matrix elements we have to make the connection to the previous section. The transformation (C.36) is a general linear transformation of operators as given by Eq. (C.2). We set  $\mathbf{e}$  to be the concatenation of  $\mathbf{c}_S$  and  $\mathbf{d}_S$ ,  $\mathbf{f}$  of  $\mathbf{C}(t)$  and  $\mathbf{D}(t)$ . The matrices  $\mu$  and  $\nu$  follow from the  $B^{\pm\pm}(t)$ . Explicitly

$$\begin{aligned}\mathbf{e} &= \begin{pmatrix} \mathbf{c}_S \\ \mathbf{d}_S \end{pmatrix}, \quad \mathbf{f} = \begin{pmatrix} \mathbf{C} \\ \mathbf{D} \end{pmatrix}, \\ \mu &= \begin{pmatrix} B^{++} & 0 \\ 0 & B^{--*} \end{pmatrix}, \quad \nu = \begin{pmatrix} 0 & B^{+-} \\ B^{-+*} & 0 \end{pmatrix}.\end{aligned}\tag{C.44}$$

The constraints (C.3) are equivalent to the unitarity of  $B^{\pm\pm}$ . With this we have the entire machinery of the previous section at our disposal.

The simplest amplitude, for example, is the vacuum persistence amplitude. The initial state can only be  $|0\rangle$ , while the final state must be the vacuum to the *Schrödinger*-picture operators  $C_{i,S}$  and  $D_{i,S}$ :  $|\Omega_S\rangle$ . The VPA is then the overlap between  $|\Omega_S(t)\rangle$  and the time evolution of  $|0\rangle$ , that is  $c_V = \langle \Omega_S(t)|U(t)|0\rangle = \langle \Omega(t)|0\rangle$ . With the matrices  $\mu$  and  $\nu$  from Eq. (C.44) it follows directly from Eq. (C.19) as

$$\begin{aligned}c_V = \langle \Omega|0\rangle &= \left[ \det \begin{pmatrix} B^{++\dagger} B^{++} & 0 \\ 0 & (B^{--\dagger} B^{--})^* \end{pmatrix} \right]^{\frac{1}{4}} = \sqrt{|\det B^{++}|} \sqrt{|\det B^{--}|} \\ &= |\det B^{++}| = |\det B^{--}|.\end{aligned}\tag{C.45}$$

The last two equality signs follow because the unitarity of  $B^{\pm\pm}$  implies  $|\det B^{++}| = |\det B^{--}|$  (and also  $|\det B^{+-}| = |\det B^{-+}|$ ).

$\overline{ab}/c_V$	$c_S$	$d_S$	$c_S^\dagger$	$d_S^\dagger$	$C$	$D$	$C^\dagger$	$D^\dagger$
$c_S$	0	0	1	0	0	$B_{-+}^\dagger$	$B_{++}^\dagger$	
$d_S$	0	0	0	1	$B_{+-}^T$	0	0	$B_{--}^T$
$c_S^\dagger$	0	0	0	$B_{-+}^T B_{--}^{T-1}$	$B_{-+}^T B_{--}^T B_{+-}^T$	0	0	$B_{-+}^T$
$d_S^\dagger$	0	0	$B_{+-}^\dagger B_{++}^{\dagger-1}$	0	0	$B_{+-}^\dagger B_{++}^\dagger B_{-+}^\dagger$	$B_{+-}^\dagger$	0
$C$	0	0	$B_{++}^{\dagger-1}$	0	0	$B_{++}^{\dagger-1} B_{-+}^\dagger$	1	0
$D$	0	0	0	$B_{--}^{T-1}$	$B_{--}^{T-1} B_{+-}^T$	0	0	1
$C^\dagger$	0	0	0	0	0	0	0	0
$D^\dagger$	0	0	0	0	0	0	0	0

**Table C.2:** All generalized contractions between the operators  $c_S$ ,  $d_S$ ,  $c_S^\dagger$ ,  $d_S^\dagger$ ,  $C$ ,  $D$ ,  $C^\dagger$  and  $D^\dagger$  scaled by the vacuum persistence amplitude  $c_V = \langle \Omega | 0 \rangle$ . We put the “signs” of the matrices into the subscript instead of the superscript to save some space, e.g.  $B^{++\dagger-1} \equiv B_{++}^{\dagger-1}$ .

For a more complex example, consider the amplitude of the vacuum decaying into a particle and anti-particle. The initial state is simply  $|i\rangle = |0\rangle$ . As we explained above, the only sensible final state is  $D_{i,S}^\dagger C_{j,S}^\dagger |\Omega_S\rangle$ . The matrix element is then

$$\begin{aligned} \langle f | U(t) | i \rangle &= \langle \Omega_S(t) | C_{j,S}(t) D_{i,S}(t) U(t) | 0 \rangle = \langle \Omega_S | U U^\dagger C_{j,S} U U^\dagger D_{i,S} U | 0 \rangle \\ &= \langle \Omega | C_j D_i | 0 \rangle. \end{aligned} \quad (\text{C.46})$$

It can be evaluated with the generalized Wick theorem from the preceding section, in particular we need table C.1 with  $\mu$  and  $\nu$  taken from Eq. (C.44)

$$\langle f | U | i \rangle = \overline{C_j D_i} = c_V \left( B^{++\dagger-1} B^{-\dagger} \right)_{ji}. \quad (\text{C.47})$$

For another example, let us look at the particle to particle amplitude. With  $|i\rangle = c_{i,S}^\dagger |0\rangle$ ,  $|f\rangle = C_{j,S}^\dagger |\Omega_S\rangle$  we find

$$\langle f | U | i \rangle = \langle \Omega | C_j c_{i,S}^\dagger | 0 \rangle = \overline{C_j c_{i,S}^\dagger} = c_V (B^{++\dagger-1})_{ji}. \quad (\text{C.48})$$

An expanded version of table C.1 showing all contractions between the operators can be found in table C.2.

Every in-state is of the form  $I(c_S^\dagger, d_S^\dagger) |0\rangle$  and every out-state of the form  $F(C_S^\dagger, D_S^\dagger) |\Omega_S\rangle$  for some functions  $I$  and  $F$ . Thus every amplitude can be written as

$$\begin{aligned} \langle \Omega_S(t) | F(C_S^\dagger(t), D_S^\dagger(t))^\dagger U(t) I(c_S^\dagger, d_S^\dagger) | 0 \rangle \\ = \langle \Omega(t) | F(C^\dagger(t), D^\dagger(t))^\dagger I(c_S^\dagger, d_S^\dagger) | 0 \rangle. \end{aligned} \quad (\text{C.49})$$

So of all the contractions in table C.2 we are only going to need those between  $c_S^\dagger$ ,  $d_S^\dagger$ ,  $C$ ,  $D$  to compute physical amplitudes. This also explains why the Bogoliubov transform is defined as the diagonal arrow in the diagram C.1 instead of, for example, as the left downward arrow, which would make the diagram more symmetrical. But any sensible

quantity we would want to compute, be it expectation value or amplitude, can be expressed in terms of  $\mathbf{c}_S$ ,  $\mathbf{d}_S$ ,  $\mathbf{C}$ ,  $\mathbf{D}$ , their adjoints,  $|0\rangle$  and  $|\Omega\rangle$ . Therefore, the transformation  $B$  is what is needed most often and should be made simple.

We reached the goal of this chapter. We clarified which expectation values and amplitudes bear physical relevance. Their computation can always be reduced to the matrices  $B^{\pm\pm}$ . These can in turn be computed from Eq. (C.31) as the scalar products between the solutions to the first-quantized Schrödinger equation and the eigenstates to  $h(t)$ . That means solving the first-quantized problem provides us with all the information needed to calculate all second-quantized observables.



# List of Figures

1.1	Schematic illustration of the Schwinger (left) and Breit-Wheeler effect (right) in the Dirac sea picture. The positron continuum is the lower blue band, the electron continuum the upper one. The red circle represents a particle, the white circle a hole and the wiggly line a photon. . . . .	3
1.2	Schematic illustration of the dynamically assisted Schwinger effect, with entities as in Fig. 1.1. . . . .	4
2.1	Plots of the time evolution of the vector potential (left) and electric field (right) for the Sauter pulse (2.40). . . . .	16
2.2	Time evolution of the pair density $f$ for Schwinger (black) and Sauter pulse (blue: $\tau = 2/m$ ; red: $\tau = 5/m$ ; green: $\tau = 10/m$ ) at $\mathbf{p} = 0$ . The field strength is $E_0 = 0.3E_c$ in the left and $E_0 = 0.4E_c$ in the right panel. The fields for the Schwinger field are given by (2.37) and its solution by (2.38). For the Sauter pulse, the corresponding equations are (2.40) and (2.41). . .	16
2.3	Plot of the time evolution of the vector potential (left) and electric field (right) for the periodic pulse (2.43). The envelope $K$ is shown as a dashed black curve in the left panel. Its parameters are $t_{\text{ramp}} = 1.5T$ and $t_{\text{flat}} = 5T$ . 19	
2.4	Contour plot of the pair density $f$ over the phase space $p_{\perp}$ - $p_{\parallel}$ with parameters $E_0 = 0.2E_c$ , $\nu = 0.02m$ , $t_{\text{ramp}} = 5T$ , $t_{\text{flat}} = 50T$ . Loci of momenta, where $2\Omega_0(\mathbf{p}) = n\nu$ , form sharp ridges where $f$ becomes large. . . . .	24
2.5	Cut through the phase space contour plot in Fig. 2.4 for $p_{\parallel} = 0$ (left) and $p_{\perp} = 0$ (right). The shell number $n$ is displayed above the ridge peaks. . . .	24
2.6	Left panel: Plot of the Fourier zero mode $\Omega_0$ as a function of $p_{\perp}$ , $p_{\parallel} = 0$ (red) or a function of $p_{\parallel}$ , $p_{\perp} = 0$ (blue) with parameters $E_0 = 0.2E_c$ , $\nu = 0.02m$ . Example solutions for $2\Omega_0 = 651\nu$ and $2\Omega_0 = 653\nu$ are indicated by the dashed lines. Right panel: Plot of the effective mass $m_*$ given by Eq. (2.60) as a function of the Keldysh parameter $\gamma$ . . . . .	25
2.7	Plot of the time evolution of $f$ for certain values of $p_{\perp}$ and $p_{\parallel}$ referring to a point on a ridge. Parameters are $E_0 = 0.2E_c$ , $\nu = 0.5m$ , $t_{\text{ramp}} = 5T$ , $t_{\text{flat}} = 10T$ . We choose our momenta so that we are on a shell for the given parameters, i.e. $p_{\perp} = 0.6920m$ and $p_{\parallel} = 0$ . The switching-off sets in at $t = 15T$ and makes the oscillations go to zero. The residual density remains constant for $t > 20T$ . . . . .	27
2.8	A zoom into the region of the $n = 651$ peak in the left panel of Fig. 2.5. Red: $t_{\text{flat}} = 20T$ ; green: $t_{\text{flat}} = 40T$ ; blue: $t_{\text{flat}} = 60T$ . . . . .	28
2.9	Plot of the $t_{\text{flat}}$ dependence of $f(t_{\text{off}})$ . Parameters are $E_0 = 0.2E_c$ , $\nu = 0.02m$ , $t_{\text{ramp}} = 5T$ . We choose our momenta so that we are on the $n = 651$ shell in the left panel of Fig. 2.5, i.e. $p_{\perp} = 0.2985933m$ and $p_{\parallel} = 0$ . Left: $1 < t_{\text{flat}}/T < 10^3$ , log-log scales; right: $0 < t_{\text{flat}}/T < 16000$ , linear scales. . .	29

2.10	A zoom into the $n = 651$ peak region in the left panel of Fig. 2.5 (black curve). In red is a fit of $a \sin^2[b(p - p_n)]/[b(p - p_n)]^2$ to this data, $a = 8.312 \times 10^{-4}$ , $b = 1.135 \times 10^3/m$ and $p_n = 0.2986m$ . . . . .	30
2.11	Schematic plot of the upper complex $t$ -plane, showing two of the zeros of $\Omega^2$ (dots labeled by $t_0$ and $-t_0^*$ ), the branch cuts emerging from them (dashed lines) and the integration contour chosen (red line, direction marked by arrows, partial contour paths labeled with $\Gamma_i$ ). . . . .	32
2.12	Schematic plot of the integration contours in the $x$ and $y$ -planes defined by the substitutions in the text. . . . .	34
2.13	A zoom into the $n = 651$ peak region in the left panel of Fig. 2.5 (black curve). See also Fig. 2.10. In red is a the analytically derived shell shape $a \sin^2[b(p - p_n)]/[b(p - p_n)]^2$ with $a = 8.121 \times 10^{-4}$ , $b = 1.097 \times 10^3/m$ and $p_n = 0.3014m$ . . . . .	36
2.14	Comparison of the pair density $f$ as a function of $p_\perp$ at $p_\parallel = 0$ with the envelope $\mathcal{E}(p_\perp)$ from Eq. (2.83) (dashed curve). Parameters are $E_0 = 0.2E_c$ , $\nu = 0.02m$ (top left); $E_0 = 0.2E_c$ , $\nu = 0.05m$ (top right); $E_0 = 0.3E_c$ , $\nu = 0.02m$ (bottom left); $E_0 = 0.3E_c$ , $\nu = 0.05m$ (bottom right). For all panels $t_{\text{ramp}} = 5T$ , $t_{\text{flat}} = 50T$ . The top left panel uses the same parameters as the left panel of Fig. 2.5. . . . .	37
2.15	Contour plot of $4\frac{m}{\nu}g(\gamma)$ , the negative of the exponent of $\mathcal{E}(0)$ , over the parameter space. The solid black curves are contour lines at integer powers of 10, the gray short dashed curves at $10^{0.2}$ , ..., $10^{0.8}$ between them. The long dashed lines are the loci of constant Keldysh parameter $\gamma$ . The color map is inverted compared to Fig. 2.4, because <i>small</i> exponents lead to <i>large</i> $f$ . Therefore the same colors correspond to each other in this figure and Fig. 2.4. Red means large, blue small $f$ . . . . .	39
2.16	Cuts through the parameter space shown in Fig. 2.15 for $\nu = 10^{-2}m$ (left) and $E_0 = 10^{-3}E_c$ (right). The dashed line denotes $\gamma = 1$ , left of which $\gamma \ll 1$ (adiabatic regime) and right of which $\gamma \gg 1$ (multiphoton regime). Note that the $E_0$ -axis is reversed in the left panel to have the regimes be on the same side of the $\gamma = 1$ line in both panels. . . . .	40
3.1	Plot of the time evolution of the vector potential (left) and electric field (right) for the superposition of two Sauter pulses (3.1) for $E_1 = 0.3E_c$ , $\tau_1 = 10/m$ , $E_2 = 0.02E_c$ , $\tau_2 = 2/m$ . The dashed lines are for the field 1 alone. . . . .	42
3.2	Plot of the Fourier transform $\tilde{E}(\omega)$ of the electric field for the superposition of two Sauter pulses (3.1) for $E_1 = 0.3E_c$ , $\tau_1 = 10/m$ , $E_2 = 0.02E_c$ , $\tau_2 = 2/m$ . The dashed line is for the field 1 alone. . . . .	43
3.3	Plot of the residual pair density $f$ for the Sauter pulse with two fields as a function of $p_\perp$ at $p_\parallel = 0$ for $E_1 = 0.3E_c$ , $\tau_1 = 10/m$ , $\tau_2 = 2/m$ and $E_2 = 0.02E_c$ (blue), $E_2 = 0.04E_c$ (red), $E_2 = 0.06E_c$ (green). The dashed lines are for the first field switched off, $E_1 = 0$ , and the black curve for the second switched off, $E_2 = 0$ . . . . .	44
3.4	Plot of the residual phase space density $f$ as a function of $p_\perp$ at $p_\parallel = 0$ for $E_1 = 0.2E_c$ , $E_2 = 0.05E_c$ , $\nu = 0.02m$ , $N = 25$ (top) and $N = 17$ (bottom). In the left panels, only the strong, slow field 1 is turned on; in the right panels, only the weak, fast field 2; in the middle panels, both fields are superimposed. . . . .	46



- 3.5 Plot of the residual phase space density  $f$  as a function of  $p_{\perp}$  at  $p_{\parallel} = 0$  for  $E_1 = 0.2E_c$ ,  $\nu = 0.02m$ ,  $N = 25$  and  $E_2 = 0$  (top left),  $E_2 = 0.02E_c$  (top middle),  $E_2 = 0.04E_c$  (top right),  $E_2 = 0.06E_c$  (bottom left),  $E_2 = 0.08E_c$  (bottom middle),  $E_2 = 0.1E_c$  (bottom right). . . . . 47
- 3.6 Schematic plot of the movement of the zeros of  $\Omega^2$  when increasing  $E_2$  in Eq. (3.3). Upper left:  $N = 4n + 0$ ; upper right:  $N = 4n + 1$ ; lower left:  $N = 4n + 2$ ; lower right:  $N = 4n + 3$  for some  $n \in \mathbb{N}$ . The blue point is the only zero when  $E_2 = 0$ . The arrow indicates the way that main zero moves when  $E_2$  increases. . . . . 49
- 3.7 Left panel: Plot of the integrand in Eq. (3.6) as a function of the imaginary part of the dimensionless time  $x = \text{Im } \nu_1 t$  at  $p_{\perp} = 0$  for the parameters  $E_1 = 0.1E_c$ ,  $\nu_1 = 0.02m$ ,  $N = 25$  and  $E_2 = 0$  (blue),  $E_2 = 0.01E_c$  (green),  $E_2 = 0.02E_c$  (cyan),  $E_2 = 0.05E_c$  (red). The curves end at  $x_0 = F^{-1}(1)$ . Right panel: Plot of  $x_0$  as a function of  $E_2$  for  $p_{\perp} = 0$ ,  $E_1 = 0.1E_c$ ,  $\nu_1 = 0.02m$  and  $N = 17$  (blue),  $N = 21$  (green),  $N = 25$  (cyan),  $N = 29$  (red). 51
- 4.1 Contour plot of the residual photon phase-space distribution  $f_{\gamma}$  over the  $k_{\parallel}$ - $k_{\perp}$  plane for the Sauter pulse with  $E_0 = 0.2E_c$  and  $\tau = 2/m$ . The solid black curves are contour lines at integer powers of 10. . . . . 63
- 4.2 Plot of the residual photon phase-space distribution  $f_{\gamma}$  as a function of  $k_{\perp}$  at  $k_{\parallel} = 0$  for the Sauter pulse with  $E_0 = 0.2E_c$  and  $\tau = 2/m$ . The blue curve is the full result. The green curve depicts the contribution from the intermediate integral, the cyan curve from the asymptotic terms and the red curve from the mixed terms. . . . . 64
- 4.3 Contour plot of  $f_{\gamma}(k_{\perp} = 10^{-4}m, k_{\parallel} = 0)/f(\mathbf{p} = 0)$ , i.e. the ratio of the photon and pair spectrum at two points in phase space for the Sauter pulse, over the parameter space. The solid black curves are contour lines at integer powers of 10, the gray short dashed curves at  $10^{0.2}$ , ...,  $10^{0.8}$  between them. The long dashed lines are the loci of constant Keldysh parameter  $\gamma$ . . . . . 65
- 4.4 Plot of the photon spectrum over  $k_{\perp}$  at  $k_{\parallel} = 0$  for the superposition of two Sauter pulses (dashed curves) and two periodic pulses (solid curves). Parameters:  $E_1 = 0.1E_c$ ,  $\nu_1 = 0.5m$ ,  $\nu_2 = 2m$  and  $E_2 = 0$  (blue),  $E_2 = 0.05E_c$  (red). Additionally for the periodic pulse  $t_{\text{flat}} = 50T$  and  $t_{\text{ramp}} = 5T$ . 66
- A.1 Plot of the modulus of  $\alpha(t)$  (red) and  $\beta(t)$  (blue) given by (A.6) as a function of time. Parameters are  $\omega = 0.8E$  and  $\tau = 2/E$  (solid) as well as  $\tau = \pi/\omega = 5\pi/4E$  (dashed). . . . . 72
- C.1 The different annihilation operators from the text and the unitary transformations between them. In the left column, the operators are in the Schrödinger picture, in the right in the Heisenberg picture. The operators in the lower row are the Bogoliubov transformed versions of those in the upper row. . . . . 88

## List of Tables

C.1	All generalized contractions between the operators $e, e^\dagger, f$ and $f^\dagger$ scaled by the vacuum persistence amplitude $c_V = \langle 0_f   0_e \rangle$ . . . . .	85
C.2	All generalized contractions between the operators $c_S, d_S, c_S^\dagger, d_S^\dagger, C, D, C^\dagger$ and $D^\dagger$ scaled by the vacuum persistence amplitude $c_V = \langle \Omega   0 \rangle$ . We put the “signs” of the matrices into the subscript instead of the superscript to save some space, e.g. $B^{++\dagger-1} \equiv B_{++}^{\dagger-1}$ . . . . .	90

## Bibliography

- [1] J. Schwinger, “On Quantum-Electrodynamics and the Magnetic Moment of the Electron”, *Phys. Rev.* **73**, 416 (1948).
- [2] T. Aoyama, M. Hayakawa, T. Kinoshita, and M. Nio, “Tenth-Order QED Contribution to the Electron  $g-2$  and an Improved Value of the Fine Structure Constant”, *Phys. Rev. Lett.* **109**, 111807 (2012).
- [3] T. Aoyama, M. Hayakawa, T. Kinoshita, and M. Nio, “Tenth-order electron anomalous magnetic moment: Contribution of diagrams without closed lepton loops”, *Phys. Rev. D* **91**, 033006 (2015).
- [4] J. Schwinger, “On Gauge Invariance and Vacuum Polarization”, *Phys. Rev.* **82**, 664 (1951).
- [5] F. Sauter, “Über das Verhalten eines Elektrons im homogenen elektrischen Feld nach der relativistischen Theorie Diracs”, *Z. Phys.* **69**, 742 (1931).
- [6] W. Heisenberg and H. Euler, “Folgerungen aus der Diracschen Theorie des Positrons”, *Z. Phys.* **98**, 714 (1936).
- [7] B. King, A. Di Piazza, and C. H. Keitel, “A matterless double slit”, *Nature Photonics* **4**, 92 (2010).
- [8] B. King, A. Di Piazza, and C. H. Keitel, “Double-slit vacuum polarization effects in ultraintense laser fields”, *Phys. Rev. A* **82**, 032114 (2010).
- [9] J. J. Klein and B. P. Nigam, “Birefringence of the Vacuum”, *Phys. Rev.* **135**, B1279 (1964).
- [10] T. Heinzl, B. Liesfeld, K.-U. Amthor, H. Schwöerer, R. Sauerbrey, and A. Wipf, “On the Observation of Vacuum Birefringence”, *Opt. Commun.* **267**, 318 (2006).
- [11] J. Rafelski, L. P. Fulcher, and W. Greiner, “Superheavy elements and an upper limit to the electric field strength”, *Phys. Rev. Lett.* **27**, 958 (1971).
- [12] J. Reinhardt and W. Greiner, “Quantum electrodynamics of strong fields”, *Rep. Prog. Phys.* **40**, 219 (1977).
- [13] B. Müller, “Positron Creation in Superheavy Quasi-Molecules”, *Annual Review of Nuclear Science* **26**, 351 (1976).
- [14] J. Rafelski, B. Müller, and W. Greiner, “Spontaneous vacuum decay of supercritical nuclear composites”, *Z. Phys. A Hadron. Nucl.* **285**, 49 (1978).
- [15] C. Kouveliotou et al., “An X-ray pulsar with a superstrong magnetic field in the soft  $\gamma$ -ray repeater SGR1806–20”, *Nature* **393**, 235 (1998).
- [16] S. Mereghetti, “The strongest cosmic magnets: soft gamma-ray repeaters and anomalous X-ray pulsars”, *Astron. Astrophys. Rev.* **15**, 225 (2008).

- [17] V. I. Denisov, V. A. Sokolov, and M. I. Vasili'ev, "Nonlinear vacuum electrodynamics birefringence effect in a pulsar's strong magnetic field", *Phys. Rev. D* **90**, 023011 (2014).
- [18] R. P. Mignani et al., "Evidence for vacuum birefringence from the first optical-polarimetry measurement of the isolated neutron star RX J1856.5–3754", *Mon. Not. R. Astron. Soc.* **465**, 492 (2017).
- [19] C. Hernandez-Gomez et al., "The Vulcan 10 PW project", *J. Phys.: Conf. Ser.* **244**, 032006 (2010).
- [20] J. P. Zou et al., "Design and current progress of the Apollon 10 PW project", *HPLaser* **3** (2015) 10.1017/hpl.2014.41.
- [21] V. Bagnoud et al., "Commissioning and early experiments of the PHELIX facility", *Appl. Phys. B* **100**, 137 (2010).
- [22] *The Petawatt High-Energy Laser for Heavy Ion EXperiments (PHELIX)*, [www.gsi.de/en/work/research/appamml/plasma\\_physicsphelix/phelix](http://www.gsi.de/en/work/research/appamml/plasma_physicsphelix/phelix), Archived at [archive.is/EdJ90](http://archive.is/EdJ90).
- [23] M. Dunne, "A high-power laser fusion facility for Europe", *Nat. Phys.* **2**, 2 (2006).
- [24] *High Power laser for Energy Research project (HiPER)*, [www.hiper-laser.org](http://www.hiper-laser.org), Archived at [archive.is/qNCOC](http://archive.is/qNCOC).
- [25] M. Hornung et al., "Temporal pulse control of a multi-10 TW diode-pumped Yb:Glass laser", *Appl. Phys. B* **101**, 93 (2010).
- [26] *Petawatt Optical Laser Amplifier for Radiation Intensive ExperimentS (POLARIS)*, [www.ioq.uni-jena.de/Lasersysteme/POLARIS](http://www.ioq.uni-jena.de/Lasersysteme/POLARIS), Archived at [archive.is/Ytwfa](http://archive.is/Ytwfa).
- [27] *Helmholtz International Beamline for Extreme Fields at the European XFEL (HI-BEF)*, [www.hzdr.de/hgfbeamline](http://www.hzdr.de/hgfbeamline), Archived at [archive.is/7Rt1p](http://archive.is/7Rt1p).
- [28] N. Blanchot et al., "Overview of PETAL, the multi-Petawatt project on the LIL facility", *Plasma Phys. Contr. F.* **50**, 124045 (2008).
- [29] G. Korn, B. LeGarrec, and B. Rus, "ELI Extreme Light Infrastructure science and technology with ultra-intense lasers", *Cleo: 2013* (2013), p. 1.
- [30] *European Extreme Light Infrastructure (ELI)*, [www.eli-laser.eu](http://www.eli-laser.eu), Archived at [archive.is/EbYGU](http://archive.is/EbYGU).
- [31] *ELI Nuclear Physics (ELI-NP)*, [www.eli-np.ro](http://www.eli-np.ro), Archived at [archive.is/0Hj4b](http://archive.is/0Hj4b).
- [32] A. V. Bashinov, A. A. Gonoskov, A. V. Kim, G. Mourou, and A. M. Sergeev, "New horizons for extreme light physics with mega-science project XCELS", *The European Physical Journal Special Topics* **223**, 1105 (2014).
- [33] *Exawatt Center for Extreme Light Studies (XCELS)*, [www.xcels.iapras.ru](http://www.xcels.iapras.ru), Archived at [archive.is/95haq](http://archive.is/95haq).
- [34] L. Xu et al., "Trends in ultrashort and ultrahigh power laser pulses based on optical parametric chirped pulse amplification", *Chin. Phys. B* **24**, 018704 (2015).
- [35] G. Gregori et al., "A proposal for testing subcritical vacuum pair production with high power lasers", *High Energ. Dens. Phys.* **6**, 166 (2010).
- [36] B. King and A. Di Piazza, "Investigating the QED vacuum with ultra-intense laser fields", *Eur. Phys. J.-Spec. Top.* **223**, 1063 (2014).

- [37] T. Heinzl, “Strong-Field QED and High-Power Lasers”, *Int. J. Mod. Phys. A* **27**, 1260010 (2012).
- [38] H. Gies, “Strong laser fields as a probe for fundamental physics”, *Eur. Phys. J. D* **55**, 311 (2008).
- [39] G. V. Dunne, “New strong-field QED effects at extreme light infrastructure”, *Eur. Phys. J. D* **55**, 327 (2009).
- [40] G. V. Dunne, “Extreme quantum field theory and particle physics with IZEST”, *Eur. Phys. J. Spec. Top.* **223**, 1055 (2014).
- [41] S. W. Hawking, “Black hole explosions?”, *Nature* **248**, 30 (1974).
- [42] G. W. Gibbons and S. W. Hawking, “Cosmological event horizons, thermodynamics, and particle creation”, *Phys. Rev. D* **15**, 2738 (1977).
- [43] L. Parker, “Particle creation in expanding universes”, *Phys. Rev. Lett.* **21**, 562 (1968).
- [44] L. Parker, “Quantized fields and particle creation in expanding universes. i”, *Phys. Rev.* **183**, 1057 (1969).
- [45] L. Parker, “Quantized fields and particle creation in expanding universes. ii”, *Phys. Rev. D* **3**, 346 (1971).
- [46] M. Basler and B. Kämpfer, “Particle Production During Inflationary Reheating”, *Int. J. Mod. Phys. A* **7**, 2033 (1992).
- [47] W. G. Unruh, “Notes on black-hole evaporation”, *Phys. Rev. D* **14**, 870 (1976).
- [48] R. Schützhold and C. Maia, “Quantum radiation by electrons in lasers and the Unruh effect”, *Eur. Phys. J. D* **55**, 375 (2009).
- [49] A. Casher, H. Neuberger, and S. Nussinov, “Chromoelectric-flux-tube model of particle production”, *Phys. Rev. D* **20**, 179 (1979).
- [50] F. Michler, H. van Hees, D. D. Dietrich, S. Leupold, and C. Greiner, “Off-equilibrium photon production during the chiral phase transition”, *Ann. Phys.* **336**, 331 (2013).
- [51] F. Michler, H. van Hees, D. D. Dietrich, and C. Greiner, “Asymptotic description of finite lifetime effects on the photon emission from a quark-gluon plasma”, *Phys. Rev. D* **89**, 116018 (2014).
- [52] D. L. Burke et al., “Positron Production in Multiphoton Light-by-Light Scattering”, *Phys. Rev. Lett.* **79**, 1626 (1997).
- [53] R. Schützhold, H. Gies, and G. Dunne, “Dynamically Assisted Schwinger Mechanism”, *Phys. Rev. Lett.* **101**, 130404 (2008).
- [54] G. V. Dunne, H. Gies, and R. Schützhold, “Catalysis of Schwinger vacuum pair production”, *Phys. Rev. D* **80**, 111301 (2009).
- [55] *The Technical Design Report (TDR) of the European XFEL*, [xfel.desy.de/technical\\_information/tdr/tdr](http://xfel.desy.de/technical_information/tdr/tdr), Archived at [archive.is/MxgMs](http://archive.is/MxgMs).
- [56] F. Gelis and N. Tanji, “Schwinger mechanism revisited”, *Prog. Part. Nucl. Phys.* **87**, 1 (2016).
- [57] S. M. Schmidt, D. B. Blaschke, G. Röpke, S. A. Smolyansky, A. V. Prozorkevich, and V. D. Toneev, “A Quantum kinetic equation for particle production in the Schwinger mechanism”, *Int. J. Mod. Phys. E* **7**, 709 (1998).

- [58] S. Schmidt, D. B. Blaschke, G. Röpke, A. V. Prozorkevich, S. A. Smolyansky, and V. D. Toneev, “Non-Markovian effects in strong-field pair creation”, *Phys. Rev. D* **59**, 094005 (1999).
- [59] M. F. Linder, C. Schneider, J. Sicking, N. Szpak, and R. Schützhold, “Pulse shape dependence in the dynamically assisted Sauter-Schwinger effect”, *Phys. Rev. D* **92**, 085009 (2015).
- [60] C. Fey and R. Schützhold, “Momentum dependence in the dynamically assisted Sauter-Schwinger effect”, *Phys. Rev. D* **85**, 025004 (2012).
- [61] C. K. Dumlu and G. V. Dunne, “Stokes phenomenon and schwinger vacuum pair production in time-dependent laser pulses”, *Phys. Rev. Lett.* **104**, 250402 (2010).
- [62] C. K. Dumlu and G. V. Dunne, “Complex Worldline Instantons and Quantum Interference in Vacuum Pair Production”, *Phys. Rev. D* **84**, 125023 (2011).
- [63] C. K. Dumlu and G. V. Dunne, “Interference effects in Schwinger vacuum pair production for time-dependent laser pulses”, *Phys. Rev. D* **83**, 065028 (2011).
- [64] F. Hebenstreit, A. Ilderton, M. Marklund, and J. Zamanian, “Strong field effects in laser pulses: The Wigner formalism”, *Phys. Rev. D* **83**, 065007 (2011).
- [65] F. Hebenstreit, R. Alkofer, and H. Gies, “Schwinger pair production in space- and time-dependent electric fields: Relating the Wigner formalism to quantum kinetic theory”, *Phys. Rev. D* **82**, 105026 (2010).
- [66] F. Hebenstreit, R. Alkofer, and H. Gies, “Particle Self-Bunching in the Schwinger Effect in Spacetime-Dependent Electric Fields”, *Phys. Rev. Lett.* **107**, 180403 (2011).
- [67] G. V. Dunne and C. Schubert, “Worldline instantons and pair production in inhomogenous fields”, *Phys. Rev. D* **72**, 105004 (2005).
- [68] H. Gies and K. Klingmüller, “Pair production in inhomogeneous fields”, *Phys. Rev. D* **72**, 065001 (2005).
- [69] M. Ruf, G. R. Mocken, C. Müller, K. Z. Hatsagortsyan, and C. H. Keitel, “Pair Production in Laser Fields Oscillating in Space and Time”, *Phys. Rev. Lett.* **102**, 080402 (2009).
- [70] H. Gies and G. Torgrimsson, “Critical Schwinger Pair Production”, *Phys. Rev. Lett.* **116**, 090406 (2016).
- [71] H. Gies and G. Torgrimsson, “Critical Schwinger pair production. II. Universality in the deeply critical regime”, *Phys. Rev. D* **95**, 016001 (2017).
- [72] A. Blinne and H. Gies, “Pair production in rotating electric fields”, *Phys. Rev. D* **89**, 085001 (2014).
- [73] S. Villalba-Chávez and C. Müller, “Photo-production of scalar particles in the field of a circularly polarized laser beam”, *Phys. Lett. B* **718**, 992 (2013).
- [74] A. D. Piazza, A. I. Milstein, and C. Müller, “Polarization of the electron and positron produced in combined Coulomb and strong laser fields”, *Phys. Rev. A* **82**, 062110 (2010).
- [75] Y. B. Wu and S. S. Xue, “Nonlinear Breit-Wheeler process in the collision of a photon with two plane waves”, *Phys. Rev. D* **90**, 013009 (2014).
- [76] A. Otto, D. Seipt, D. Blaschke, B. Kämpfer, and S. A. Smolyansky, “Lifting shell structures in the dynamically assisted Schwinger effect in periodic fields”, *Phys. Lett. B* **740**, 335 (2015).

- [77] A. Otto, D. Seipt, D. B. Blaschke, S. A. Smolyansky, and B. Kämpfer, “Dynamical Schwinger process in a bifrequent electric field of finite duration: Survey on amplification”, *Phys. Rev. D* **91**, 105018 (2015).
- [78] A. Otto et al., “Pair production by Schwinger and Breit-Wheeler processes in bi-frequent fields”, *J. Plasma Phys.* **82**, 655820301 (2016).
- [79] T. Nousch et al., “Laser assisted Breit-Wheeler and Schwinger processes”, Proceedings of the International Symposium on New Horizons in Fundamental Physics, Makutsi, South Africa, 23.–28. November 2015, FIAS Interdisc. Sci. Ser. (2017), pp. 253–262.
- [80] A. D. Panferov, S. A. Smolyansky, A. Otto, B. Kämpfer, D. B. Blaschke, and Ł. Juchnowski, “Assisted dynamical Schwinger effect: pair production in a pulsed bifrequent field”, *Eur. Phys. J. D* **70**, 56 (2016).
- [81] S. A. Smolyansky, A. D. Panferov, D. B. Blaschke, Ł. Juchnowski, B. Kämpfer, and A. Otto, “Vacuum particle-antiparticle creation in strong fields as a field induced phase transition”, *Russ. Phys. J.* **59**, 1731 (2017).
- [82] A. Otto and B. Kämpfer, “Afterglow of the dynamical Schwinger process: Soft photons amass”, *Phys. Rev. D* **95**, 125007 (2017).
- [83] H. Oppitz, “Dynamisch assistierter Schwinger-Effekt in unterschiedlichen Feldkonfigurationen”, Bachelor’s Thesis (Technische Universität Dresden, 2013).
- [84] S. Hähnel, “Paarerzeugung in elektrischen Feldern: Numerische Untersuchungen zum Schwinger-Effekt”, Bachelor’s thesis (Technische Universität Dresden, 2015).
- [85] H. Oppitz, “Dynamisch assistierter Schwinger-Effekt für Multi-Skalen-Feldkonfigurationen”, Master’s Thesis (Technische Universität Dresden, 2017).
- [86] F. Hebenstreit, “Schwinger effect in inhomogeneous electric fields”, PhD thesis (Karl-Franzens-Universität Graz, 2011).
- [87] A. Nuriman, B. S. Xie, Z. L. Li, and D. Sayipjamal, “Enhanced electron-positron pair creation by dynamically assisted combinational fields”, *Phys. Lett. B* **717**, 465 (2012).
- [88] F. Hebenstreit, R. Alkofer, G. Dunne, and H. Gies, “Momentum Signatures for Schwinger Pair Production in Short Laser Pulses with a Subcycle Structure”, *Phys. Rev. Lett.* **102**, 150404 (2009).
- [89] *Boost Units Library*, [www.boost.org/doc/libs/1\\_61\\_0/doc/html/boost\\_units.html](http://www.boost.org/doc/libs/1_61_0/doc/html/boost_units.html), Archived at [archive.is/I6yF1](http://archive.is/I6yF1).
- [90] J. C. Butcher, *Numerical methods for ordinary differential equations* (John Wiley & Sons, Chichester, 2008).
- [91] *Boost Odeint Library*, [www.boost.org/doc/libs/1\\_63\\_0/libs/numeric/odeint/doc/html/index.html](http://www.boost.org/doc/libs/1_63_0/libs/numeric/odeint/doc/html/index.html), Archived at [archive.is/eZQ9x](http://archive.is/eZQ9x).
- [92] G. Teschl, *Ordinary Differential Equations and Dynamical Systems*, Graduate Studies in Mathematics (American Mathematical Society, 2012).
- [93] D. B. Blaschke, B. Kämpfer, A. D. Panferov, A. V. Prozorkevich, and S. A. Smolyansky, “Influence of Laser Pulse Parameters on the Properties of  $e^-e^+$  Plasmas Created from Vacuum”, *Contrib. Plasm. Phys.* **53**, 165 (2013).



- [94] S. A. Smolyansky, D. B. Blaschke, V. V. Dmitriev, B. Kämpfer, A. V. Prozorkevich, and A. V. Tarakanov, “Photon cluster excitation mechanism in an  $e^-e^+$  plasma created from vacuum by a strong electromagnetic field”, *PoS (Baldin ISHEPP XXI)*, 069 (2012).
- [95] C. Kohlfürst, H. Gies, and R. Alkofer, “Effective Mass Signatures in Multiphoton Pair Production”, *Phys. Rev. Lett.* **112**, 050402 (2014).
- [96] G. R. Mocken, M. Ruf, C. Müller, and C. H. Keitel, “Nonperturbative multiphoton electron-positron-pair creation in laser fields”, *Phys. Rev. A* **81**, 022122 (2010).
- [97] I. Akal, S. Villalba-Chávez, and C. Müller, “Electron-positron pair production in a bifrequent oscillating electric field”, *Phys. Rev. D* **90**, 113004 (2014).
- [98] E. Brezin and C. Itzykson, “Pair Production in Vacuum by an Alternating Field”, *Phys. Rev. D* **2**, 1191 (1970).
- [99] A. Ringwald, “Pair production from vacuum at the focus of an X-ray free electron laser”, *Phys. Lett. B* **510**, 107 (2001).
- [100] D. B. Blaschke, B. Kämpfer, S. M. Schmidt, A. D. Panferov, A. V. Prozorkevich, and S. A. Smolyansky, “Properties of the electron-positron plasma created from a vacuum in a strong laser field: Quasiparticle excitations”, *Phys. Rev. D* **88**, 045017 (2013).
- [101] M. Orthaber, F. Hebenstreit, and R. Alkofer, “Momentum spectra for dynamically assisted Schwinger pair production”, *Phys. Lett. B* **698**, 80 (2011).
- [102] Z. L. Li, D. Lu, B. S. Xie, L. B. Fu, J. Liu, and B. F. Shen, “Enhanced pair production in strong fields by multiple-slit interference effect with dynamically assisted Schwinger mechanism”, *Phys. Rev. D* **89**, 093011 (2014).
- [103] C. Kohlfürst, M. Mitter, G. von Winckel, F. Hebenstreit, and R. Alkofer, “Optimizing the pulse shape for Schwinger pair production”, *Phys. Rev. D* **88**, 045028 (2013).
- [104] C. Schneider and R. Schützhold, “Dynamically assisted Sauter-Schwinger effect in inhomogeneous electric fields”, *J. High Energy Phys.* **2016**, 164 (2016).
- [105] J. C. R. Bloch et al., “Pair creation: Back reactions and damping”, *Phys. Rev. D* **60**, 116011 (1999).
- [106] Y. Kluger, J. M. Eisenberg, B. Svetitsky, F. Cooper, and E. Mottola, “Fermion pair production in a strong electric field”, *Phys. Rev. D* **45**, 4659 (1992).
- [107] Y. Kluger, J. M. Eisenberg, B. Svetitsky, F. Cooper, and E. Mottola, “Pair production in a strong electric field”, *Phys. Rev. Lett.* **67**, 2427 (1991).
- [108] Y. Kluger, J. M. Eisenberg, and B. Svetitsky, “Pair production in a strong electric field: an initial value problem in quantum field theory”, *Int. J. Mod. Phys. E* **2**, 333 (1993).
- [109] D. B. Blaschke, V. V. Dmitriev, G. Röpke, and S. A. Smolyansky, “BBGKY kinetic approach for an  $e^-e^+\gamma$  plasma created from the vacuum in a strong laser-generated electric field: The one-photon annihilation channel”, *Phys. Rev. D* **84**, 085028 (2011).
- [110] D. B. Blaschke, G. Röpke, S. M. Schmidt, S. A. Smolyansky, and A. V. Tarakanov, “Kinetics of Photon Radiation off an  $e^-e^+$ -Plasma Created from the Vacuum in a Strong Laser Field”, *Contrib. Plasma Phys.* **51**, 451 (2011).
- [111] D. B. Blaschke, S. M. Schmidt, S. A. Smolyansky, and A. V. Tarakanov, “Self-consistent description of  $e^-e^+\gamma$ -plasma created from the vacuum in a strong electric laser field”, *Phys. Part. Nuclei* **41**, 1004 (2010).



- [112] M. E. Peskin and D. V. Schroeder, *An Introduction to Quantum Field Theory* (Addison-Wesley, Reading, USA, 1995).
- [113] *Cuba – a library for multidimensional numerical integration*, [www.feynarts.de/cuba](http://www.feynarts.de/cuba), Archived at [archive.is/nk9e5](http://archive.is/nk9e5).
- [114] W. Witschel, “On the General Linear (Bogoliubov-)Transformation for Bosons”, *Z. Phys. B Con. Mat.* **21**, 313 (1975).
- [115] D. P. Jr, M. O. Pinho, and H. Rodrigues, “Recursive Construction of the Bosonic Bogoliubov Vacuum State”, *Quant. Phys. Lett.* **2**, 11 (2013).
- [116] E. S. Fradkin, D. M. Gitman, and S. Shvartsman, *Quantum Electrodynamics with Unstable Vacuum* (Springer-Verlag, Berlin, Heidelberg, 1991).



## Danksagung

Ich möchte mich bei Herrn Professor Dr. Burkhard Kämpfer ganz herzlich bedanken, mir die Gelegenheit gegeben zu haben, in einem so interessantem Gebiet der theoretischen Physik zu forschen, ferner für seine exzellente Betreuung und Motivation, die vielen zum Nachdenken und Hinterfragen anregenden Diskussionen und nicht zuletzt, dass er mir ermöglichte, auf nationalen und internationalen Konferenzen meine Arbeit vorzustellen.

Für die exzellenten Arbeitsbedingungen am Helmholtz-Zentrum Dresden-Rossendorf danke ich Herrn Professor Dr. Roland Sauerbrey und Herrn Professor Dr. Peter Joehnk, sowie den Direktoren des Instituts für Strahlenphysik, Herrn Professor Dr. Thomas Cowan und Herrn Professor Dr. Ulrich Schramm. Ich danke auch Herrn Professor Dr. Rüdiger Schmidt für die Gastfreundschaft am Institut für theoretische Physik der TU Dresden.

Mein Dank gilt auch meinen Kollegen, Mitarbeitern und Koautoren, Professor Dr. David Blaschke, Professor Dr. Stanislav A. Smolyansky, Professor Dr. Alexander I. Titov, Dr. Anatoli D. Panferov und Łukasz Juchnowski.

Ohne die vielen Mitglieder in meiner Arbeitsgruppe wären die letzten Jahre nur halb so erfolgreich und nicht halb so schön gewesen. Insbesondere möchte ich hier Herrn Dr. Daniel Seipt danken, dass er mich damals als Diplomanden unter seine Fittiche nahm und mir immer mit Rat und Tat zur Seite stand.

Grüße gehen raus an meine Freunde, den FSR Physik der TU Dresden und die ZaPF. Mit euch war das Studium um einiges erquicklicher.

Zu guter Letzt einen großen Dank an meine Eltern und meine Familie für ihre stete Unterstützung und dafür, nicht allzu oft „und was macht man später mal damit“ gefragt zu haben.



## Erklärung

Hiermit versichere ich, dass ich die vorliegende Arbeit ohne unzulässige Hilfe Dritter und ohne Benutzung anderer als der angegebenen Hilfsmittel angefertigt habe. Die aus fremden Quellen direkt oder indirekt übernommenen Gedanken sind als solche kenntlich gemacht. Die Arbeit wurde bisher weder im Inland noch im Ausland in gleicher oder ähnlicher Form einer anderen Prüfungsbehörde vorgelegt.

Diese Dissertation wurde am Helmholtz-Zentrum Dresden-Rossendorf unter der wissenschaftlichen Betreuung von Herrn Professor Dr. Burkhard Kämpfer angefertigt. Ich habe bisher an keiner Institution, weder im Inland noch im Ausland, einen Antrag auf Eröffnung eines Promotionsverfahrens gestellt. Ferner erkläre ich, dass ich die Promotionsordnung der Fakultät Mathematik und Naturwissenschaften der Technischen Universität Dresden vom 23. Februar 2011 anerkenne.

Andreas Otto  
Dresden, den 4. August 2017